eman ta zabal zazu

Universidad del País Vasco

Euskal Herriko Unibertsitatea

Designer Magneto-Optics with Plasmonic Magnetic Nanostructures

Nicolò Maccaferri

- PhD Thesis -

Thesis supervisor

Prof. Paolo Vavassori

2016

Resumen

La nanotecnología es un campo emergente y relativamente nuevo de la investigación, que ha ganado un gran interés en los últimos años. El término “nano” es un prefijo derivado de la palabra griega νάνος (nános) y significa "diminuto, enano". La nanotecnología y las nanociencias relativas a ésta destacan por su carácter multidistiplinario y representan el enfoque combinado de diferentes campos como la biología, la química, la física y la ciencia de materiales, para diseñar y manipular estructuras, materiales y sus propiedades a escala nanométrica (hablamos de dimensiones menores a 100 nm, donde1 nm = 10^{-9} m). El origen de la nanotecnología se le atribuye a Richard Feynman, que pronosticó la exploración y la manipulación del nanomundo en 1959 en su famoso discurso "There’s Plenty of Room at the Bottom" (Hay mucho sitio al fondo).[1] El término “nanotecnología” fue utilizado por primera vez en 1974 por Taniguchi[2], y popularizado por Drexler[3] en 1986 con su libro "Engines of Creation: The Coming Era of Nanotechnology" (La próxima era de la nanotecnología). Hoy en día la nanotecnología ya se ha convertido en parte de nuestra vida cotidiana. Por primera vez en la historia somos capaces de dominar, registrar y entender el mundo microscópico a la escala más pequeña posible.

Los campos electromagnéticos, y en concreto la luz, forman parte privilegiada de esta joven disciplina al ser portadores de información e instrumentos de medida y control. La nanofotónica se encarga del estudio de la luz a escala nanométrica y aporta beneficios a la biología, la química y la ingeniería a través de nuevas configuraciones para microscopía, de modificación externa de reacciones y de dispositivos integrados para conmutación óptica. Algunos de los avances más significativos de la nanofotónica se han centrado en los metamateriales[4, 5], cuyas propiedades ópticas superan y complementan a las de los materiales que se encuentran en la naturaleza o las de los sintetizados con técnicas químicas y físicas convencionales. Los metamateriales se construyen de forma artificial a partir de componentes microscópicos, y presentan una respuesta óptica asimilable a la de medios continuos sin estructura, cuyo manejo resulta sencillo al venir

descritos por constantes efectivas. El índice de refracción, definido por el cambio angular en la dirección de propagación de la luz al atravesar una superficie, es una de esas constantes sobre las cuales se han producido importantes avances, como la demostración experimental de medios de índice negativo en los que la dirección de difracción es contraria a la intuición. Este tipo de materiales pueden ser utilizados para fabricar lentes perfectas, capaces de formar imágenes con precisión superior a la impuesta por el límite de difracción, que impide resolver detalles inferiores a media longitud de onda (una fracción de la micra para luz visible). Otro ejemplo está representado por los materiales invisibles, indistinguibles del aire porque tienen su mismo índice de refracción. Recientemente se ha logrado un alto grado de invisibilidad en metales, opacos en general, pero que se tornan transparentes al ser perforados por redes periódicas de agujeros. La transmisión de luz a través de un solo agujero resulta enormemente reducida si este es pequeño en comparación con la longitud de onda. Sin embargo, el efecto cooperativo de una disposición periódica de agujeros induce resonancias que apilan la intensidad de la luz en las cercanías de los mismos, produciendo una transmisión neta cercana al 100%, al menos para rayos infrarrojos y agujeros nanoscópicos. Estos fenómenos se sustentan en general en el control del flujo luminoso a escala nanométrica (muy por debajo de la longitud de onda). Por ejemplo, en los llamados cristales fotónicos, donde el índice de refracción aparece modulado periódicamente en el espacio y donde la luz se comporta de manera análoga a los electrones sensibles a la disposición periódica de los átomos en el seno de un cristal sólido convencional. Emergen por tanto conceptos análogos a los de aislante y conductor eléctricos, pero para la luz. En este contexto se han construido guías de luz capaces de cambiar su dirección de propagación en distancias de tan sólo una micra, con el consiguiente potencial para reducir la presencia de componentes ordinarios en los circuitos ópticos tales como las fibras de sílice, portadoras de señales de teléfono, internet y televisión, y que requieren milímetros para lograr el mismo efecto. En otra vertiente, la fuerza de enlace entre moléculas se puede determinar ahora con facilidad gracias a las técnicas desarrolladas en el ámbito de la nanofotónica, pues las señales electromagnéticas ejercen fuerzas sobre los objetos, siendo capaces incluso de moverlos. Los conceptos de campo cercano, campo evanescente y resonancia son importantes en todos estos ejemplos. La nanofotónica se centra principalmente en el llamado campo

cercano, un término que se refiere a las distancias próximas a los objetos sobre los cuales la luz se refleja, se absorbe o se dispersa. En el campo cercano aparecen contribuciones de los llamados campos evanescentes, incapaces de propagar energía, y por tanto inmunes al conocido principio de conservación al que otros campos (los propagantes) están sometidos. Los plasmones de superficie ilustran claramente el concepto de campo evanescente, pues son excitaciones de electrones de conducción, similares a las de un plasma, que al no propagar energía en dirección perpendicular a la superficie están condenadas a vivir en sus inmediaciones. El estudio de la creación y el guiado de plasmones en superficies metálicas nanoestructuradas constituye el núcleo central de la plasmónica. Asimismo, existen plasmones en nanopartículas metálicas, observables en las bandas de absorción óptica. Al contrario que en superficies planas, los plasmones de nanopartículas pueden escapar de ellas por acoplamiento directo con la luz propagante. La longitud de onda de estos plasmones depende críticamente de la composición y morfología de las partículas. Actualmente, la propagación electromagnética causada por metamateriales plasmónicos nanoestructurados es una cuestión de enorme interés que está siendo investigada teóricamente y experimentalmente con el fin de comprender la física e investigar efectos novedosos de campo cercano y de campo lejano que podrían explotarse en una amplia gama de aplicaciones. Tales aplicaciones incluyen el desarrollo de dispositivos nano-ópticos novedosos para comunicaciones ópticas[6], para la captación de energía[7] y también para el desarrollo de dispositivos ultrasensibles para detectar biomoléculas.[8] Gran parte de este reciente descubrimiento ha estado impulsado por las mejorias continuas de las herramientas de nanofabricación que permiten crear y diseñar nano-objetos de alta calidad, por la mayoria hechos utilizando metals nobles como el oro o la plata. Los esfuerzos destinados a diseñar nuevos dispositivos nano-ópticos basados en la utilización de los plasmones están generando una multitud de avances básicos en conmutación óptica, biosensores, microscopía, etc. Además, hoy en día, muchas de las tecnologías emergentes utilizadas en bioquímica y en ciencia de los materiales se basan en la nano-fotónica, que utiliza la luz como un portador de información. Los componentes ópticos que son capaces de manipular la polarización y la intensidad de la luz, tales como rotores y aisladores no recíprocos, son ubicuos. Las mayores dificultades para la integración de componentes para la modulación de modos ópticos en guías de ondas o,

aún más prohibitivo, en los circuitos nano-fotónicos, son sus dimensiones macroscópicas. Dichos componentes son imprescindibles para la modificación de los modos ópticos, por ejemplo, a través de los efectos Kerr y Faraday con modulación magnética. Por lo tanto, se están haciendo esfuerzos considerables y crecientes para implementar nuevos diseños conceptuales que exploten eficientemente el control de la intensidad y de la polarización de la luz y para la propagación de los modos ópticos a través de metamateriales plasmónicos planos y nanoestructurados. Un abordaje muy prometedor para lograr este objetivo es explorar la propagación no recíproca de la luz mediante el diseño de materiales magneto-ópticos nanoestructurados que, combinando funcionalidades plasmónicas y magnéticas al mismo tiempo, muestren nuevos e inesperados fenómenos y funcionalidades que permitan la manipulación de la luz en la nanoescala.[9-34] La idea que subyace a la llamada magnetoplasmónica es que puede explotarse el gran confinamiento de fotones que se relaciona con la excitación de resonancias de plasma en combinación con las propiedades magnéticas del nano-objeto para aumentar y optimizar los efectos magneto-ópticos de los materiales ferromagnéticos existentes, lo que proporcionaría medios muy eficaces para controlar el flujo de luz. La actividad magneto-óptica se corresponde con los cambios en el estado de polarización y/o intensidad de la luz transmitida (efecto Faraday), reflejada (efecto Kerr), o más generalmente dispersada por un material, que son inducidos por la aplicación de un campo magnético externo. Los materiales ferromagnéticos muestran una importante actividad magneto-óptica con campos magnéticos bajos (< 0.5 T), lo que los convierte en los mejores candidatos para ser empleados en estos estudios. Por lo contrario, las oscilaciones de plasma en materiales ferromagnéticos suelen mostrar un mayor amortiguamiento que en los metales nobles, de manera que la estrategia común para superar este exceso de amortiguamiento es desarrollar estructuras híbridas que consisten en metales nobles y materiales ferromagnéticos, donde el metal noble aumenta la respuesta plasmónica del sistema.[12-21] Recientemente se ha demostrado que puede producirse el efecto de aumento magneto-óptico debido a la excitación de plasmones en nanoestructuras ferromagnéticas puras [35, 36], las cuales ofrecen como ventaja una mayor polarización magnética y una fabricación menos exigente. Además de los retos experimentales relacionados con el control preciso y simultáneo de las propiedades de los materiales, la fabricación y la caracterización óptica

en nanoescala, la exploración de todos estos efectos plantea cuestiones fundamentales de la magneto-óptica de materiales en la nanoescala. El trabajo de investigación presentado en esta Tesis se ha centrado en profundizar el estudio de fenómenos ópticos y plasmónicos en nanoestructuras ferromagnéticas puras. El trabajo aquí presentado está focalizado en la caracterización espectroscópica de materiales plasmónicos magneto-ópticos nanoestructurados, así como en el desarrollo de modelos teóricos para explicar y describir los efectos físicos observados en los experimentos. La finalidad de esta Tesis es comprender mejor la física subyacente a las relaciones mutuas entre el magnetismo, la actividad magneto-óptica y el acoplamiento de luz-materia en geometrías espacialmente confinadas en la nanoescala, y abrir el camino al diseño de nuevos materiales nanoestructurados para controlar magnéticamente la propagación de la luz. Estos nuevos materiales podrían tener un gran impacto en una amplia gama de aplicaciones tecnológicas importantes como almacenamiento magneto-óptico de datos, optoelectrónica, captación de energía para células fotovoltaicas y biodetección.

En concreto, después de una introducción sobre las propiedades ópticas y magneto-ópticas de los metales y nanoestrutura metalicas (Capitulo 1), en el Capítulo 2 de la Tesis se han estudiado nanoantenas de forma circular y elipsoidal de níquel. Dichas nanoantenas se fabricaron sobre sustratos dieléctricos transparentes con el método litográfico “Hole Mask Colloidal Lithography”, desarrollado en colaboración con el grupo del Prof. Alexandre Dmitriev (Gothenburg University). En CIC nanoGUNE se han medido las propiedades ópticas y magneto-ópticas de estas muestras, y se ha desarrollado un modelado teórico para reproducir los resultados experimentales, diseñar metamateriales magnetoplasmónicos y alcanzar un mejor control de sus propiedades ópticas y magneto-ópticas. En este sentido se han desarrollado “reglas de diseño” para obtener el control de la luz a través de nanoantenas magnetoplasmónicas de forma elíptica, donde ajustando los tres ejes de la elipse se pueden combinar varios modos plasmónicos a través del acoplamiento magneto-óptico. En el Capítulo 3 se ha estudiado la aplicación de estos metamateriales magnetoplasmónicos como sensores refractométricos y químicos ultrasensibles a nivel de molécula y/o proteína individual. La técnica de detección desarrollada está basada en un fenómeno llamado conversión de polarización, el cual se produce cuando la luz polarizada linealmente interactúa con

sistemas que presentan una anisotropía óptica o una actividad magneto-óptica (efecto Kerr o Faraday) produciendo una luz reflejada o transmitida que es elípticamente polarizada y tiene el plano de polarización rotado. Los resultados obtenidos muestran que si se mide la rotación del plano de polarización o la elipticidad de la polarización de la luz trasmitida/reflejada, se puede cuantificar de manera muy precisa la adsorción de moléculas y proteínas. Esta investigación se ha hecho en colaboración con el Dr. Keith Gregorczyk y el Prof. Mato Knez del grupo de Nanomateriales en CIC nanoGUNE. Ademas, durante una estancia de tres meses en el grupo de Nanobiofotónica en Chalmers University of Technology (Goteborgo, Suecia), se ha diseñado un experimento en colaboración con el Dr. Ruggero Verre para detectar la adsorción de neutravidina y biotina con diferentes concentraciones, basado su la tecnica mencionada antes. El Capítulo 4 presenta un estudio sobre sistemas magnetoplasmónicos nanoestructurados y ordenados en redes periódicas de nanoantenas ferromagneticas donde los efectos plasmónicos de las estructuras individuales interfieren coherentemente a través de efectos difractivos debidos al orden del retículo, produciendo un efecto colectivo llamado resonancia de superficie de retículo (lattice surface resonances). Para calcular la respuesta óptica y magneto-óptica de dichos sistemas se ha desarrollado un código basado en la aproximación de dipolo discreto (Discrete Dipole Approximation) en colaboración con el Dr. Luca Bergami y la Prof.ª Nerea Zabala de la UPV/EHU, y el Prof. Javier Aizpurua del CFM/CSIC-UPV. La combinación de cálculos analíticos y numéricos ha servido de soporte al diseño, fabricación y medición de sistemas ordenados de antenas de níquel con forma elíptica para obtener un control más eficaz de la respuesta magneto-óptica y un aumento de dicha respuesta comparado con los efectos estudiados en nanoestructuras no interagentes. Finalmente, en el Capítulo 5, se han estudiado experimentalmente y teóricamente, en colaboración con el Dr. Antonio García-Martín (Instituto de Microelectrónica de Madrid) y el Prof. Juan Carlos Cuevas (Universidad Autónoma de Madrid), las propiedades de plasmones propagantes en capas ferromagnéticas perforadas, donde se puede crear bandas plasmónicas que se pueden utilizar y combinar entre ellas para manipular y aumentar la respuesta magneto-óptica de dichos metamateriales.

Contents

Resumen i
Summary 1
1. Basics on plasmonics and magneto-optics in metallic nanostructures 5
1.1 Optical properties of metals 6
1.1.1 The Drude free electron model 9
1.1.2 Localized Surface Plasmon Resonances (LSPRs) 14
1.1.3 Surface Plasmon Polaritons (SPPs) 24
1.1.4 Plasmons in noble and ferromagnetic metals 28
1.1.5 Fano resonances 32
1.2 Magneto-Optical effects in metals 36
1.2.1 Historical introduction 36
1.3.2 Physical origins of magneto-optical effects: classical description 37
1.3.3 Microscopic description of the magneto-optical effects 44
1.3.4 Macroscopic formalism of Kerr and Faraday effects 46
2. Magneto-optics of ferromagnetic nanostructures supporting localized plasmons 49
2.1 Introduction 50
2.2 Plasmonic phase-tuning of magneto-optical effects 50
2.3 Longitudinal Kerr effect to increase magneto-optical tunability 59
2.4 Towards magnetoplasmonics in 3D-nanoantennas 65
2.5 Conclusions 67
3. Polarization conversion-based sensing schemes using plasmonic and magnetoplasmonic nanostructures 69
3.1 Introduction 70
3.2 Introduction to polarization conversion-based sensing 72
3.2.1 Magnetoplasmonic nanoantennas 72
3.2.2 Anisotropic noble metal-based nanostructures 74
3.3 Bulk refractometric sensing 78

3.3.1 Refractive index sensing with Ni nanoantennas 78
3.3.2 Real time refractive index sensing with Au dimers 79
3.4 Molecular-level detection experiments 82
3.5 Conclusions 92
4. Anisotropic nanoantenna-based magnetoplasmonic crystals 93
4.1 Introduction 94
4.2 Lattice surface modes in magnetic nanoantenna-based plasmonic crystals 95
4.3 Engineering of magneto-optical anisotropy 104
4.4 Conclusions 111
5. SPPs assisted magneto-optical activity in 2D magnetoplasmonic crystals 113
5.1 Introduction 114
5.2 Optical properties of 2D-MPCs supporting SPPs 115
5.3 Magneto-optical properties of 2D-MPCs 122
5.4 Polarization conversion tuning through plasmonic bands engineering 127
5.5 Conclusions 130
6. Conclusions and outlook 131
7. List of Publications 133
Appendix A (experimental methods) 135
A1 Optical and magneto-optical characterization 135
A2 Sensing experiments 138
A3 Fabrication processes 140
Appendix B (theoretical methods) 143
B1 Polarizability of a general ellipsoid 143
B2 Analytical expression for MOKE in elliptical nanodisks 148
B3 Couple Dipole Approximation (CDA) 149
B4 Optical response of plasmonic dimers 151
B5 Derivation of the Faraday and Kerr angles 155
Bibliography 159

Summary

Light-matter interaction has been studied during the last two centuries centuries with the aim of unveiling and exploiting the optical properties of materials. A very common technique based on this interaction is conventional microscopy, where small objects can be imaged by illumination with visible light (400-700 nm) and the images magnified with a system of lenses. Nevertheless, there are other devices or methods that enable the study of matter using light: for example, optical detectors and spectroscopy methods analyse light reflected from/transmitted by a sample in order to explore its structure, chemical composition and many other interesting features. However, the wave nature of light imposes a fundamental limit, called diffraction limit, which implies that light cannot be focused to dimensions smaller than roughly one half of the wavelength of light.[37] Therefore, many features of matter at the nanoscale remain unresolvable for conventional optics when using visible light. A promising way to overcome the diffraction limit is provided by the surface plasmons.[38, 39] The origin of plasmons is the coupling of the electromagnetic fields to the collective oscillations of the free electrons in conductive materials, such as metals. The key properties of plasmons are the capability to squeeze light in the vicinity of the metal, enhance electromagnetic field and confine energy at the nanoscale.[38] Consequently, nanoscale features become resolvable under the excitation of surface plasmons. These remarkable effects led to the foundation of a new research field called "Plasmonics", which seeks to control and manipulate light at the nanoscale and it is significantly growing in recent years. Plasmonics, and more in general Photonics, use light as an information carrier in optical communications, sensing, and imaging. Optical components that are able to manipulate light states such as rotators and non-reciprocal isolators are ubiquitous.[40-44] The difficulty for the integration of light−modulation components into waveguide optics or, even more prohibitive, into nanoscale photonic circuitry is their macroscopic dimensions. Such large components are needed for polarization modification, for example, via magnetically activated magneto-optical Kerr and Faraday effects. Thus, there are significant and growing efforts to implement new

conceptual designs for efficient polarization control of propagating optical modes with planar plasmonic metasurfaces.[4, 45-50] Within the paradigm of traditional magneto-optical materials, such as ferromagnetic metals, the rapidly developing field of magnetoplasmonics merges the concepts from plasmonics and magnetism to realize novel and unexpected phenomena and functionalities for the manipulation of light at the nanoscale.[9-34] Current advances in nanofabrication make it nowadays possible to design new classes of nanostructured systems combining magnetic and plasmonic functionalities. This allows exploring the nonreciprocal propagation of light, typical of ferromagnetic materials, by designing custom nanoscale magnetoplasmonic elements. As a result, investigations of surface plasmon resonances in such nanostructured systems are broadening our understanding of optics at the nanoscale. Initial studies on these structures were mainly focused on the enhancement of magneto-optical effects.[11, 12, 19, 21, 51-55] Moreover, the majority of studies in magnetoplasmonics commonly combine ferromagnetic materials with noblemetals[12-25, 31] in order to explore strong magneto-optical behavior together with reduced damping of plasmonic modes, respectively. Noble metals, such as gold and silver, display detectable magneto-optical effects under resonance conditions[56-58], although extremely high magnetic fields (> 1 T) are required. Nevertheless, also pure ferromagnetic nanostructures support surface plasmoncs with reasonably small damping. They are, thus, an ideal playground for studying effects arising from the excitation of surface plasmons and the simultaneous presence of a magneto-optical activity. Magneto-optical activity originates from spin-orbit coupling and is an intrinsic property of a material that cannot be freely and easily controlled. This Thesis aims to show that the excitation of surface plasmons in pure ferromagnetic nanostructures provides a pathway for tuning the magneto-optical response of a system beyond what is offered by the control of intrinsic material properties. The work presented here is focused on the design, fabrication and characterization of magneto-optical nanostructures supporting both localized and propagating plasmon resonances and on the exploration of their possible applications as, for instance, ultrasensitive single-molecule detectors.

In Chapter 1 a general overview on the optical properties of metals and metallic nanostructures supporting surface plasmons is presented. The concept of both localized

and propagating surface plasmons in both noble metals and ferromagnetic materials is introduced, as well as the concept of the so-called Fano resonances. Fano theory applies also in Plasmonics when, for instance, destructive or constructive interference between plasmonic modes and diffraction edges (Rayleygh's anomalies) in ordered systems takes place. A brief introduction on the magneto-optical properties of matter is also presented.

In Chapter 2 we explore the influence of the phase of localized surface plasmon resonances on the magneto-optical activity of nanostructured ferromagnetic materials. We first demonstrate that ferromagnetic nanoantennas support two or more simultaneous localized plasmonic modes, which are activated by an external static magnetic field. We show that these systems can be described as damped harmonic oscillators coupled by the spin-orbit interaction. We prove that the spin-orbit induced plasmons play an active role in determining the magneto-optical properties of these systems by controlling the relative amplitude and phase lag between the oscillators involved. Our theoretical predictions are fully confirmed by magneto optical Kerr effect and optical extinction measurements in nanostructures of different size and shape.

In Chapter 3 we propose a novel bio-chemo-sensing methodology, which enables radically improved sensitivity compared with recently reported plasmon-based sensors. Such a high sensitivity is achieved by exploiting the polarization conversion capabilities of both magneto-optically active nanoantennas and noble metal-based anisotropic metasurfaces.

In Chapter 4 we introduce a novel concept of magnetically tunable plasmonic crystal based on the excitation of Fano lattice surface modes in periodically arranged magnetic antennas that show anisotropic in-plane plasmonic responses. We demonstrate a significant strengthening of magneto-optical effects due to the coherent excitation of radiative far-field interactions between the nanoantennas as compared to a continuous film or metasurfaces made of randomly distributed nanoantennas.

Finally, in Chapter 5 we explore further the potential of the synergy between intrinsic magneto-optical mediated polarization conversion and plasmon excitations in ordered systems by substituting localized with propagating surface plasmon polaritons in

an archetypical 2D-magnetoplasmonic crystal made of periodic cylindrical holes in a ferromagnetic metallic layer. We demonstrate that an enhancement of the Kerr effect is induced when special non-collinear surface plasmon polariton modes, which couple to both p- and s-polarized light, are resonantly excited. We also show how the resonant enhancement of the Kerr effect can be set at desired radiation wavelengths and incidence angles by precise plasmonic band engineering achievable through the proper design of the magnetoplasmonic lattice structure.

We envisage that the concepts and the results presented in this Thesis will open up excellent nano-engineering opportunities towards enhanced and generally designed magneto-optical applications such as nanostructured magnetic-tunable metasurfaces for the control of light polarization states and improved nanoscale detection schemes.

1. Basics on plasmonics and magneto-optics in metallic nanostructures

In this introductory Chapter we present a general overview on the optical properties of metals and metallic nanostructures supporting collective electronic oscillation coupled to light, the so-called surface plasmons. We introduce the concept of both localized and propagating surface plasmons in noble metals and ferromagnetic materials. The latter posses the intrinsic property to change the light polarization by the application of an external magnetic field. Then, we introduce the concept of Fano resonances, which is used also in plasmonics to describe the interference between plasmonic modes and geometric resonances (Rayleygh's anomalies) in ordered systems. Finally we conclude with a theoretical introduction of the magneto-optical properties of matter.

1.1 Optical properties of metals

The wide-ranging optical properties observed in solid state materials can be classified into a small number of general phenomena. The simplest group, namely reflection, propagation and transmission[59], is illustrated in Figure 1.1. When light impinges on an optical medium, some of the light is reflected from the front surface, while the rest enters the medium and propagates through it. If any of this light reaches the back surface, it can be reflected again, or it can be transmitted through to the other side. The amount of light transmitted is therefore related to the reflectivity at the front and back surfaces and also to the way the light propagates through the medium.

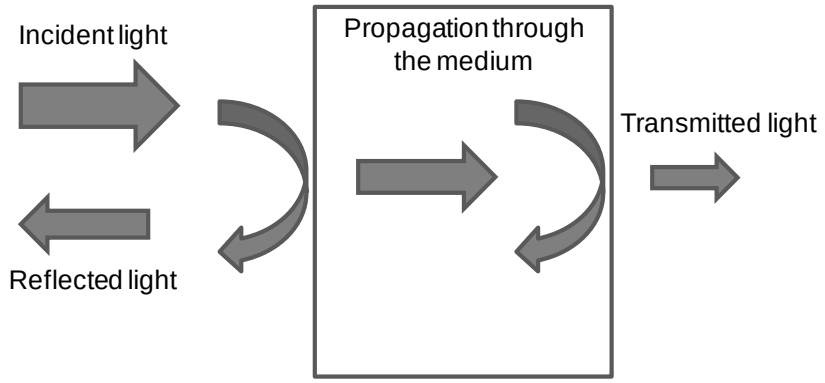

Figure 1.1: Reflection, propagation and transmission of a light beam incident on an optical medium.

The phenomena that can occur while light propagates through an optical medium are several. The most common are listed below.

- Refraction, which causes the light waves to propagate in a medium with a smaller velocity than in free space. In case of oblique (not normal) incidence, this effect leads to the bending of light rays at interfaces described by Snell's law of refraction. More in detail, this reduction of velocity is due to the "disturbance" caused by the electric field of the light on the charge distribution in the atoms/molecules of the material (in an insulator, like a dielectric, this does not

correspond to a electronic transition between two states, like in absorption or luminescence). This disturbance generates an electric dipole (or a variation of the dipole moment in atoms or molecules which are polar) that re-emits radiation at the same frequency but with a different phase. The re-emitted light adds up to the travelling wave causing a slowing down of the wave. Refraction does not affect the intensity of the light wave as it propagates.

- Absorption occurs during the propagation of light if its frequency is resonant with the transition frequencies of the atoms in the medium. The energy is retained by the material, so the transitions induced by light are non-radiative. In this case, the beam will be attenuated as it progresses. The transmission of the medium is clearly related to the absorption, because only unabsorbed light can be transmitted. Selective absorption is responsible for the colouration of many optical materials.

- Scattering is the phenomenon in which the light changes direction and possibly also its frequency (inelastic scattering) after interacting with the medium. After a scattering process, the number of photons going in the forward direction decreases because light is being re-directed in other directions. Scattering therefore has the same attenuating effect as absorption.

A number of other phenomena, like luminescence (spontaneous emission of light by excited atoms), can take place as the light propagates through the medium. Moreover, if the intensity of the beam is very high, nonlinear effects, such as frequency doubling, in which the frequency of part of a beam is doubled by interaction with the optical medium, can occur.

The classical approach to light propagation was developed at the end of the 19^{th} century following Maxwell's theory of electromagnetic waves and with the introduction of the concept of harmonic oscillator. The model assumes that there are several different types of oscillators within a medium, each with its own characteristic resonant frequency. The optical properties of metals at ultra-violet (UV), visible (VIS) and near-infrared (NIR) wavelengths can be described by a complex and frequency-dependent dielectric function $\varepsilon(\omega)$ that depends on the material properties. In metals, the conduction electrons

can move “freely" within the bulk of the material and interband excitations can take place if the energy of the photons exceeds the bandgap energy. This means that optical properties of metals are in general due to unbound electrons and, depending on the frequency ω of the incoming light, to bound electrons. The presence of an external electric field $\boldsymbol{E}(\boldsymbol{r}', t)$ leads to a macroscopic electric displacement in the material defined as

$$\boldsymbol{D}(\boldsymbol{r}, t) = \int \int_{-\infty}^{t} [\varepsilon_0(\boldsymbol{r}, \boldsymbol{r}', t)\boldsymbol{E}(\boldsymbol{r}', t) + \boldsymbol{P}(\boldsymbol{r}', t)]\, dt \tag{1.1}$$

where ε_0 is the dielectric constant of vacuum. The oscillating electric field $\boldsymbol{E}(\omega)$ causes the charges in the material (atomic nuclei and electrons) to slightly separate, inducing a local electric dipole moment $\boldsymbol{p} = \epsilon\langle \boldsymbol{r} \rangle$, where $\langle \boldsymbol{r} \rangle$ is the average displacement of the electron charge ϵ with respect to the ion (bound electron) or, in the case of free electrons, of the electron gas with respect to the approximated continuous and immobile positive charge distribution. Cumulative effect of all dipole moments (bound and unbound) results in a macroscopic density of the induced electric dipole moments in the material, called polarization density $\boldsymbol{P}(\boldsymbol{r}', t)$. Henceforth we consider only non-local effects, namely $\varepsilon(\omega)$ (from now on ε) does not depend on $\boldsymbol{r}$, and only stationary cases, that is ε does not depend on t. Within this approximation, Eq. (1.1) becomes

$$\boldsymbol{D} = \varepsilon_0 \boldsymbol{E} + \boldsymbol{P} \tag{1.2}$$

where

$$\boldsymbol{P}(\omega) = \boldsymbol{P}_b(\omega) + \boldsymbol{P}_{ub}(\omega) = \varepsilon_0(\chi_b + \chi_{ub})\boldsymbol{E}(\omega) \tag{1.3}$$

The quantity χ is the electric susceptibility, a dimensionless proportionality factor that indicates the degree of polarization of a material in response to an applied electric field: χ_b accounts for the bound electrons and χ_{ub} for the unbound ones. Greater is the electric susceptibility, greater is the ability of a material to polarize in response to the electric field, and thereby to screen the total electric field and store energy inside the material. Combining Eq. (1.2) and (1.3) we have that

$$\boldsymbol{D} = \varepsilon_0 \varepsilon_r \boldsymbol{E}(\omega) = \varepsilon_0 (1 + \chi_b + \chi_{ub}) \boldsymbol{E}(\omega) \tag{1.4}$$

where $\varepsilon_r = 1 + \boldsymbol{P}/\varepsilon_0 \boldsymbol{E}$ is the relative frequency-dependent dielectric response of the metal. The displacement $\langle \boldsymbol{r} \rangle$, the macroscopic polarization density $\boldsymbol{P}$ and the electric susceptibilities χ_b and χ_{ub} can be obtained by solving the equations of motions (for both unbound and bound electrons) under the influence of an external electromagnetic field. The different contributions of the unbound (free) and bound electrons to ε_r can be treated using a simple damped harmonic oscillator model.

1.1.1 The Drude free electron model

The Drude model of electrical conduction was proposed in 1900 by Paul Drude to explain the transport properties of electrons in materials. The model was extended in 1905 by Hendrik Antoon Lorentz and was supplemented with the results of quantum theory in 1933 by Arnold Sommerfeld and Hans Bethe.[60] This model, which allows us to compute χ_{ub}, is an application of the kinetic theory of ideal gases. The microscopic behavior of electrons in a solid is treated classically and looks like a pinball machine, with a sea of constantly jittering electrons bouncing and re-bouncing off heavier, relatively immobile positive ions as sketched in Figure 1.2. The Drude model neglects long-range interactions between the electrons and the ions and assumes that the electrons do not interfere with each other.

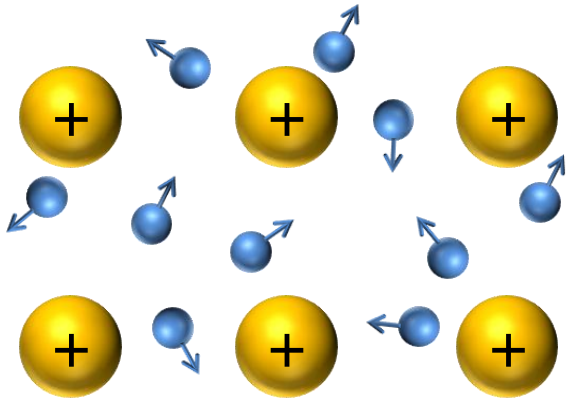

Figure 1.2: Schematic picture of a free-electrons system. The electrons (blue spheres) are free to move inside the material without feeling the attractive potential of the ions (yellow spheres). The arrows indicate the direction of the motion of the electrons.

In this picture the equation of motion is[37]

$$m_\epsilon \left(\frac{\partial^2 \boldsymbol{r}}{\partial t^2} + \Gamma \frac{\partial \boldsymbol{r}}{\partial t} \right) = \epsilon \boldsymbol{E} e^{-i\omega t} \tag{1.5}$$

where ϵ and m_ϵ are the electron charge and effective mass, respectively, and $\Gamma = 1/\langle\tau\rangle = v_F/l_\epsilon$ is the damping term, where v_F is the Fermi velocity, l_ϵ is the electron mean free path between scattering events and $\langle\tau\rangle$ is the relaxation time, which is the average time between two consequent scattering processes. If we solve Eq. (1.5) using the ansatz $\boldsymbol{r}(t) = r_0 e^{-i\omega t}$, and then we insert the obtained result into Eq. (1.3), assuming $\chi_b = 0$, we have that

$$\varepsilon_r(\omega) = \varepsilon_\infty - \frac{\omega_p^2}{\omega^2 + i\Gamma\omega} = 1 - \frac{\omega_p^2}{\omega^2 + \Gamma^2} + i\frac{\Gamma\omega_p^2}{\omega(\omega^2 + \Gamma^2)} \tag{1.6}$$

where $\omega_p = \sqrt{n\epsilon/m_\epsilon \varepsilon_0}$ is the bulk plasma frequency and ε_∞ summarizes the effect of the interband transitions due to bound electrons.[37] We note from Eq. (1.6) that the dielectric function is complex. It is worth mentioning that, since in a real system the electrons, even in metals although weakly, feel the potentials of the other electrons and the ions, the Drude model can be corrected to take into account this fact by replacing the electron mass with an effective mass, which accounts for the presence of these potentials.

Let's consider now the case of one of the most studied metals in plasmonics to develop novel nanotechnologies, namely gold (Au). The real and the imaginary parts of its complex dielectric function calculated with the Drude model are plotted in Figure 1.3(a) and 1.3(b) (solid lines), respectively. Note that the real part of the dielectric constant is negative. Note that, being the dielectric function of Au a complex number, the refractive index $\tilde{n} = n + ik = \sqrt{\varepsilon_r}$ has an imaginary part and so light can penetrate a metal only to a certain extent: k is called extinction coefficient and describes the dissipation of energy associated with the motion of electrons in the metal. The real part n affects only the velocity of the electromagnetic wave, that is, within the material, $c' = c/n$ and $\lambda' = \lambda/n$, whereas the frequency is the same $\omega = 2\pi c/\lambda$.

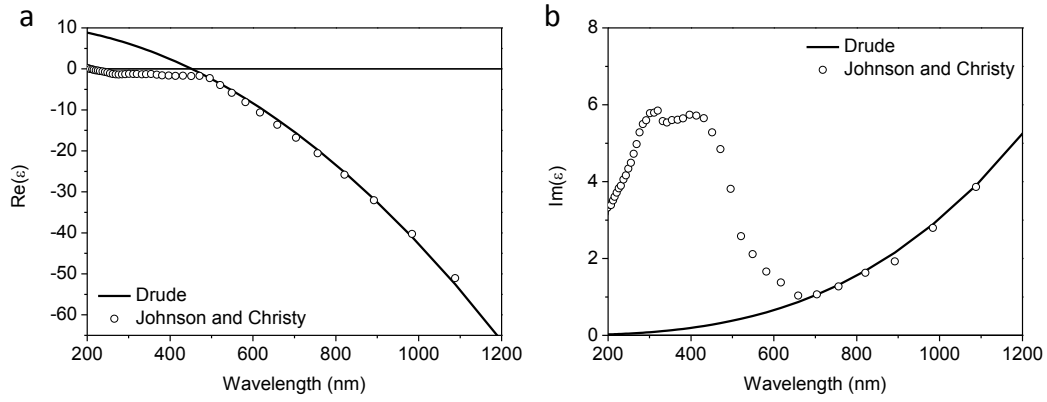

Figure 1.3: (a) Real and (b) imaginary part of the gold dielectric function according to the Drude model (solid lines, ω_p= 2.2 10^{15} s^{-1} and Γ = 1.7 10^{13} s^{-1} and ε_∞ = 11) and experimental values (circles) from Johnson & Christy[61] for the visible and near-infrared spectral range.

Although the Drude model gives quite accurate results for the optical properties of metals in the IR regime, it could need to be supplemented, especially in the VIS spectral range, by the response of bound electrons. For example, in the gold case considered here, at a wavelength shorter than 650 nm, the measured imaginary part of the dielectric function increases strongly and the real part remain negative along all the spectral region considered, and this is not predicted by the Drude theory (see the experimental dielectric function of gold (circles), taken from [61], plotted in Figure 1.3). This is because higher-energy photons can promote electrons of lower-lying bands into the conduction band. It is clear that, for gold, in the VIS part of the spectrum the contributions to ε coming from bound electrons are very relevant and they cannot be neglected. In the classical picture shown in Figure 1.4, such interband transitions may be described by exciting the oscillation of bound electrons, which are linked to the nucleus by the atomic forces represented by spring constants.

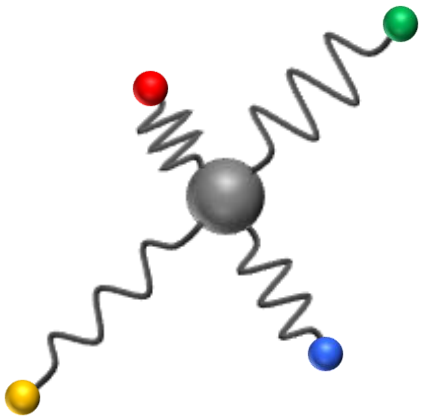

Figure 1.4: Classical model of the bound electrons in an atom. The grey sphere at the centre represents the nucleus, while the different bound electrons in a particular shell are represented by the colored spheres. The electrons are held to the heavy nucleus by springs, which represent the restoring forces due to the binding. Each atom has a series of characteristic resonant frequencies, which correspond to the quantized transition energies, or, from a classical point of view, to different spring constants.

The equation of motion for bound electrons existing in lower-lying shells of the metal atoms reads as

$$m_{\epsilon}^{eff}\left(\frac{\partial^2 \boldsymbol{r}}{\partial t^2}+\gamma\frac{\partial \boldsymbol{r}}{\partial t}\right)+\mu \boldsymbol{r}=\epsilon \boldsymbol{E}e^{-i\omega t} \tag{1.7}$$

Here m_{ϵ}^{eff} is the effective mass of the bound electrons, which is in general different from the mass of a free electron, γ is the damping constant, which, in the case of bound electrons, describes mainly radiative damping and tells us how slowly the oscillation dies out. The spring constant μ relates the restoring force exerted by a spring to the distance it is stretched by $F=-\mu x$, as it tends to restore the system to equilibrium. Using the same ansatz $\boldsymbol{r}(t)=r_0 e^{-i\omega t}$, the contribution of bound electrons to the dielectric function, for each shell, can be calculated as

$$\varepsilon_r(\omega)=1+\frac{\tilde{\omega}_p^2(\omega_0^2-\omega^2)}{(\omega_0^2-\omega^2)^2+\gamma^2\omega^2}+i\frac{\gamma\tilde{\omega}_p^2\omega}{(\omega_0^2-\omega^2)^2+\gamma^2\omega^2} \tag{1.8}$$

where $\tilde{\omega}_p=\sqrt{\tilde{n}\epsilon/m_{\epsilon}^{eff}\,\varepsilon_0}$ is introduced in analogy to the plasma frequency in the Drude model, being $\tilde{n}$ the density of the bound electrons in the considered shell, $\omega_0=\sqrt{\mu/m_{\epsilon}^{eff}}$ is the oscillator strength. Figure 1.5 shows the experimental Au dielectric constant[61] (real and imaginary part) compared with the calculated dielectric constant using Drude model (Eq. (1.6)) with ε_∞ = 7 and the same parameters used before, and one interband transition (Eq. (1.8)).

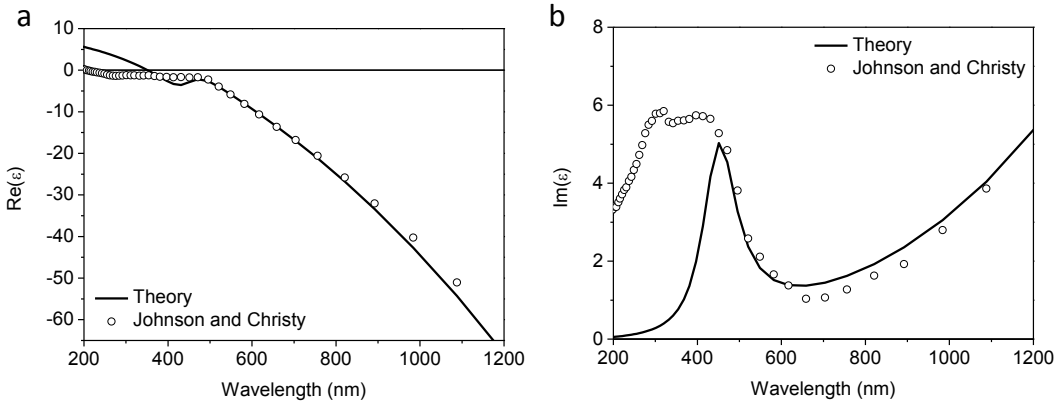

Figure 1.5: Dielectric function of gold, experimental values (circles) and model (lines). (a) imaginary part. (b) real part. Experimental values taken from [61]. The theoretical dielectric function is calculated taking into account the free electron contribution and the contribution of a single interband transition, where $\widetilde{\omega}_p$ = 6.8 10^{14} s^{-1}, γ = 1.45 10^{14} s^{-1}, and $\omega_0 = 2\pi c/\lambda$ with λ = 450 nm.

For wavelengths above 650 nm the behavior clearly follows the Drude theory. For wavelengths below 650 nm interband transitions become significant. Since only one interband transition is taken into account, the model curves still fail to reproduce the data below 500 nm. In general, by adding up Eq. (1.6) and the sum of all the interband transitions, we can fit perfectly the experimental values.[37, 62] For the ferromagnetic materials studied in the Thesis, namely nickel and permalloy (an alloy of iron and nickel), we can consider the optical response determined by the free electrons of the metal.

1.1.2 Localized Surface Plasmon Resonances (LSPRs)

Let's consider a nano-confined object like a sphere. When light impinges on the sphere, some energy of the electromagnetic field is transferred to it, and the rest follows its way. This removed energy manifests as the scattering, light radiated by the particle in all directions, and absorption, energy dissipated inside the particle through heating (Ohmic losses), as it can be seen in Figure 1.6. In general, absorption and scattering of light are

influenced both by the material properties and by the size and shape of the object. There is a macroscopic parameter that describes this dependence, which is called extinction cross section, defined as $\sigma_{ext} = \sigma_{abs} + \sigma_{scat}$, where σ_{abs} and σ_{scat} are the absorption and scattering cross sections, respectively. The cross sections account for the probability that absorption and scattering can take place at a certain wavelength, and they have the unit of an area. We can define also the so-called efficiencies Q_{abs}, Q_{scat} and Q_{ext}, which are the cross-sections divided by the geometrical area of the object, which, in the case of a sphere is πr^2.

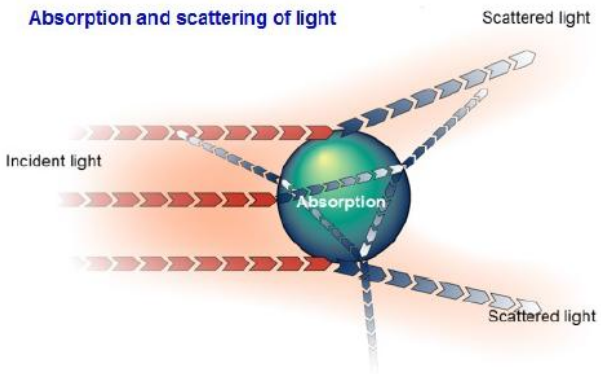

Figure 1.6: Schematics of scattered and absorbed light after incident light reaches a nanoparticle.

Let's first consider a metallic sphere characterized by a frequency dependent dielectric constant $\varepsilon_r(\omega)$ and embedded in a dielectric surrounding medium like vacuum or air (n = 1). Through the application of an external electromagnetic field, we can excite the so called localized surface plasmon resonances (LSPRs) in the sphere, which are peculiar excitations arising from spatial confinement. Usually a resonance is thought to be an enhancement of the response of a system to an external excitation at a particular frequency. It is referred to as the resonant frequency or natural frequency (eigen-frequency) of the system. A resonance can be simply explained by the means of a harmonic oscillator with periodic forcing. When the frequency of the driving force is close to the eigen-frequency of the oscillator, the amplitude of the latter is growing

toward its maximum value, which is a finite number due to the intrinsic damping of the system. Often many physical systems may also exhibit the opposite phenomenon when their response is suppressed if some resonance condition is met which has lead to the term anti-resonance. The dielectric function $\varepsilon_r(\omega)$ describes the optical bulk properties of the material, while if we have a confined object like a sphere, we have to take into account the spatial confinement of that material. Let's assume that the sphere is so small such that the polarization density inside can be considered uniform. This assumption is certainly valid if the sphere radius r is $\ll \lambda$. Thus the total field inside the particle is

$$\boldsymbol{E}_{int} = \boldsymbol{E}_0 + \boldsymbol{E}_d \tag{1.9}$$

where $\boldsymbol{E}_0$ is the external applied electric field, and $\boldsymbol{E}_d$ is the depolarization field, which tends to oppose the action of $\boldsymbol{E}_0$ and it is due to the finite size of the particle, as shown in Figure 1.7. It can be demonstrated that, in the case of a sphere, a uniform applied field $\boldsymbol{E}_0$ produces a uniform internal field $\boldsymbol{E}_{int}$. The same can be assumed, under certain conditions (weak Eshelby's conjecture)[63], also for a general ellipsoid. If P_x, P_y and P_z are the components of the polarization density $\boldsymbol{P}$ referred to the principal axes of an ellipsoid (for a sphere all the directions are principal axes), then the components of the depolarization field are written as[64]

$$E_d^i = -\frac{L_i P_i}{\varepsilon_0 \varepsilon_m} \tag{1.10}$$

where ε_m is the dielectric constant of the surrounding medium (in this case ε_m = 1), and L_i is the so-called depolarization factor, with $i = x, y, z$. For a sphere $L_i = 1/3, \forall\, i$.

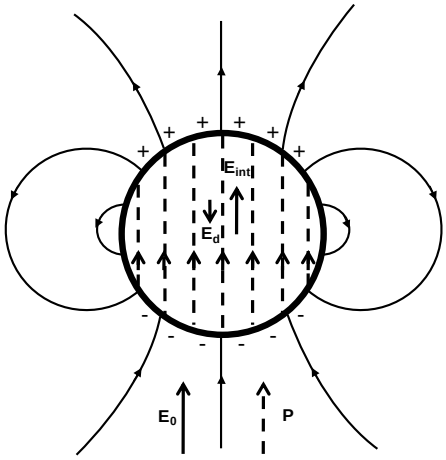

Figure 1.7: The dipolar field of a uniformly polarized sphere.

Thus the total polarization of such sphere is

$$\mathbf{P} = (\varepsilon - \varepsilon_0 \varepsilon_m)\left(V\boldsymbol{E}_0 - \frac{\mathbf{P}}{3\varepsilon_0 \varepsilon_m}\right) \tag{1.11}$$

where $\varepsilon = \varepsilon_r \varepsilon_0$, and **P** and $V = 4\pi r^3/3$ are the polarization and volume of the sphere, respectively. Solving Eq. (1.11) for **P** we get

$$\mathbf{P} = \varepsilon_0 V \frac{3(\varepsilon_r - \varepsilon_m)}{(\varepsilon_r + 2\varepsilon_m)/\varepsilon_m}\boldsymbol{E}_0 = \varepsilon_0 \alpha \boldsymbol{E}_0 \tag{1.12}$$

where the proportionality constant α between **P** and $\boldsymbol{E}_0$ in the expression on the right is called polarizability. The physical mechanism behind Eq. (1.12) is that when a small spherical nanoparticle is illuminated by light, the oscillating electric field causes the conduction electrons to oscillate coherently. This is schematically pictured in Figure 1.8(a).

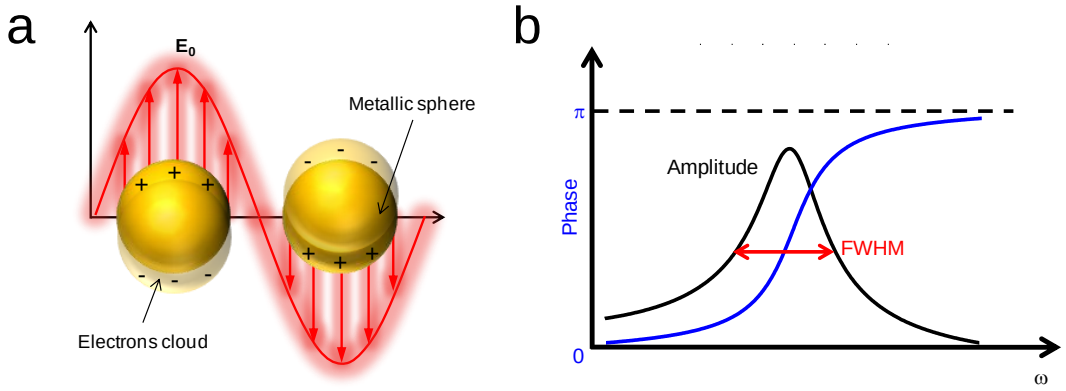

Figure 1.8: (a) Sketch of the dipolar electronic motion under the application of an external electromagnetic field. (b) Amplitude, characterized by a full width at half (FWHM), and phase of the electronic motion close to the resonant condition. The phase of the motion exhibits a jump of π at the resonance.

At a certain wavelength (or range of wavelengths), depending on the intrinsic optical properties of the material considered and on the size of the sphere, this motion becomes resonant, namely when $Re(\varepsilon_r) = -2\varepsilon_m$ (Fröhlich condition), giving rise to a LSPR. Usually the collective oscillation of the electrons is a dipole-like oscillation, as described by Eq. (1.12). In general higher modes, both even and odd, are allowed and can be excited. In the case of a small sphere, all the excitable modes can be calculated using the analytical theory developed by Mie.[64] Note that the polarizability is in general a complex number, meaning that the polarization does not have to exactly follow the electric field. In the framework of a forced harmonic oscillator model, it is known that the phase of the oscillator exhibits a π jump at the resonance frequency ω_0, meaning that below the resonance ($\omega < \omega_0$) the oscillator is in phase with the driving force, and it becomes out of phase above the resonance ($\omega > \omega_0$). Indeed, the phase of the calculated polarizability exhibits a jump of π at the resonance, meaning that below the resonance (higher wavelengths) the electron motion is in phase with the driving field, and it becomes out of phase above the resonance (lower wavelengths), as sketched in Figure 1.8(b). The approximated method presented here, also known as quasi-static approximation, considers the interaction of light with a spherical particle that is smaller than the

wavelength of the light. Under these circumstances, the electric field of the incident light can be considered constant inside the particle. Noteworthy, in the case of metallic nanostructures, one should take into account also radiative losses, but this contribution will be considered later when we will expand the quasi-static approximation to objects where r is comparable with λ. The link between α and the absorption and scattering cross sections is provided through the Optical Theorem and reads[64, 65]

$$\sigma_{scat}(\omega) = \frac{k^4}{6\pi}|\alpha(\omega)|^2 \tag{1.13}$$

$$\sigma_{abs}(\omega) = kIm[\alpha(\omega)] \tag{1.14}$$

The samples studied in this Thesis are characterized by dimensions comparable with the wavelength of the incident light. For larger sphere volumes, viz., radius r no longer $<< \lambda$, the quasi-static approximation has to be reviewed as the electric field inside the nanoparticle cannot be considered homogeneous anymore. Moreover, in the case of larger objects, higher modes of plasmon excitation can occur[66], such as the quadrupole mode, where half of the electron cloud moves parallel to the applied field and half moves antiparallel, although in what follows we consider only dipolar excitations. In noble metal spheres, when the order of magnitude of the radius is comparable with the wavelength of the incoming light, the position of the LSPR red-shifts to higher wavelengths and the width of the resonance is severely broadened.[67, 68] In this case depolarization effects due to the large size of the object appear, and so some corrections to Eq. (1.12) have to be done. The polarizability of the sphere is determined using a self-consistent derivation, known as Meier and Wokaun long wavelength approximation (MWLWA), that is a correction to the quasi-static approximation to account for the size of the particle and it is usually employed to calculate far-field properties, such as the extinction cross section. The approximation introduced by Meier and Wokaun's is based on the assumption that the polarization **P** is homogeneous within the sphere volume or, in other words, the sphere can be considered as a point dipole, like in the quasi-static approximation, in spite of its finite dimensions. For the cases treated in this Thesis, far from the sphere one sees a

dipole, so this is certainly a right and legitimate idea. Of course the MWLWA does not describe properly the field distribution if one goes closer, where the sphere is not a point dipole but a rather complicated distribution of charges that should be described by a multipole expansion. But as far as we interested in far field properties, this is almost exact and describe very well the experimental results presented in the following Chapters. In the framework of the MWLWA, the field $\boldsymbol{E}_d$ is determined starting from the infinitesimal contribution $d\boldsymbol{E}_d$ generated in the centre of the sphere by the dipole moment $d\mathbf{p}(r) = \boldsymbol{P}dV(r)$, and integrating over the sphere volume (for a detailed derivation see Appendix B1). For a sphere with radius r we have[67]

$$\boldsymbol{E}_d = \left(-1 + r^2k^2 + i\frac{2r^3k^3}{3}\right)\frac{1}{3\varepsilon_0\varepsilon_m}\boldsymbol{P} \tag{1.15}$$

The first term is the static (related to the shape of the object) contribution to the depolarization field: this term is the most important if $r << \lambda$, and it is the term that, in the quasi-static approximation, gives Eq. (1.12). The second term, dependent on the size of the object, is called the dynamic depolarization term, and it is responsible for the red-shift of the resonance at large volumes. It accounts for the frictional action on the electrons due energy irradiated while oscillating. The last term, also dependent on the size of the object, represents the radiation-damping correction to the electrostatic solution: it accounts for the damping of the dipole by radiative losses and results in a broadening of the resonance peak for large particle volumes. Finally, the corrected polarizability reads

$$\alpha_{MWLWA} = \frac{3\varepsilon_m(\varepsilon_r - \varepsilon_m)V}{3\varepsilon_m + \left(1 - r^2k^2 - i\frac{2r^3k^3}{3}\right)(\varepsilon_r - \varepsilon_m)} \tag{1.16}$$

One can obtain a similar expression also for a general ellipsoid, where all three the principal axes are different, but the integrals of the fields have to be solved numerically as

there is no analytical solution in the case of a general ellipsoid (for more details see Appendix B1). In Figure 1.9 we plot the normalized extinction cross section for a 40 nm radius gold sphere in vacuum, calculated with Eq. (1.16). We used ε_r values calculated using the Drude model with the same parameters used to calculate the curves in Figure 1.3 (blue curve) and tabulated ones[61] (red curve).

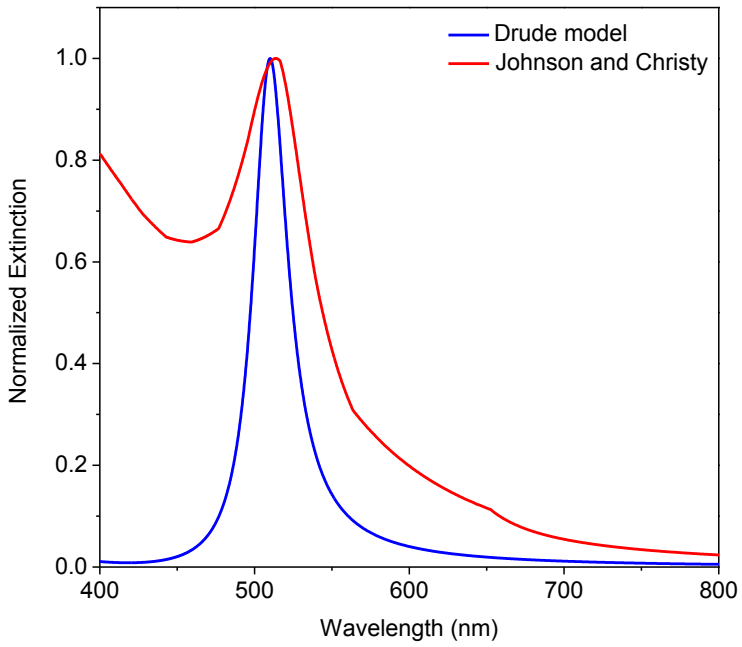

Figure 1.9: Normalized extinction cross section for a 40 nm radius gold sphere in vacuum, calculated with Eq. (1.16) using the Drude model (blue curve) and the tabulated data[61] (red curve).

1.1.2.1 Characteristics of near and far-field regions

The electric fields scattered by a metallic nanoparticle or a metallic surface are commonly separated into two regions: the near-field and the far-field region. These two regions are separated by an intermediate region, called mid-field region.In what follows, they will be defined with the example of an oscillating dipole, whose electric field $\boldsymbol{E}$ fields can be described analytically as follows[69]

$$\boldsymbol{E} \propto \left\{ k^2(\boldsymbol{n}\times\boldsymbol{p})\times\boldsymbol{n}\frac{e^{ikr}}{r} + [3\boldsymbol{n}(\boldsymbol{n}\cdot\boldsymbol{p})-\boldsymbol{p}]\left(\frac{1}{r^3}-\frac{ik}{r^2}\right)e^{ikr}\right\} e^{-i\omega t} \tag{1.17}$$

This solution takes simple forms in the limit of being either very close or very far from the point dipole. In the far-field region ($r \gg \lambda$) the electric field takes on the limiting form

$$\boldsymbol{E} \propto k^2(\boldsymbol{n}\times\boldsymbol{p})\times\boldsymbol{n}\frac{e^{ikr}}{r}e^{-i\omega t} \tag{1.18}$$

This equation describes spherical waves where the electric field $\boldsymbol{E}$ and the magnetic field $\boldsymbol{H}$ are perpendicular to each other. These waves are propagating waves because of the term $e^{ikr-i\omega t}$. In the near-field region ($r \ll \lambda$), the fields of an oscillating electric dipole can be approximated by

$$E \propto (3\boldsymbol{n}(\boldsymbol{n}\cdot\boldsymbol{p})-\boldsymbol{p})\frac{1}{r^3}e^{-i\omega t} \tag{1.19}$$

This equation describes quasi-static, strong field, also called near-field. Near-fields do not contain any term which is descriptive of a wave-like propagation phenomenon, and they oscillate in time with $e^{-i\omega t}$. Near-fields decay with a rate of $1/r^3$ and do not irradiate energy from the dipole. In Figure 1.10(a) we show the spatial decay of the different contributions to the electric field of an oscillating dipole. In Figure 1.10(b) the electric field distribution of the far-field and the near-field region for an electric dipole aligned along the z-direction, are shown.

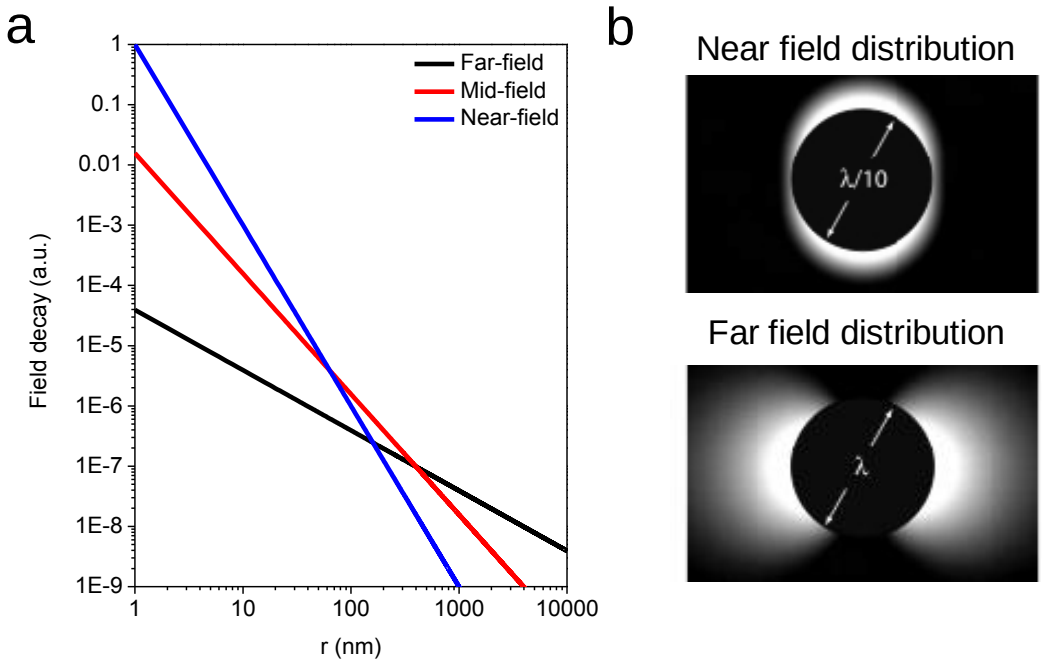

Figure 1.10: (a) Spatial decay of the far-, mid- and near-field, with $k = 2\pi/\lambda$, and λ = 500 nm. (b) Electric field amplitudes of an electric dipole. Top-panel: near-field. Bottom-panel: far-field. The black disk of given radius masks the field around the electric dipole which would saturate with the used color scale.

Far fields are propagating waves in the sense of Maxwell's equations and thus can propagate forever, e.g. even in the case that the source is switched off. Likewise, extracting power from the radiated fields has no effect on the source. This is a The near-fields are reactive fields or storage fields, meaning that they store the energy that drives the dipole oscillation in nanoparticles. Therefore, the near fields extinguish when the source is turned off.

1.1.3 Surface Plasmon Polaritons (SPPs)

Surface plasmon polaritons (SPPs) are electromagnetic excitations propagating at the interface between a dielectric with ε_d and a conductor with ε, evanescently confined in the perpendicular direction (Figure 1.11). These electromagnetic surface waves arise via the coupling of the electromagnetic field of light to oscillations of the metal electron plasma. The electromagnetic field generated by this coupling, decays exponentially from the interface, which makes the SPPs a bound mode propagating along the interface.[70] The dispersion of SPPs can be found by solving Maxwell equations assuming surface waves and the appropriate boundary conditions.[38] For a planar interface between a dielectric with $Re(\varepsilon_d) > 0$ and a metal with $Re(\varepsilon) < 0$, the dispersion relation is given by

$$k_x = k_0 \sqrt{\frac{\varepsilon \varepsilon_d}{\varepsilon + \varepsilon_d}} \tag{1.20}$$

where the wave-vector k_x in propagation direction (here assumed to be the *x*-axis) is expressed as a function of the dielectric constants of the metal and of the dielectric, and $k_0 = 2\pi c/\lambda$ is the light wave vector in vacuum.

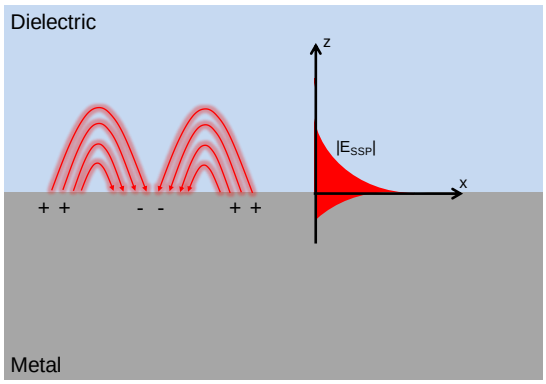

Figure 1.11: SPP propagating in *x*-direction along a flat interface between a dielectric ($Re(\varepsilon_d)$ > 0) and metal ($Re(\varepsilon)$ < 0).

The SPP dispersion expressed by Eq. (1.20) is illustrated in Figure 1.12, where we assume a metal/air interface.

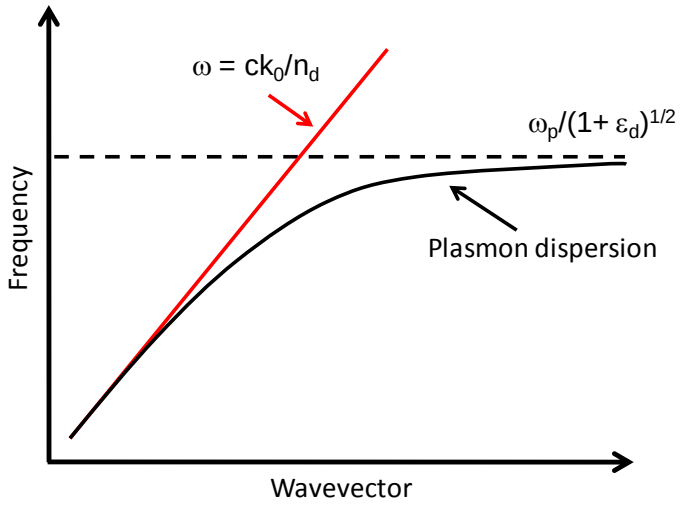

Figure 1.12: Dispersion curve of a metal-air interface, showing the real part of k_x (black line) of the SPP wave vector as a function of frequency ω. The red line is the light line in vacuum k_0. The dashed line is the metal surface plasmon resonance frequency ω_p.

The field confinement perpendicular to the surface can be obtained by considering the out of plane component of the wave-vector in each medium, which for a SPP at a flat interface is given by[37]

$$k_{z,d} = k_0 \sqrt{\frac{\varepsilon_d^2}{\varepsilon + \varepsilon_d}} \qquad \text{in the dielectric}$$

$$k_{z,m} = k_0 \sqrt{\frac{\varepsilon^2}{\varepsilon + \varepsilon_d}} \qquad \text{in the metal}$$

The field confinement is given as the $1/e$ decay length of the SPP electric field in z-direction and can be obtained by evaluating $L_z = 1/Im(k_z)$. At VIS frequencies the decay length L_z into the dielectric is much shorter than the free-space wavelength λ_0, namely in the order of 10-100 nm, and even less in the metal. Thus, at VIS wavelengths we can employ SPPs for confining fields to the surface. This finds applications in magneto-optical data storage, chemical sensing and spectroscopy[71, 72], biomedical application and miniaturized photonic circuits[39, 73]. The SPP field also penetrates the metal for a few tens of nanometers for both VIS and NIR spectral regions. Because the metal is lossy, energy of the SPP wave is dissipated in the metal. This leads to a damping of the SPP wave in propagation direction, which is described by the propagation length $L_x = 1/Im(k_x)$, defined as the length scale over which the field amplitude of the SPP has decayed to $1/e$.

1.1.3.1 Excitation of SPPs in metals

The excitation of SPPs on a metal-air interface requires the conservation of energy and momentum. Since at any frequency the SPP wave vector $k_x > k_{||} = k_0 sin\theta$, where θ is the angle of incidence, a direct excitation of SPPs via free space radiation is not achievable (Figure 1.12). On the other hand, it is possible to excite SPPs in a three-layer system consisting of a thin metal film sandwitched between two insulators of different dielectric constants. We take one of the insulators to be air ($\varepsilon_1 = 1$). A beam reflected at the interface between the insulator of higher dielectric constant ε_2, usually in the form of a prism (see Figure 1.13(a)), and the metal, will have an in-plane momentum $k_x = k_2\sqrt{\varepsilon_2} sin\theta_{TR}$, where θ_{TR} is the angle of the total internal reflection. This coupling scheme – also known as attenuated total internal reflection or prism coupling – is sufficient to excite SPPs at the metal/air interface (Figure 1.13(b)). Note that phase-matching to SPPs at the prism/metal interface cannot be achieved, since the respective SPP dispersion lies outside the prism light cone. Two different geometries for prism coupling are possible (Figure 1.13(a)). The most common configuration is the Kretschmann method (left panel in Figure 1.13(a)). Photons from a beam impinging from

the glass side at an angle $\theta > \theta_{TR}$ tunnel through the metal film and excite SPPs at the metal/air interface. The other geometry is the Otto configuration (right panel of Figure 1.13(a)), in which the prism is separated from the metal film by a thin air gap. Total internal reflection takes place at the prism/air interface, exciting SPPs via tunneling to the air/metal interface.

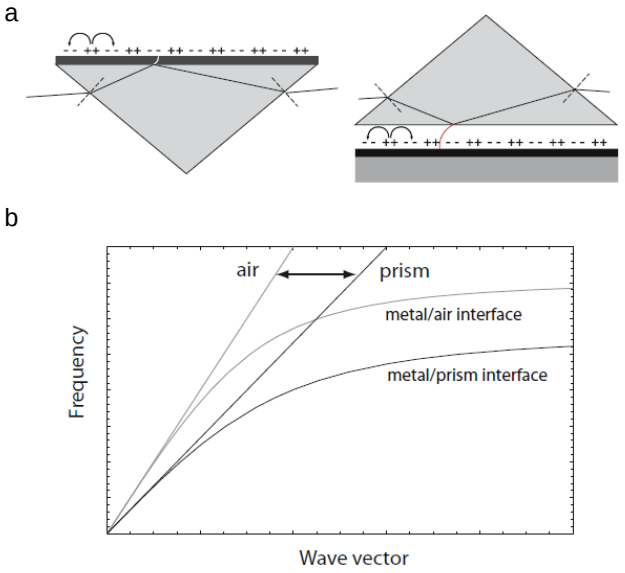

Figure 1.13: (a) Prism coupling to SPPs using attenuated total internal reflection in the Kretschmann (left) and Otto (right) configuration. (b) SPP dispersion. Only propagation constants between the light lines of air and the prism (usually glass) are accessible. Taken from [38].

The mismatch in wave-vector between the in-plane momentum of the impinging photons and the SPP wave-vector can also be overcome by patterning the metal surface with a shallow grating of grooves or holes with lattice constant a. For the simple one-dimensional grating of grooves depicted in Figure 1.14, phase matching takes place whenever the condition (grating equation) $k_{SPP} = k_x sin\theta \pm mg$ is fulfilled. Here $g = 2\pi/a$ is the reciprocal vector of the grating, and $m = (-i, \ldots, i)$ with i an integer

number. This configuration will be used in Chapter 5 to excite SPPs modes in a two-dimensional nanostructured ferromagnetic thin film.

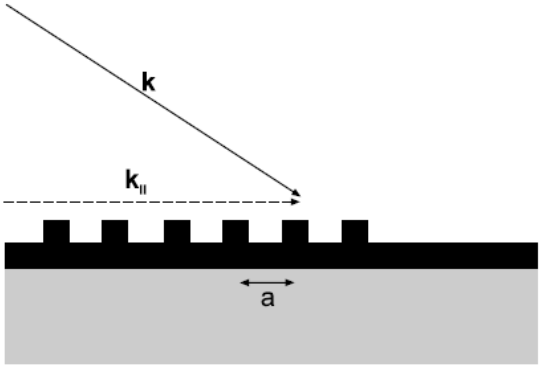

Figure 1.14: Phase-matching of light to SPPs using a grating. Taken from [38]

1.1.4 Plasmons in noble and ferromagnetic metals

The common materials used in plasmonics are noble metals such as Au or Ag. Since in this Thesis we deal with pure ferromagnetic nanostructures, a comparison with the best plasmonic materials has to be done to frame ferromagnetic materials in plasmonics. It is well known that the dielectric constant of metals is linked to the conductivity (or the resistivity) of the material. The way electrons respond to an electric field, the friction they encounter when they are pushed to move inside the metal by an external stimulus, determine also their behavior when they interact with light. From an electronic point of view, and in the framework of the Drude free-electron model, noble metals are characterized by a lower electron density and a higher relaxation time if compared to ferromagnetic materials, whose electron density is one order of magnitude higher than that of noble metals, and their relaxation time is very small (higher damping) if compared to that of noble metals.[60] This leads to a higher conductivity (lower resistivity) in noble metals and to a lower conductivity (higher resistivity) in ferromagnetic materials. The

repercussions of this difference can be easily seen when measuring the main optical quantities defined in the above sections, namely absorption and scattering cross sections, propagation lengths, etc. For instance, in the case of LSPRs, noble metal-based nanostructures are characterized by substantially narrower and more intense resonant peaks when compared to ferromagnetic nanostructures. The differences in the shape and strength of the LSPRs of noble metals and ferromagnetic materials can be explained just in terms of different relaxation time/damping constant, as shown in Figure 1.15. Moreover, because of the strong damping in ferromagnetic materials at VIS and NIR wavelengths, the SPP propagation length for these materials is limited to the order of the micrometer, while in the case of noble metals can reach hundreds of micrometers[37, 74] , as shown in Figure 1.16 where plot propagation lengths of Ni, Co, Ag and Au.

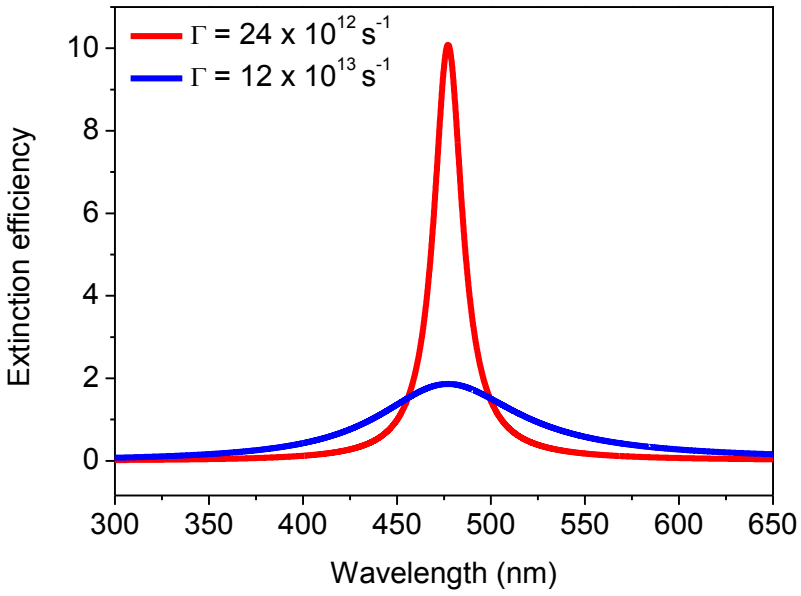

Figure 1.15: Extinction efficiency of a metallic sphere with r = 20 nm, calculated using Drude model in the quasi-static approximation (Eq. (1.12), with ε_∞ = 1, ω_p = 1.09 x ^{15} s^{-1}), varying the value of the damping constant Γ.

Another difference is that, while noble metals absorb a lot under 500 nm, above this wavelength they start to be almost perfect Drude-metals. As we move away from the VIS range, the efficiency of light scattering process increases progressively and overcomes that of the absorption process. On the contrary, in ferromagnetic nanostructures the scattering efficiency is one order of magnitude lower than those of noble metals and remains comparable with the absorption efficiency.

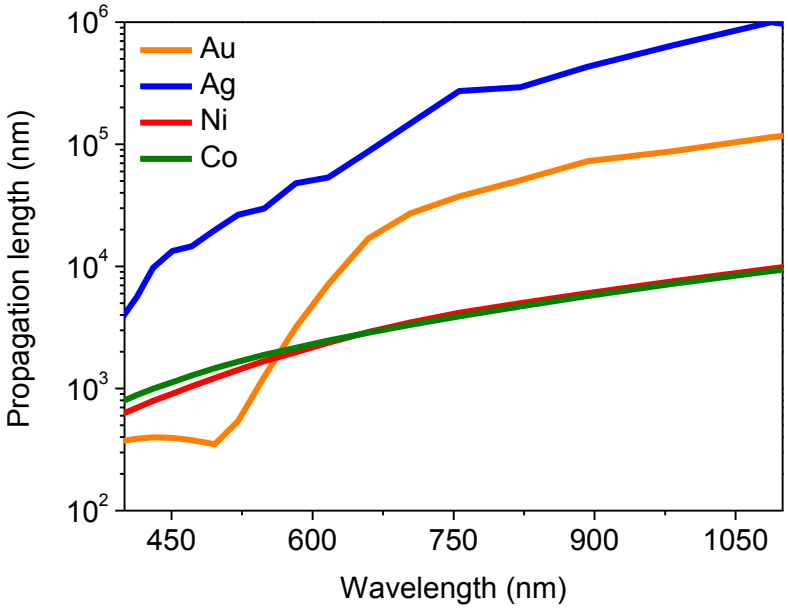

Figure 1.16: Propagation lentgh of a continuous Au, Ag [61] and Ni and Co [75].

Another important comparison between noble and ferromagnetic metals can be done analyzing a parameter called quality factor (Q-factor), which is a dimensionless parameter that describes how damped an oscillator or resonator is. The common definition of the Q-factor is the resonance wavelength λ_0 divided by its full width at half maximum, i.e., $Q = \lambda_0/FWHM$. Higher Q indicates a lower rate of energy loss relative to the stored

energy of the resonator (the oscillations die out more slowly). The Q-factor, for materials where only ohmic losses are considered, can be defined also as follows[76]

$$Q = \frac{\omega \frac{dRe(\varepsilon)}{d\omega}}{2Im(\varepsilon)} \tag{1.21}$$

In Figure 1.17 the Q-factors of Au, Ag, Co and Ni calculated using Eq. (1.21) are plotted. While the real part of the dielectric constant of noble metals and ferromagnets are comparable in terms of magnitude, the imaginary part, which represent the power of absorption of the material, is higher for the latter. This explains why the Q-factor is higher for noble metals if one looks at Eq. (1.21).

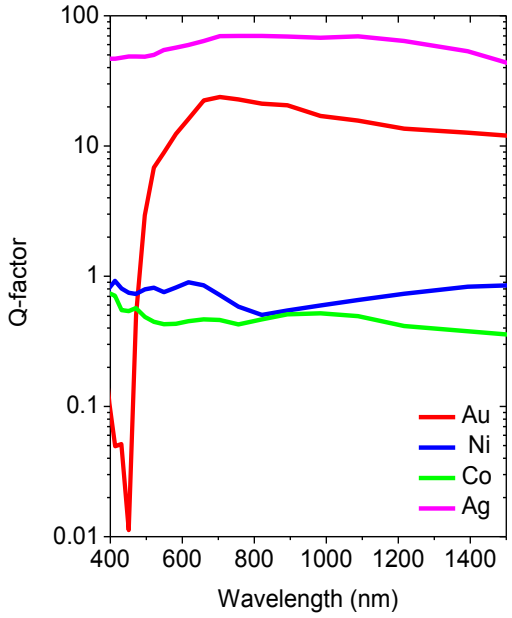

Figure 1.17: Q-factor of Au and Ag (constants taken from [61]) and Ni and Co (constants taken from [75]).

A high Q-factor is often desirable as it leads to stronger local-field enhancement.[76] In this sense the Q-factor is also an indicator of the sensitivity of a metal nanoparticle to the local environment. In LSPR-based sensing the main quantities analyzed are the peaks of SPPs and LSPRs both in reflection and transmission geometries. The width of these resonances is an indicator of the performance of the sensors. Ferromagnetic materials present broad and less intense resonances compared to noble metals, so they are not, in this framework, the best candidates to be used as sensors. In Chapter 3 we will introduce a novel approach to sensing based on the analysis of the light polarization, showing that extremely good performances of sensing can be achieved using also ferromagnetic materials, in spite of their lower Q-factor. Noteworthy, while noble metals represent the best candidates to be integrated in photonic circuits, they are also passive in terms of response to different external sources, such magnetic fields. On the contrary ferromagnetic materials can change their optical response under the application of an external magnetic field. This property can be used, for instance, to modify the dispersion relation of SPPs.[17]

1.1.5 Fano resonances

The first observation of the so-called Fano resonances in plasmonic systems, namely asymmetric line shapes in the absorption, transmission or reflection spectra of subwavelength metallic materials, can be traced back to 1902, when Wood observed unexpected narrow bright and dark bands in the spectrum of a reflection grating.[77] Wood saw that under special illumination conditions the grating efficiency in a given order dropped from maximum to minimum illumination, within a wavelength range not greater than the distance between the sodium D-lines (doublet separated by approx 0.4 nm).[78] These rapid variations in intensity were termed anomalies since the effects could not be explained by the conventional grating theory. Rayleigh proposed the first explanation for the existence of the anomalies: an anomaly in a given spectrum occurs at the wavelength for which a scattered wave emerges tangentially to the grating surface. [79] The Rayleigh

conjecture was considered as a valuable tool for the prediction of Wood's anomalies. Indeed, the famous (purely geometrical) grating formula

$$\sin(\theta_m) = \sin(\theta) + \frac{m\lambda_0}{nd} \tag{1.22}$$

allows one to rigorously calculate the diffraction angle of any scattered order m from the grating period, the angle of incidence and the wavelength of light. In Eq. (1.22) θ is the angle of incidence (measured anticlockwise from the normal to the grating), θ_m is the angle of diffraction (measured clockwise), λ_0 is the wavelength in vacuum (which can also be considered as the wavelength in the air), n is the refractive index of the embedding medium and d is the grating period. The passing-off of the order m occurs when $sin\,(\theta_m) = \pm 1$ and thus, from Eq. (1.22), the wavelengths of a spectrum generating the passing-off of a diffracted order are given by $m\lambda/nd = -sin\,(\theta) \pm 1$ $(m = \pm 1, \pm 2, \pm 3\ldots)$. The discrepancy of about 5% with the real location of anomalies was justified by Rayleigh with the hypothesis that this mismatch was the consequence of an imprecise knowledge of the grating period, but Strong[80] showed that the influence of the metal on the shape of the anomalies and, much more important, on their location, plays a major role. Some years later, Fano achieved the first theoretical breakthrough on Wood's anomalies[81], explaining the discrepancy between the theoretical predictions by Rayleigh and the experimental data provided by Wood. Observing the experimental data, Fano distinguished two kinds of anomalies:

- A sharp anomaly—that is, an edge of intensity—appears along the spectrum at sharply defined wavelengths governed by the grating formula using the Rayleigh conjecture.

- A diffuse anomaly extends for a wavelength interval from the first one (the edge) to the red (i.e. higher wavelengths) and "consists generally of a minimum and a maximum of intensity (one dark band and one bright band)".

The Rayleigh conjecture predicts the location of the sharp anomaly, while the anomaly observed by Wood is the diffuse anomaly. Fano explained the diffuse anomaly by "a forced resonance" related to the "leaky waves supportable by the grating", by assuming a grating consisting of lossy dielectric material and suggesting that anomalies could be associated with the excitation of a surface wave along the grating. The resonant excitation of leaky surface waves near the grating, which occurs when a suitable phase matching between the incident plane wave and the guided wave is satisfied, leads to a strong enhancement of the field near the grating surface. The theory developed by Fano explains also interference phenomena such as the sharp asymmetric profiles observed by Beutler in 1935 in the absorption of the Rydberg spectral atomic lines, revealing the universality of Fano's approach in describing the origin of asymmetric line shapes in terms of interference phenomena, regardless of the nature of the constituting waves. The Fano resonance exhibits a distinctly asymmetric shape with the following functional form[82]

$$I \propto \frac{(F\gamma + \omega - \omega_0)^2}{(\omega - \omega_0)^2 + \gamma^2} \tag{1.23}$$

where ω_0 and γ are standard parameters that denote the position and width of the resonance, respectively; F is the so-called Fano parameter, which describes the degree of asymmetry. The microscopic origin of the Fano resonance arises from the resonant destructive interference of a narrow discrete resonance with a broad spectral line or continuum. In Figure 1.18(a), we plot $I(\omega)$ calculated using Eq. (1.23), where the asymmetric lineshape of the Fano resonance can be observed (red line). At ω_0 = 1.45 the intensity reaches zero, meaning that the destructive interference between the continuum and the narrow resonance reaches its maximum. The Fano lineshape can be described also in terms of two weakly coupled harmonic oscillators with mass m_i, spring constant k_i, and damping Γ_i $(i = 1, 2)$, where one of the two oscillators is driven by a periodic force (see Figure 1.18(b)).[83] In this system there are two resonances located close to the eigenfrequencies ω_1 and ω_2.[84, 85] As shown in Figure 1.18(c) one of the resonances of the forced oscillator (blue line) demonstrates the standard enhancement of the amplitude near

its eigenfrequency $\omega_1^- = \omega_1$, and show a symmetric profile, described by a Lorentzian function and known as a Breit-Wigner resonance.[86] The second resonance at ω_1^+ is characterized by an asymmetric profile, and exhibits total suppression of the amplitude of the forced oscillator at the eigenfrequency ω_2 of the second oscillator. The amplitude of the first oscillator becomes zero as a result of destructive interference of oscillations from the external force and the second oscillator: at the resonance of the second oscillator (orange line) there are effectively two driving forces acting on the first oscillator, which are out of phase (see Figure 1.18(d)) and cancel each other.

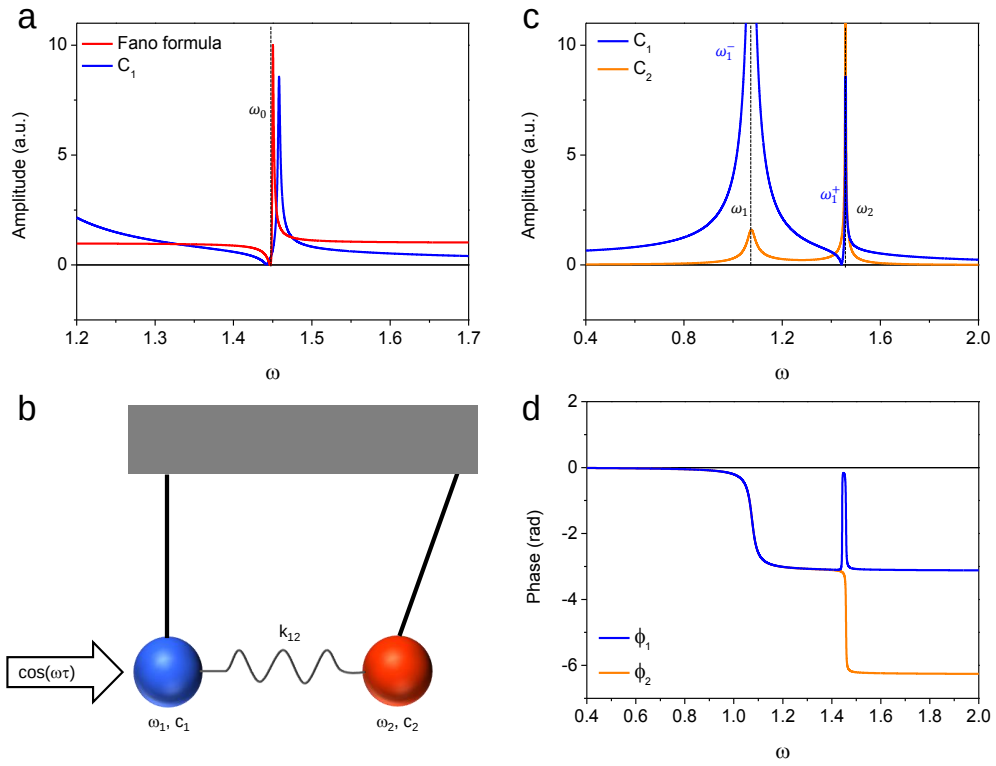

Figure 1.18: (a) Fano resonance calculated using Eq. (1.23) (red line, F = 3, ω_0 = 1.45, γ = 0.001), and using the coupled oscillators model (k_1 = 1, m_1 = 1.5, Γ_1 = 0.05, k_2 = 20, m_2 = 10, Γ_2 = 0.01). (b) Schematic view of two coupled damped oscillators with a driving force applied to one of them. (c) Resonant dependence of the amplitude of the forced oscillator c_1 (blue line), and the coupled one c_2 (orange line). The second coupled oscillator responds only with symmetric resonant profiles. (d) Phase of the forced oscillator ϕ_1 (blue line), and the coupled one ϕ_2 (orange line).

1.2 Magneto-Optical effects in metals

1.2.1 Historical introduction

The Magneto-Optical (MO) Kerr Effect (MOKE) was discovered by the Scottish physicist John Kerr in 1876 and consists in the alteration of the polarization state of light reflected from the surface of a magnetic material, as skecthed in Figure 1.19. If an external magnetic field is applied to the sample its reflectivity changes and the net effect is an ellipticization and/or rotation of the reflected polarized light.[87, 88] By impinging on the sample surface with, for instance, a p-polarized light, the reflected light acquires a small s-polarization component, whose amplitude and phase-lag ϕ with respect to the main p-component, determine the angles θ_K and ε_K that identify the elliptical polarization of the reflected field. The transmission analog to the Kerr effect is the Faraday effect (discovered by Michael Faraday in 1845), where the polarization state of a light beam is changed upon transmission through a magnetic material.

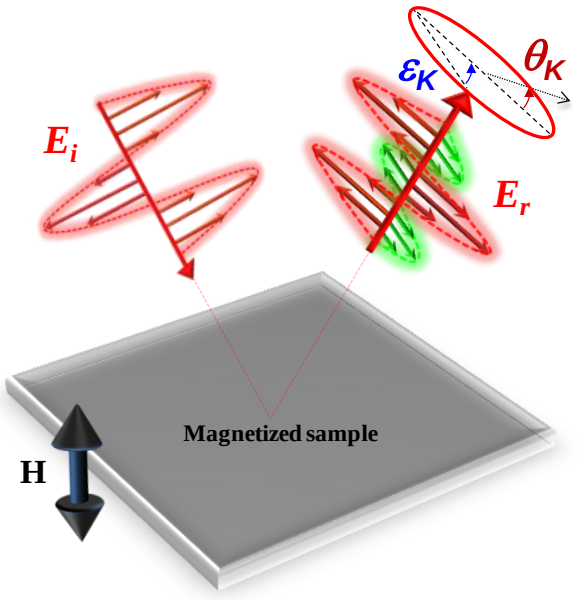

Figure 1.19: In the Kerr effect the linear polarized light becomes elliptically polarized and the polarization plane is rotated after reflection by a magnetized sample.

It was not until 1896 that similar effects were observed by Zeeman in gases. He saw the splitting of electronic states induced by the application of a magnetic field and different polarization of light emitted after absorption of photons. These effects were quickly explained in terms of classical electron theory by Lorentz. The observation was that certain spectral lines split, in the presence of a magnetic field, into two circularly polarized components when viewed along the direction of the magnetic field, the frequencies of these components being displaced to either side of the frequency of the line in the absence of the magnetic field. The displacement of the frequencies in emission implies a corresponding displacement in absorption. The theory of dispersion of Maxwell and Sellmeier had already shown the relation between the absorption spectrum of a medium and the index of refraction.[89] Thus the Zeeman splitting of the emission line into two circularly polarized components implies circular birefringence. It also implies circular dichroism, that is, a difference between the absorptions of right and left circularly polarized waves propagating in a medium along the direction of an applied magnetic field.

1.3.2 Physical origins of magneto-optical effects: classical description

In order to better understand the physics behind these phenomena, it is useful to start analyzing the explanation of the Faraday and Kerr effects in dielectric, non-magnetic media in terms of the Drude model.[90] The goal is to obtain the susceptibility tensor, from which one can determine how the electromagnetic field is modified during the interaction with such a material by the presence of an external applied magnetic field.

Let's consider a system of harmonically bound electrons in an oscillating electric field and with a static magnetic field along the *z*-axis (perpendicular to the sample plane). The equation of motion of each electron is then

$$m\ddot{\boldsymbol{r}} + b\dot{\boldsymbol{r}} + k\boldsymbol{r} = -\epsilon \boldsymbol{E}_0 e^{-i\omega t} - \epsilon\mu_0 \dot{\boldsymbol{r}} \times \boldsymbol{H} \tag{1.24}$$

where b is the damping coefficient, $\sqrt{k/m} = \omega_0$ is the natural frequency of the electron, r is the displacement of the electron from its equilibrium position, k is the elastic-force constant and μ_0 is the vacuum permeability, as we are working with non-magnetic media. The particular solution we are interested in is the steady state condition for which the displacement $\boldsymbol{r}$ has the same time dependence as the electric field, hence Eq. (1.24) becomes

$$-m\omega^2\boldsymbol{r} - i\omega b\boldsymbol{r} + k\boldsymbol{r} = -\epsilon\boldsymbol{E}_0 - i\omega\epsilon\mu_0\boldsymbol{r} \times \boldsymbol{H} \tag{1.25}$$

Defining the *z*-axis as the direction of the applied magnetic field, if N is the average number of electron per unit volume, the polarization density $\boldsymbol{P}$ of the medium is given by $\boldsymbol{P} = -N\epsilon\boldsymbol{r}$ and can be obtained from Eq. (1.25):

$$\boldsymbol{P} = \frac{N\epsilon^2}{m}\widetilde{\boldsymbol{\mathcal{M}}}^{-1}\boldsymbol{E}_0 \tag{1.26}$$

where

$$\widetilde{\boldsymbol{\mathcal{M}}} = \begin{bmatrix} \omega_0^2 - \omega^2 - i\gamma\omega & -i\omega\omega_L & 0 \\ i\omega\omega_L & \omega_0^2 - \omega^2 - i\gamma\omega & 0 \\ 0 & 0 & \omega_0^2 - \omega^2 - i\gamma\omega \end{bmatrix} \tag{1.27}$$

where $\gamma = b/m$ is the damping parameter and $\omega_L = \epsilon\mu_0 H/m$ is the cyclotron frequency known as Larmor's frequency. The susceptibility density tensor $\widetilde{\boldsymbol{\chi}}$ relates the polarization to applied electric field through the relation $\boldsymbol{P} = \varepsilon_0\widetilde{\boldsymbol{\chi}}\boldsymbol{E}_0$. Combining this last expression and Eq. (1.26) we find that

$$\tilde{\boldsymbol{\chi}} = \frac{N\epsilon}{\varepsilon_0 m}\tilde{\boldsymbol{\mathcal{M}}} = \begin{bmatrix} \chi_{11} & \chi_{12} & 0 \\ -\chi_{12} & \chi_{11} & 0 \\ 0 & 0 & \chi_{33} \end{bmatrix} \tag{1.28}$$

where

$$\chi_{11} = \frac{N\epsilon}{\varepsilon_0 m}\left[\frac{\omega_0^2 - \omega^2 - i\gamma\omega}{(\omega_0^2 - \omega^2 - i\gamma\omega)^2 - \omega^2\omega_L^2}\right] \tag{1.29a}$$

$$\chi_{12} = \frac{N\epsilon}{\varepsilon_0 m}\left[\frac{i\omega\omega_L}{(\omega_0^2 - \omega^2 - i\gamma\omega)^2 - \omega^2\omega_L^2}\right] \tag{1.29b}$$

$$\chi_{33} = \frac{N\epsilon}{\varepsilon_0 m}\left[\frac{1}{\omega_0^2 - \omega^2 - i\gamma\omega}\right] \tag{1.29c}$$

The effect of the applied magnetic field is to introduce non-diagonal antisymmetric terms in the susceptibility tensor. For zero applied field and in the case of isotropic media, the susceptibility is reduced to a diagonal tensor with all the elements equal to each other.

1.3.2.1 Faraday effect

Let's consider the propagation of an electromagnetic wave in the direction of the applied field (*z*-axis). The wave equation for $\boldsymbol{E}$ is

$$\nabla \times \nabla \times \boldsymbol{E} = -\frac{1}{c^2}\frac{\partial^2 \boldsymbol{E}}{\partial t^2} - \frac{\tilde{\boldsymbol{\chi}}}{c^2}\frac{\partial^2 \boldsymbol{E}}{\partial t^2} \tag{1.30}$$

Choosing a solution in the form $\boldsymbol{E} = \boldsymbol{E}_0 e^{i(kz-\omega t)}$, Eq. (1.30) gives

$$\left[k^2 - \frac{\omega^2}{c^2}(1+\chi_{11})\right]E_{0x} + \left(-\frac{\omega^2}{c^2}\chi_{12}\right)E_{0y} = 0 \tag{1.31a}$$

$$\left(\frac{\omega^2}{c^2}\chi_{12}\right)E_{0x} + \left[k^2 - \frac{\omega^2}{c^2}(1+\chi_{11})\right]E_{0y} = 0 \tag{1.31b}$$

$$\frac{\omega^2}{c^2}(1+\chi_{33})E_{0z} = 0 \tag{1.31c}$$

The last equation gives $E_{0z} = 0$, while the determinant of the coefficients of the first two equations must vanish for non-trivial solution, giving the condition

$$\left[k^2 - \frac{\omega^2}{c^2}(1+\chi_{11})\right]^2 + \left(\frac{\omega^2}{c^2}\chi_{12}\right)^2 = 0 \tag{1.32}$$

Solving for k, we find

$$k = \frac{\omega}{c}\sqrt{1+\chi_{11} \pm i\chi_{12}} \tag{1.33}$$

that in combination with Eqs. (1.31)(a)-(b) yields

$$E_{0y} = \pm iE_{0x} \tag{1.34}$$

The above result means that the two values of k given by Eq. (1.33) correspond to left (L) and right (R) circularly polarized (CP) light eigenmodes, respectively. The indices of refraction are, accordingly,

$$n_L = \sqrt{1 + \chi_{11} + i\chi_{12}} \approx \sqrt{1 + \frac{N\epsilon}{\varepsilon_0 m}\left[\frac{1}{\omega_0^2 - \left(\omega - \frac{\omega_L}{2}\right) - i\gamma\omega}\right]} \tag{1.35a}$$

$$n_R = \sqrt{1 + \chi_{11} - i\chi_{12}} \approx \sqrt{1 + \frac{N\epsilon}{\varepsilon_0 m}\left[\frac{1}{\omega_0^2 - \left(\omega + \frac{\omega_L}{2}\right) - i\gamma\omega}\right]} \tag{1.35b}$$

The last expressions on the right of Eqs. (1.35a) and (1.35b) are valid under the assumption $\chi_{12} \ll 1$. The effect of the applied magnetic field is to shift the dispersion curves for circularly polarized light by an amount equal to $\omega_L/2$ and proportional to $|\boldsymbol{H}|$. Let's consider a monochromatic plane wave with wavelength λ_0 which, at z = 0, is linearly polarized in the x-direction, in order to identify the effect of propagation through a magnetized medium by evaluating how much the resultant polarization rotates from the original direction (quantified by a rotation angle θ_F) and how much it becomes elliptical (quantified by the ellipticity ε_F, i. e. the angle whose tangent is given by the ratio of the axes of the resultant ellipse). This linearly polarized wave can be expressed through Jones vectors and can be resolved into left and right circularly polarized waves[90]

$$E_0\begin{bmatrix}1\\0\end{bmatrix} = \frac{1}{2}E_0\begin{bmatrix}1\\i\end{bmatrix} + \frac{1}{2}E_0\begin{bmatrix}1\\-i\end{bmatrix} \tag{1.36}$$

This means that we can analyze the propagation considering the superposition of the propagation of circularly polarized waves, which can be described using the refraction indices given by Eqs. (1.35a) and (1.35b):

$$\frac{1}{2}E_0\begin{bmatrix}1\\i\end{bmatrix}e^{i\frac{2\pi n_L}{\lambda_0}z} + \frac{1}{2}E_0\begin{bmatrix}1\\-i\end{bmatrix}e^{i\frac{2\pi n_R}{\lambda_0}z} = E_0 e^{i\psi}\begin{bmatrix}\cos(\delta)\\\sin(\delta)\end{bmatrix} \tag{1.37}$$

where

$$\psi = \frac{\pi z}{\lambda_0}(n_R + n_L) \tag{1.38a}$$

$$\delta = \frac{\pi z}{\lambda_0}(n_R - n_L) \tag{1.38b}$$

After propagating a distance l in the medium, the wave will be elliptically polarized with the major axis of the ellipse rotated by an angle

$$\theta_F = Re(\delta) = \frac{\pi z}{\lambda_0} Re(n_R - n_L) \tag{1.39}$$

and ellipticity

$$\tan(\varepsilon_F) = \tanh[Im(\delta)] = \tanh\left[\frac{\pi z}{\lambda_0} Im(n_R - n_L)\right] \tag{1.40}$$

From these equations (for a detailed derivation see Appendix B5), it can be seen that θ_F and ε_F come from a difference between the indices of refraction for left and right circularly polarized light, which are the propagation modes for a light wave traveling in the direction of the applied magnetic. Eq. (1.40) also leads to the fact that the light becomes elliptically polarized only if the indices of refraction are complex quantities, namely if the medium is absorbing. Expanding n_L and n_R for $\chi_{12} \ll 1$ and substituting them back in Eq. (1.39), θ_F becomes

$$\theta_F \approx -\frac{\pi l}{\lambda_0} Re\left(\frac{i\chi_{12}}{1 + \chi_{11}}\right) = VlH \tag{1.41}$$

where the coefficient V is the wavelength-dependent Verdet constant and it is a characteristic of the material.

1.3.2.2 Kerr effect

The analysis given above can also lead to the evaluation of the rotation and ellipticity in the case of the Kerr effect at normal incidence. The effect arises from the reflection a light wave undergoes when it impinges on a medium with susceptibility given by Eq. (1.28); such phenomenon can be described through the Fresnel coefficient r for normal reflection:

$$r = -\frac{n-1}{n+1} \tag{1.42}$$

where n is the ratio between the index of refraction of the medium the wave impinges on and the index of refraction of the medium the wave initially propagates. In this case, we take as reference a monochromatic plane wave $\boldsymbol{E}_0$ with wavelength λ_0 which is lineraly polarized in the *x*-direction and propagates in vacuum. The reflection is evaluated in terms of the superposition of Eq. (1.36), so using Eqs. (1.35a) and (1.35b) to calculate r:

$$\frac{1}{2}E_0\left\{\begin{bmatrix}1\\ i\end{bmatrix}\left(-\frac{n_L-1}{n_L+1}\right)+\begin{bmatrix}1\\ -i\end{bmatrix}\left(-\frac{n_R-1}{n_R+1}\right)\right\} \propto \begin{bmatrix}1\\ i\left(\frac{n_R-n_L}{1-n_Rn_L}\right)\end{bmatrix} = \begin{bmatrix}1\\ \theta_K + i\varepsilon_K\end{bmatrix} \tag{1.43}$$

where

$$\theta_K = -Im\left(i\frac{n_R-n_L}{1-n_Rn_L}\right) \tag{1.44a}$$

$$\varepsilon_K = Re\left(i\frac{n_R-n_L}{1-n_Rn_L}\right) \tag{1.44b}$$

The expansion used in obtaining the Eq. (1.41) implies that $n_R - n_L$ is of the order of χ_{12} if $\chi_{12} \ll 1$; under this assumption we can identify θ_K as the Kerr rotation and ε_K as the Kerr ellipticity for the case of normal incidence. Again we see that these effects are proportional to the applied magnetic field and that the plane of polarization of light is rotated only if the interaction is with an absorbing medium.

1.3.3 Microscopic description of the magneto-optical effects

The description of the MO effects has main been focused on the explanation of the unusual large effect showed by ferromagnetic materials, for which MO effects are up to five orders of magnitude more intense than in non-ferromagnetic bodies under the same external applied magnetic field. These effects are definitely connected to the ferromagnetic properties of the system, since for temperature higher than the Curie temperature they disappear along with the ferromagnetic behavior. The classical approach presented above can be extended in order to evaluate the electronic equations of motion in metallic media, for which the conduction electrons play a fundamental role. As reported in Chapter 1.1, the electrons are grouped into two sets: the bound electrons, whose equations of motion do not include a force from the magnetization $\boldsymbol{M}$, and the conduction electrons, whose equations of motion do include a force given by the presence of an effective magnetic field $\xi \boldsymbol{M}$ proportional to the magnetization.[91] This field, known as *Weiss field*, was postulated by Weiss in order to account for the existence of ferromagnetic order and it is of the correct order of magnitude to justify the observed effects. In view of these considerations, the equations of motions to be solved are, according to the notations used in Eq. (1.24)

$$m\ddot{\boldsymbol{r}}_{\boldsymbol{1}} + b_1\dot{\boldsymbol{r}}_{\boldsymbol{1}} + k\boldsymbol{r}_{\boldsymbol{1}} = -\epsilon \boldsymbol{E}_0 \tag{1.45}$$

$$m\ddot{\boldsymbol{r}}_{\boldsymbol{2}} + b_2\dot{\boldsymbol{r}}_{\boldsymbol{2}} = -\epsilon \boldsymbol{E}_0 - \epsilon\mu_0\ddot{\boldsymbol{r}}_{\boldsymbol{2}} \times \xi \boldsymbol{M} \tag{1.46}$$

for the bound electrons and for the conduction electrons, respectively. The polarization of the medium can be obtained by the averaged effect given by the two groups of electrons, in the form of $\boldsymbol{P} = -\beta N\epsilon \boldsymbol{r_1} - (1-\beta)N\epsilon \boldsymbol{r_2}$, where β is the fraction of bound electrons out of a total electron density N. This leads to an anti-symmetric susceptibility tensor, in which the off-diagonal terms are proportional to the component of the magnetization. Both groups of electrons contribute to the susceptibility tensor, but in the presence of magnetism only the contribution from the conduction electrons is affected by the presence of the effective magnetic field $\xi \boldsymbol{M}$, known also as Weiss field. After the advent of quantum mechanics, Heisenberg was able to ascribe the Weiss field to the exchange interaction among electrons, providing a description for ferromagnetic phenomena in terms of an effective field capable of aligning the individual spins. However, this field cannot be used to explain magneto-optical effects, because it is not coupled to the electron motion which determines the optical properties of a material. This problem was solved by Hulme, who introduced the concept of spin-orbit interaction, which couples the motion of an electron to its spin, providing the connection between magnetic and optical properties in a ferromagnetic material. The interaction of the electron spin $\boldsymbol{s}$ with the magnetic field the electron "sees" as it moves through the electric field $-\nabla V$ inside a medium with momentum $\boldsymbol{p}$, known also as spin-orbit coupling interaction, is expressed by a term proportional to $(\nabla V \times \boldsymbol{p}) \cdot \boldsymbol{s}$, which, to a certain extent, can be thought as an effective magnetic field acting on the motion of the electron. For non-magnetic materials, this effect is not strong, because the equal number of spin-up and spin-down electrons cancels the effect, although the spin-orbit interaction is present. For ferromagnetic materials, the effect manifests itself because of the unbalanced population of electron spins. A full derivation of these effects in ferromagnets was given by Argyres using the band theory of metals and the perturbation theory in order to evaluate the first-order effect of the spin-orbit interaction on the optical properties of ferromagnets.[92]

1.3.4 Macroscopic formalism of Kerr and Faraday effects

Assuming that the dielectric tensor $\tilde{\boldsymbol{\varepsilon}}$ is known, in absence of magnetic fields, this tensor is symmetric, namely $\varepsilon_{ij} = \varepsilon_{ji}$, but the application of a magnetic field makes this tensor asymmetric and dependent on the magnetization of the material ($\varepsilon_{ij}(M) = \varepsilon_{ji}(-M) = -\varepsilon_{ji}(M)$, also known as Onsager's principle). In a matrix form this tensor is expressed as

$$\tilde{\boldsymbol{\varepsilon}} = \begin{bmatrix} \varepsilon_{xx} & \varepsilon_{xy} & \varepsilon_{xz} \\ -\varepsilon_{xy} & \varepsilon_{yy} & -\varepsilon_{yz} \\ -\varepsilon_{xz} & \varepsilon_{yz} & \varepsilon_{zz} \end{bmatrix} \tag{1.47}$$

Let's consider the case of a cubic crystal or an isotropic medium, namely $\varepsilon_{xx} = \varepsilon_{yy} = \varepsilon_{zz} = \varepsilon$. The electric induction $\boldsymbol{D}$ can be written as

$$\boldsymbol{D} = \varepsilon(\boldsymbol{E} + iQ\boldsymbol{m} \times \boldsymbol{E}) \tag{1.48}$$

where $Q = i(\varepsilon_{ij}/\varepsilon_{ii})$ is the magneto-optical constant or Voigt parameter, a macroscopic and wavelength dependent quantity summarizing the quantum mechanical effects of the SOC and proportional to the magnitude of the magnetization, $\boldsymbol{m} = \boldsymbol{M}/M_{Sat}$, where M_{Sat} is the magnetization value at the saturation and m_x, m_y and m_z are the director cosines of $\boldsymbol{M}$. In this case the dielectric tensor takes the following form

$$\tilde{\boldsymbol{\varepsilon}} = \varepsilon \begin{bmatrix} 1 & iQm_z & iQm_y \\ -iQm_z & 1 & -iQm_x \\ -iQm_y & iQm_x & 1 \end{bmatrix} \tag{1.49}$$

As mentioned in the previous Section, the Kerr (Faraday) effect manifests as a change in the polarization of the reflected (transmitted) light. All the information related to this effect is summarized in the reflectivity (transmittivity) matrix of the system, which can be calculated starting from the knowledge of the dielectric tensor of the material considered. This matrix, that contains the Fresnel coefficients connecting the incident and reflected (transmitted) electric fields through $\boldsymbol{E}_{r(t)} = \tilde{\boldsymbol{S}}\boldsymbol{E}_i$, is defined as

$$\tilde{\boldsymbol{S}} = \begin{bmatrix} r_{pp}\,(t_{pp}\,) & r_{ps}\,(t_{ps}\,) \\ r_{sp}\,(t_{sp}\,) & r_{ss}\,(t_{ss}\,) \end{bmatrix} \tag{1.50}$$

where $r_{pp}\,(t_{pp}\,)$ and $r_{ss}\,(t_{ss})$ are the reflectivity (transmissivity) coefficients for the p- and s-component of the light, whereas $r_{ps}\,(t_{ps})$ and $r_{sp}\,(t_{sp})$ represent the polarization conversion of s-polarized light into p-polarized light, and of p-polarized light into s-polarized light, respectively. The Kerr (Faraday) rotation $\theta_{K(F)}$ and ellipticity $\varepsilon_{K(F)}$ are defined through the Fresnel coefficients as

$$\left|\theta_{K(F)}^{p(s)}\right| = Re\left(\frac{r_{sp\,(ps)}}{r_{pp\,(ss)}}\left(\frac{t_{sp\,(ps)}}{t_{pp\,(ss)}}\right)\right) \tag{1.52a}$$

$$\left|\varepsilon_{K(F)}^{p(s)}\right| = Im\left(\frac{r_{sp\,(ps)}}{r_{pp\,(ss)}}\left(\frac{t_{sp\,(ps)}}{t_{pp\,(ss)}}\right)\right) \tag{1.52b}$$

This definition is strictly effective only for linearly s- or p-polarized incident light. Since a multiplicity of sign conventions appears in literature, the above equations express only the modulus of the rotation and ellipticity, while the sign must be chosen in agreement with the convention adopted.[93] As we have already seen, the effect of the magnetization is contained in Q: if $Q = 0$, only $r_{pp}\,(t_{pp}\,)$ and $r_{ss}\,(t_{ss})$ are different from zero and they are reduced to the usual form valid for the reflection (transmission) between dielectric media. In this case, the Kerr rotation and ellipticity are zero, for both p and s-polarization of the

incoming light. When $Q \neq 0$, different MOKE configurations can be distinguished, depending on the relative direction of the magnetization to the plane of incidence (see also Figure 1.20):

- Polar MOKE (P-MOKE), where $m_z = 1$, $m_x = m_y = 0$ (magnetization parallel to the surface normal);
- Longitudinal MOKE (L-MOKE), where $m_y = 1$, $m_x = m_y = 0$ (magnetization parallel to both the surface and the plane of incidence);
- Transverse MOKE (T-MOKE), where by $m_x = 1$, $m_y = m_z = 0$ (magnetization parallel to the surface and normal to the plan of incidence).

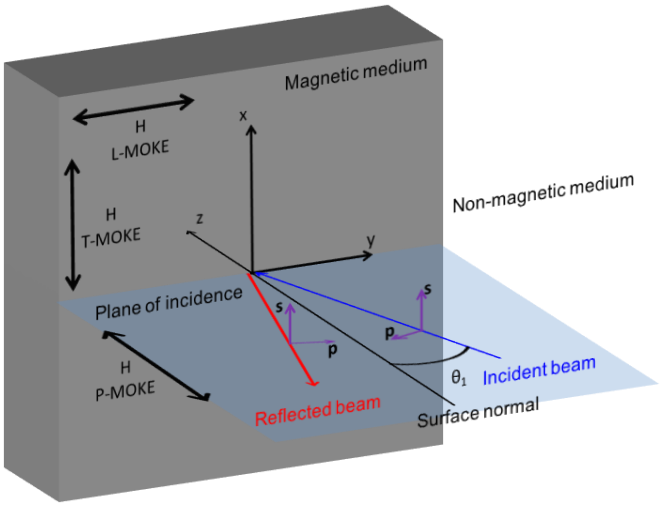

Figure 1.20: Coordinate system used in the description of the MOKE geometries.

Noteworthy, the T-MOKE does not produce Kerr rotation and ellipticity, but it only induces a change in the intensity of linearly p-polarized incident light, because r_{ss} does not depend on Q and from $m_y = m_z = 0$ follows that $r_{ps} = r_{sp} = 0$. In this Thesis we use the Polar and the Longitudinal configurations (see also Appendix A1.2 for a description of the measurement set-up used).

2. Magneto-optics of ferromagnetic nanostructures supporting localized plasmons

In this Chapter we explore the influence of the phase of localized surface plasmon resonances on the magneto-optical activity of nanostructured ferromagnetic materials. We demonstrate that ferromagnetic nanoantennas support two or more simultaneous plasmons, which are activated by an external static magnetic field. We show that these systems can be described as damped harmonic oscillators coupled by the spin-orbit interaction. We prove that the spin-orbit induced plasmons play an active role on the magneto-optical properties. By controlling the relative amplitude and phase lag between the oscillators involved we can tailor the intensity and sign of the Kerr effect over a broad spectral range. Our theoretical predictions are fully confirmed by magneto optical Kerr effect and optical extinction measurements in nanostructures of different size and shape.

2.1 Introduction

The main result presented in this Chapter is that the complex interplay between magneto-optical (MO) activity and localized surface plasmon resonances (LSPRs) in ferromagnetic nanostructures can be described in terms of a simple model based on orthogonal damped harmonic oscillators coupled by spin-orbit coupling (SOC) interaction. Our model reveals that the phase lag between these oscillators governs the MO response of the system. We first experimentally demonstrate the validity of our model in Polar MO Kerr Effect (P-MOKE) geometry. We furthermore show that the tunability of MO effects in plasmonic magnetic nanostructures supporting LSPRs can be even more amplified using the longitudinal MOKE (L-MOKE) configuration. We show how controlling the geometry of the nanostructures is a straightforward path to the tuning of MO responses. We first employ an archetypical nanostructure with geometrical anisotropy, a planar nanoellipse, to devise the general concepts necessary for achieving a broadband control of phase and amplitude of light. The key of this functionality lies in the interplay of the directly excited and the SOC induced LSPRs in the individual magnetoplasmonic nanoantenna. We finally extend this approach also to three-dimensional (3D) ferromagnetic nanoantennas, conceptualizing our theory to all common magneto-optical Kerr effect geometries.

2.2 Plasmonic phase-tuning of magneto-optical effects

At first, we investigated three samples made of Ni circular nanodisks of nominal diameters D = 70 nm, 100 nm and 160 nm. The nanodisks have the same nominal thickness t = 30 nm and were fabricated on glass substrates into large-scale short-range ordered, namely non-periodic, arrays using hole mask colloidal lithography (HMCL, see Appendix A3.2 for more details). The surface coverage or filling factor, that is the number of disks per unit area, is ~10%. The inter-particles spacing is sufficiently large to consider them as non-interacting. SEM images of these arrays are shown in the insets of

Figure2.1(a), which shows the experimental extinction spectra $(I_0 - I_t)/I_0$ of the three samples. I_0 and I_t are the intensities of the incident and transmitted light, respectively.

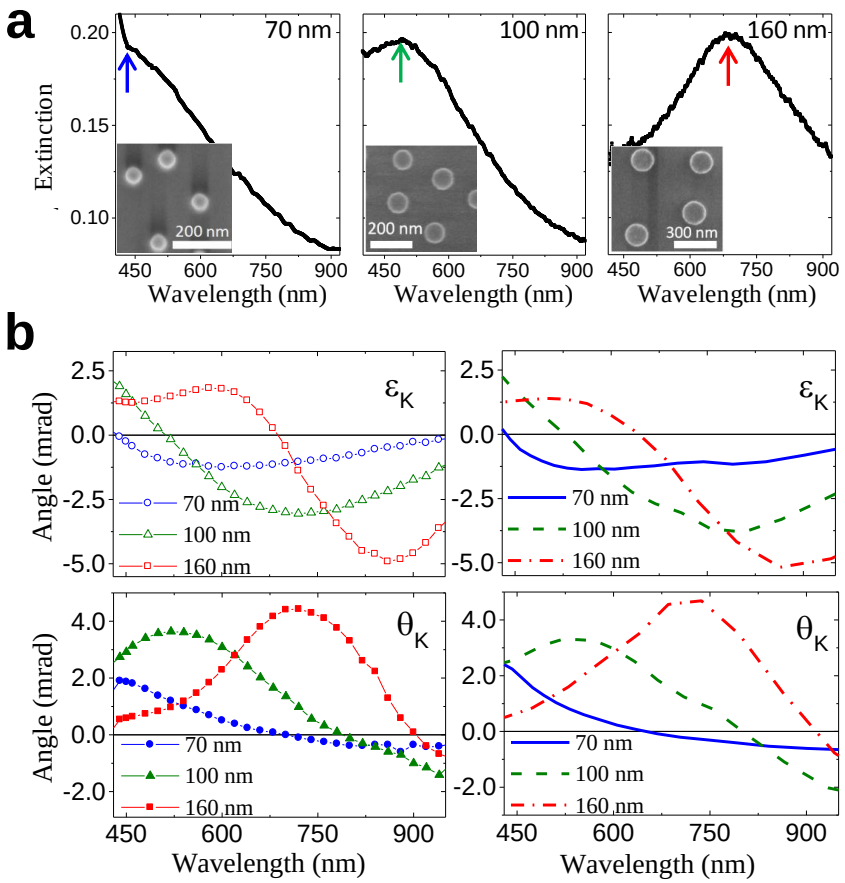

Figure 2.1: (a) Extinction spectra of the three samples. The arrows mark the excitation of a plasmonic resonance. Insets: SEM images of a portion of each sample. (b) Experimental (left panel) and calculated (right panel) P-MOKE spectra of ε_K (top panels) and θ_K (bottom panels).

The extinction spectra display the characteristic peaks due to the excitation of LSPRs at visible wavelengths, as well as the expected red-shift of the peak position with increasing the diameter of the nanodisks.[38] MOKE measurements in a Kerr spectrometer working in P-MOKE geometry (incident angle 2.5º) were measured in the wavelength range 420-950

nm. Kerr rotation (θ_K) and ellipticity (ε_K) angles were measured when the polarity of the saturating magnetic field $|H_S|$ = 8 kOe was switched along the normal of the sample plane (see Appendix A1.2 for a description of the MOKE experimental set-up used). The left column of Figure 2.1(b) shows the experimental P-MOKE spectra of the three samples. A sign reversal of ε_K can be observed in all three samples at the increasing wavelength of ~ 440 nm, ~ 510 nm, and of ~ 690 nm for D = 70, 100, and 160 nm, respectively. At a wavelength close to that corresponding to each ε_K sign reversal, a maximum of θ_K is observed. The comparison between the P-MOKE and extinction spectra clearly indicates that the features in the Kerr spectra are correlated to the excitation of LSPRs in the Ni nanodisks.

In order to precisely identify the physical mechanism through which the excitation of a LSPR acts on the P-MOKE response, we model the internal collective oscillations of conduction electrons in an isolated nanodisk as two orthogonal damped harmonic oscillators coupled by the SOC interaction, as sketched in Figure2.2. The complex solution of a single oscillator equation can be directly associated with the polarizability α_{ii} of the nanostructured object along the i-direction . Thus, the nanodisk is approximated by an oblate ellipsoid with principal axes D (in-plane) and t (out-of-plane).

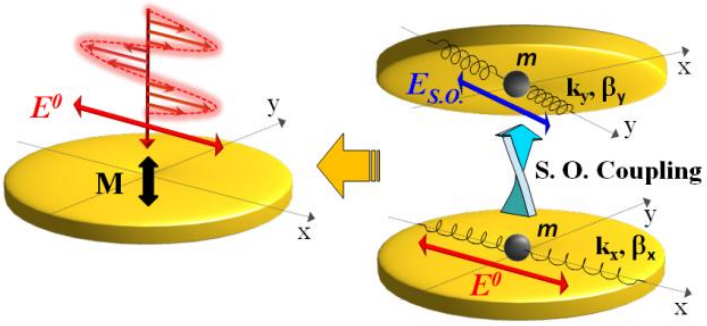

Figure 2.2: A ferromagnetic disk modeled with two orthogonal damped harmonic oscillators coupled by the SOC interaction; m represents the mass of the conduction electrons; the spring constants k_x and k_y originate from the electromagnetic restoring forces due to the displacements of the conduction electrons; β_x and β_y are the damping constants.

The optical properties of Ni are described with an anti-symmetric permittivity tensor $\tilde{\boldsymbol{\varepsilon}}$ with $\varepsilon_{xx} = \varepsilon_{yy} = \varepsilon_{zz} = \varepsilon_r$ and $\varepsilon_{xy} = -\varepsilon_{yx} = i\varepsilon_r Q$, where Q is the Voigt parameter defined in Chapter 1.2, which accounts for the effects of the SOC interaction on the dielectric properties of the constituent material. All the remaining components of the tensor are equal to zero in the case considered here (disk magnetized along the *z*-direction). The off-diagonal terms, hence the SOC interaction, couple the two transverse in plane oscillation modes: if one oscillator is excited, the other orthogonal oscillator is activated through the SOC interaction. The amplitude and phase of the oscillation of the orthogonal oscillator are governed by the interplay between the coupling strength, the stiffness of the springs, and the damping constant along *y*-direction. Referring to Figure 2.2, the complex electric field amplitude E^0 of the incident light, assumed to be a plane monochromatic wave, is driving the collective oscillation of the conduction electrons along the *x*-direction. Consequently a complex oscillating electric dipole

$$p_x = \chi_{xx} E_x^i = \varepsilon_0(\varepsilon_r - \varepsilon_m)E_x^i \tag{2.1}$$

is induced. Here, ε_m is the dielectric constant of the medium surrounding the disk, χ_{xx} is the diagonal component of the electric susceptibility tensor $\tilde{\boldsymbol{\chi}} = \varepsilon_0(\tilde{\boldsymbol{\varepsilon}}_{\boldsymbol{r}} - \tilde{\boldsymbol{I}}\varepsilon_m)$ of Ni, with $\tilde{\boldsymbol{I}}$ the identity tensor, and $E_x^i = E^0 - E_x^d$ is the internal electric field effectively acting on the conduction electrons. E_x^d is the depolarizing field (restoring force) generated by the electric dipole per unit volume p_x owing to the spatial confinement and it is opposite to E^0. We know that p_x can be expressed in terms of E^0 as

$$p_x = \varepsilon_0 \alpha_{xx} E^0 \tag{2.2}$$

where α_{xx} is the disk polarizability density along the *x*-direction. The general expression of α_{ii} is $\alpha_{ii} = [\varepsilon_m(\varepsilon_r - \varepsilon_m)]/[\varepsilon_m + N_{ii}(\varepsilon_r - \varepsilon_m)]$ (see Appendix B1 for a detailed derivation), where N_{ii} is the depolarizing factor, which accounts for the finite size and

shape of the disk and for radiative damping effects. Considering the pure material effect, viz., neglecting for the moment the spatial confinement along *y*-direction, the SOC interaction induces an oscillating dipole

$$p_y^{SOC} = \chi_{yx} E_x^i = \varepsilon_0 \varepsilon_{yx} E_x^i \tag{2.3}$$

It is convenient to describe this coupling through a second electric field $E_{SOC} = p_y^{SOC}/\chi_{xx} = p_y^{SOC}/[\varepsilon_0(\varepsilon_r - \varepsilon_m)]$ acting on the conduction electrons along the *y*-direction

$$E_{SOC} = \frac{\varepsilon_{yx}}{(\varepsilon_r - \varepsilon_m)} E_x^i \tag{2.4}$$

Introducing the restoring force along the *y*-direction due to the spatial confinement, the electric dipole generated by the damped harmonic oscillation driven by E_{SOC} is

$$p_y = \varepsilon_0 \alpha_{yy} E_{SOC} = \varepsilon_0 \frac{\varepsilon_{yx} \alpha_{yy}}{(\varepsilon_r - \varepsilon_m)} E_x^i \tag{2.5}$$

where α_{yy} is the nanodisk polarizability along the *y*-direction. The polarization of the far-field radiated in the *z*-direction by these two orthogonal oscillating electric dipoles is given by the ratio

$$\frac{p_y}{p_x} = \frac{\varepsilon_{yx} \alpha_{yy}}{(\varepsilon_r - \varepsilon_m)^2} \tag{2.6}$$

where we neglect the back effect of p_y onto p_x that would lead to terms quadratic or higher order in ε_{yx}. This approximation is fully appropriate since $\varepsilon_{yx} \ll \varepsilon_r$ in the spectral

range considered here. The fundamental consequence of Eq. (2.6), owing to the presence of *only* α_{yy} at the numerator, is that the plasmon-induced MO response reported in Figure 2.1(b) occurs, in P-MOKE configuration, when a LSPR is excited by the SOC interaction along the direction of the *transverse* harmonic oscillator. The direct excitation of a *longitudinal* LSPR by the incident light is *irrelevant* for the P-MOKE. Eq. (2.6) can be used to obtain the Kerr rotation and ellipticity for an isolated nanostructure of a general shape as $\theta_K = Re[p_y/p_x]$ and $\varepsilon_K = Im[p_y/p_x]$. For an ellipsoidal particle of given material and size, Eq. (2.6) requires calculation of the α_{ii}, viz., of the depolarizing coefficients N_{ii}. (see Appendix B1 for a detailed derivation). For a direct comparison of the theoretical predictions with the experimental P-MOKE spectra, the Maxwell-Garnett Effective Medium Approximation (MG-EMA) approach is used.[94-96] This approach models the nanodisks in the embedding medium, a mix of air and glass in our case, as a homogeneous film described by an effective permittivity tensor that contains the polarizabilities and the disks concentration, as sketched in Figure 2.3.

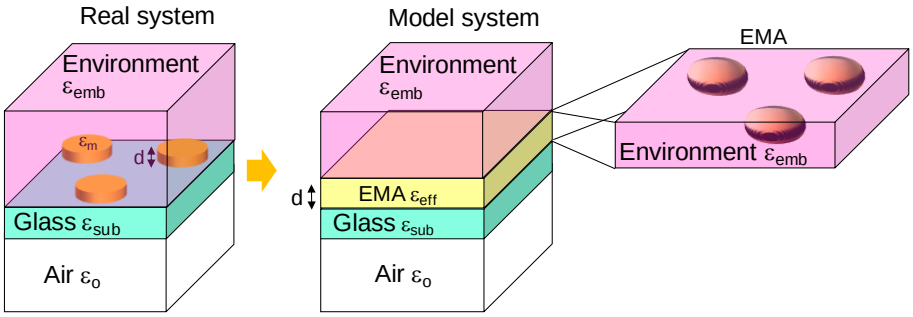

Figure 2.3: Sketch of the modeled system in the MG-EMA approximation.

We set ε_m = 1.15 and used the tabulated values of ε and Q for Ni.[97, 98] Finally, we introduce the Transfer Matrix Method (TMM)[99-101] to account for the glass substrate and evaluate the P-MOKE response. The calculated P-MOKE spectra are shown in the right panels of Figure 2.1(b), showing an outstanding agreement with measured spectra.

We now focus now on Eq. (2.6) to gain further insights of the detailed physical mechanism underlying the observed MO spectral features. An important quantity that can be retrieved from Eq. (2.6) is the phase lag between the p- and s-components of field radiated in the *z*-direction. This phase lag can be expressed as follows

$$\phi\left[\frac{p_y}{p_x}\right] = \phi[p_y] - \phi[p_x] = \phi\left[\frac{\varepsilon_{yx}}{(\varepsilon_r - \varepsilon_m)^2}\right] + \phi[\alpha_{yy}] = \phi_{SOC} + \phi_{\alpha_{yy}} \qquad (2.7)$$

Figure 2.4 shows how the two phase contributions, ϕ_{SOC} (due to the intrinsic properties of the material) and $\phi_{\alpha_{yy}}$ (related to the excitation of a LSPR along the *y*-direction), combine. Figure 2.4(a) analyzes in detail the case of a Ni disk with D = 160 nm. The plot of $Im[\alpha_{yy}]$ (dashed line) is proportional to the extinction efficiency of a single nanodisk, and displays a peak at ≈ 680 nm, in agreement with the corresponding experimental extinction spectrum shown in Figure 2.1(a). The phase spectra of the LSPR and SOC contributions are plotted as well (dotted and dash-dot lines), together with their sum (solid line), which corresponds to the phase lag $\phi[p_y/p_x]$. The plot clearly shows that the additional phase added by α_{yy} and due to the LSPR that is excited via E_{SOC}, alters dramatically $\phi[p_y/p_x]$. Due to this contribution, the condition $\phi[p_y/p_x] = 0$ results in a vanishing ε_K, which red-shifts from below ≈ 350 nm (continuous film) to ≈ 680 nm (disk, gray arrow in Figure2.4(a)), in correspondence of the peak in the extinction spectrum. Figure 2.4(b) summarizes the spectral dependence of $\phi[p_y/p_x]$ for the three Ni disks (solid lines) together with their extinction efficiencies (dashed lines). Again, the wavelength at which $\phi[p_y/p_x] = 0$ matches with good agreement the wavelength of maximum extinction and sign reversal of ε_K in the experimental spectra of Figure2.1(b) for all three the nanodisks arrays.

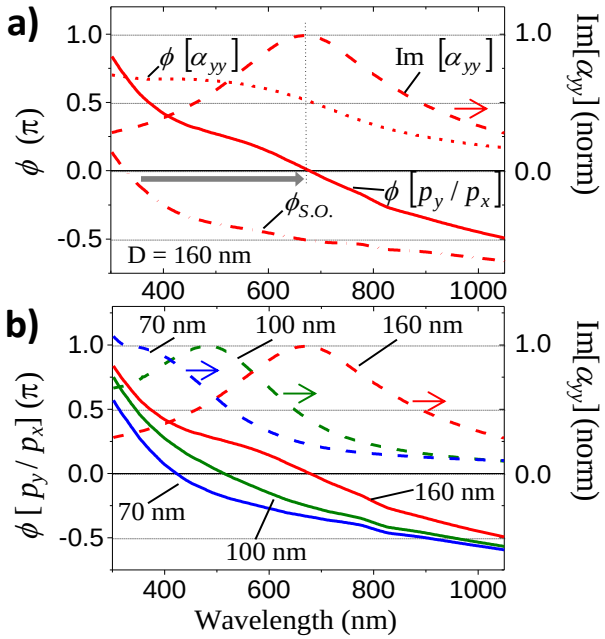

Figure 2.4: (a) Calculated spectral dependence of extinction efficiency $Im[\alpha_{yy}]$ normalized to 1 (dashed line), total phase lag $\phi[p_y/p_x]$ between p_y and p_x (solid line), and individual phase contributions due to SOC interaction (ϕ_{SOC}, dot-dashed line) and plasmonic resonance ($\phi_{\alpha_{yy}}$, short-dashed line) for a Ni nanodisk with D = 160 nm. The gray arrow shows the displacement of the point at which $\phi[p_y/p_x] = 0$ when the phase due to the plasmonic resonance is added to that due to the spin-orbit coupling. (b) Spectral dependence of extinction (dashed lines) and total phase lag $\phi[p_y/p_x]$ (solid lines) for the three disk diameters considered here.

In order to fully demonstrate that the direct excitation of a longitudinal LSPR cannot give rise to the observed P-MOKE features, a sample in which the in-plane circular symmetry is broken, namely $\alpha_{xx} \neq \alpha_{yy}$, is investigated. Such array is made of Ni nanoellipses with nominal long and short axis of 180 nm and 100 nm, respectively, and thickness t = 30 nm. A SEM image of a portion of the array is shown in the inset of Figure2.5(a), which displays the extinction spectra measured with the electric field E^0 of the incident light linearly polarized along the two in-plane symmetry axes of the system. Each spectrum shows a peak due to LSPR excitation with a maximum at 520 nm for E^0 along the *y*-direction (short axis) and at 760 nm for E^0 along the *x*-direction (long axis).

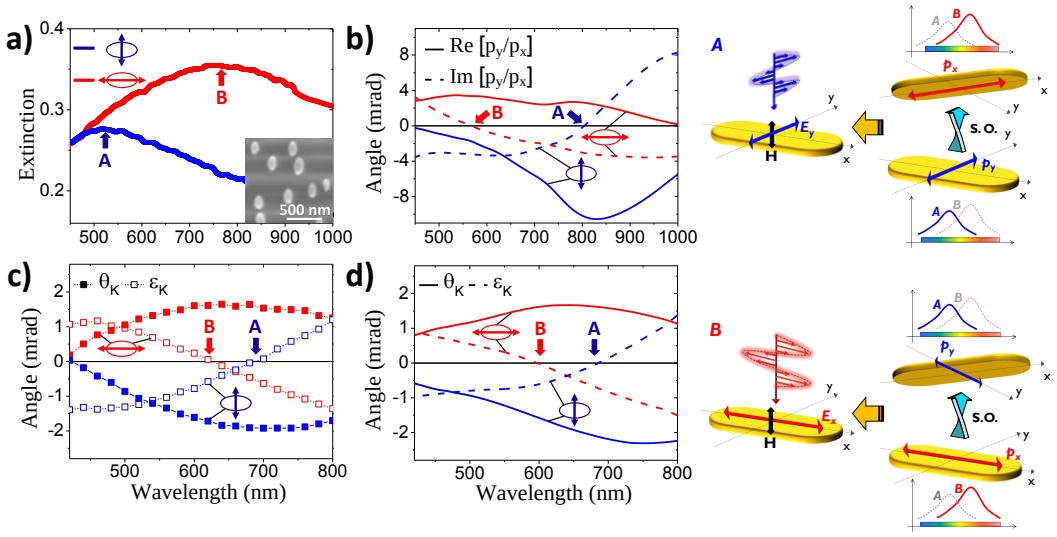

Figure 2.5: (a) Extinction spectra of the elliptical nanostructures studied for two directions of the incident electric field as sketched in the right panel. The arrows A and B mark the peaks corresponding to the excitation of a LSPR along the short- and long-axis, respectively. Inset: SEM image of a portion of the sample. (b) P-MOKE spectra calculated using Eq. (2.6). (c) Experimental P-MOKE spectra obtained for two electric field directions. (d) Calculated P-MOKE spectra using MG-EMA and TMM.

Figure2.5(b) shows θ_K and ε_K calculated using Eq. (2.6) and modeling the elliptical disk as an ellipsoid. The calculated spectra predict that, when E^0 is parallel to the *long* axis, ε_K should vanish at the wavelength close to that of the extinction peak observed when E^0 is applied along the *short* axis, and vice versa. This result, counterintuitive at first sight, matches the physical picture developed so far that the LSPR excited along the direction of the *transverse* harmonic oscillator, driven by the SOC, determines the spectral features in the P-MOKE spectra. The experimental spectra, shown in Figure 2.5(c), are compared with the prediction of Eqs. (2.6) and (2.7). It is evident from the experimental data that the zero-crossing point for ε_K, as well as the θ_K maximum, when E^0 is applied along the short axis ("A" in Figure 2.5(c)) is "red" shifted compared to the case when E^0 is applied along the long axis ("B" in Figure 2.5(c)), exactly as predicted by our model. Comparing Figure 2.5(b) and 2.5(c), one could argue that the model does not provide a good

quantitative agreement. However, the reason of the discrepancy is not related to the physics developed above, rather it is due to the reduction of the P-MOKE contrast caused by the glass substrate. In order to prove that this is indeed the case, we used the MG-EMA and TMM to include the effect of the glass substrate. Results of these calculations are shown in Figure 2.5(d), and the agreement with the experimental data is once again excellent. This proves that the apparent quantitative discrepancy between our model and the experimental data is merely a substrate effect, and directly confirms that our coupled oscillators model captures the essential physics of the MO response of ferromagnetic nanostructures supporting LSPRs.

2.3 Longitudinal Kerr effect to increase magneto-optical tunability

In this Section we study Ni nanoantennas in L-MOKE configuration. Circular nanodisks of nominal diameter D = 100 nm and 170 nm, and nanoellipses with a fixed aspect ratio (AR) of 1.4 between the long and short axis with 100/140 and 170/240 nm ratios for the short/long axis, are studied. The latter two are referred to as "100 nm" and "170 nm" nanoellipses in the discussion that follows. The thickness t of all the nanoantennas is 30 nm. A brief schematic of the LSPRs involved in this configuration when E^0 is applied along the long axis is presented in Figure 2.6. As we illuminate the particles with p-polarized light, the in-plane mode along the *x*-direction ($p_x = \varepsilon_0 \alpha_{xx} E_x^0$) is resonantly excited by the incident electromagnetic wave. At the same time there is a *z*-component of the electric field due to the angle of incidence ≠ 0° that polarizes the nanoparticle non-resonantly ($p_z = \varepsilon_0 \alpha_{zz} E_z^0$). Although the out-of-plane LSPRs of these systems occur in the UV spectral region, its excitation is sufficient to couple efficiently through the SOC interaction to the second in-plane LSPR along the *y*-direction such that

$$p_y = \varepsilon_0 \alpha_{yz} E_z = \varepsilon_0 \frac{\varepsilon_{yz}\, \alpha_{yy}\, \alpha_{zz}}{(\varepsilon_{\mathrm{r}} - \varepsilon_m)^2} E_z = \varepsilon_0 \alpha_{SO}\, \alpha_{yy}\, \alpha_{zz} E_z \tag{2.8}$$

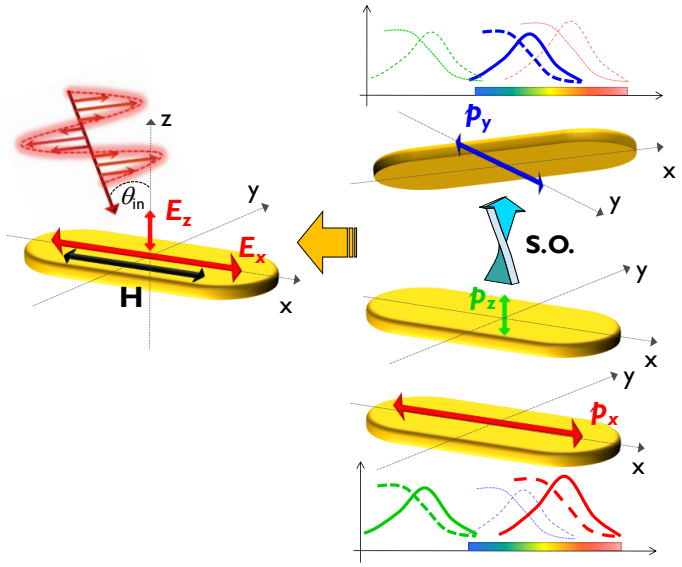

Figure 2.6: Schematic of L-MOKE when a p-polarized incident electric field E^0 is applied along the long axis of a nanoellipse (left panel). Two components of the electric field are involved: the in-plane component (red arrow in the right panel) and the out-of-plane component (green arrow in the right panel). The latter, through the SOC interaction, allows the activation the plasmonic resonance along the short axis (blue arrow in the right panel).

From a purely optical stand point we observe broad LSPRs in the VIS and NIR spectral range (Figure 2.7(a)). As expected, the spectral position of the LSPRs of nanodisks and corresponding nanoellipses (short axis equal to diameter) when E^0 is applied along the short axis fairly coincides. The LSPR related to the long axis of the nanoellipses is red-shifted as expected. In Figure 2.7(b) we show θ_K for p-polarized light incident at 25° at magnetic in plane saturation (magnetic field $|H_s|$ = 0.5 kOe) for different sample orientations and compare it with the intrinsic response of a continuous Ni film of the same thickness. A very broadband spectral tunability, both in sign and amplitude, is observed. In particular, for the "170 nm" nanoellipses at 800 nm it can been observed that θ_K displays the same amplitude but opposite sign when either the long or short axes of the elliptical nanoantennas are excited (see the raster bar in the top-right panel of Figure 2.7(b)). Conversely the reference Ni film shows zero polarization rotation at this wavelength (blue curve in the top-right panel of Figure 2.7(b)).

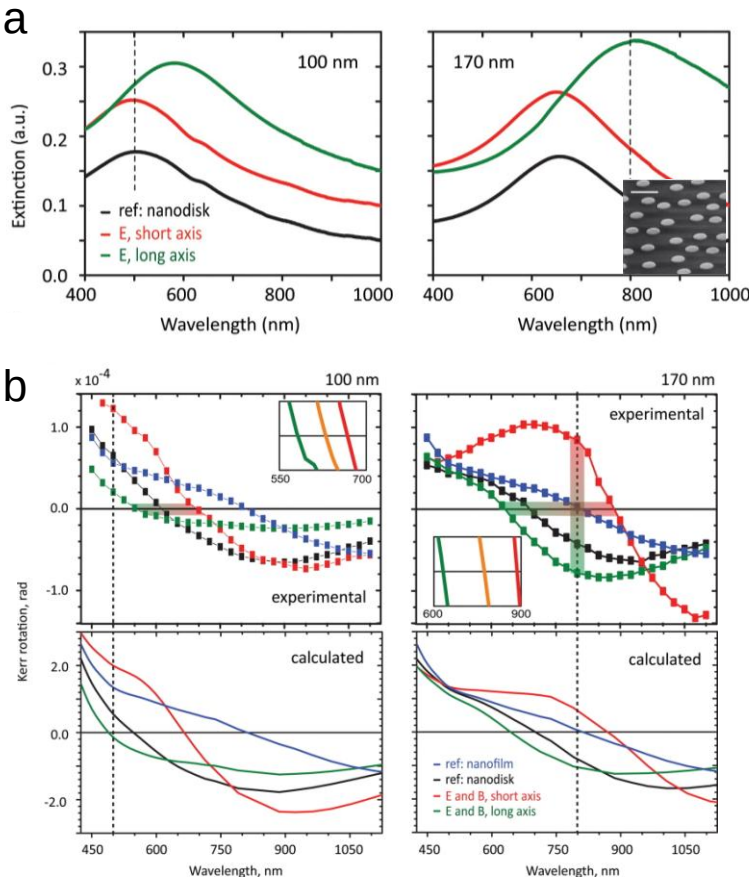

Figure 2.7: (a) Optical extinction for different nanoantenna sizes ("100 nm" and "170 nm" nanodisks and nanoellipses on left and right panels, respectively). Inset: SEM image of "170 nm" nanoelliptical antennas; scale bar 500 nm. (b) Experimental L-MOKE spectra of θ_K for the nanoantennas in p-polarization for "100 nm" (top-left panel) and "170 nm" (top-right panel) nanodisks and nanoellipses with the corresponding calculated ones (bottom panels). Insets: θ_K null-point along the symmetry axes of the elliptical antennas and for the intermediate case of 45° in-plane sample rotation (orange curve).

The θ_K null-points are shifted with respect to the reference film in such a way that $\lambda_{inv,\ long-axis} < \lambda_{inv,\ round} < \lambda_{inv,\ short-axis}$., namely close to the spectral positions of the in-plane LSPR *perpendicular* to the excitation direction (along *y*-axis), in strong analogy with what has been observed in the previous Chapter 2.2 in the P-MOKE configuration for ε_K. Again, the comparison between the measured spectra and the calculations performed using MG-EMA and TMM shows an outstanding agreement (see

bottom panels of Figure 2.7(b)). As shown in Chapter 2.2, the broadband control of sign and amplitude of the MO response originates from the off-diagonal terms of the dielectric tensor of Ni (intrinsic MO response) and the spectral dependence of the LSPRs involved. In the case analyzed here, the tunability of the L-MOKE response originates from the interplay of the two in-plane LSPRs. As these two in-plane modes are spectrally separated, giving rise to a different response both in phase and amplitude of the polarizability, they offer the possibility to obtain a very broadband tunability of θ_K beyond what is offered by the intrinsic MO properties of the material (reference Ni film case). In L-MOKE configuration and assuming p-polarized incident light, the polarization state of the reflected light can be written as follows

$$\frac{p_y}{p_x+p_z} \propto \frac{\alpha_{S0}\,\alpha_{yy}\,\alpha_{zz}\,E_z}{\alpha_{xx}\,E_x cos\gamma+\alpha_{zz}\,E_z sin\gamma} \propto \frac{\alpha_{S0}\,\alpha_{yy}\,\alpha_{zz}\,E sin\gamma}{\alpha_{xx}\,E cos^2\gamma+\alpha_{zz}\,E sin^2\gamma} \propto \frac{\alpha_{S0}\,\alpha_{yy}\,\alpha_{zz}\,sin\gamma}{\alpha_{xx}\,cos^2\gamma+\alpha_{zz}\,sin^2\gamma} \tag{2.9}$$

where γ is the angle of incidence of the impinging radiation. This expression contains the polarizabilities associated with all three modes of the nanoantenna. While the two in-plane LSPRs occur in our spectral measurement window, the out-of-plane LSPR occurs in the UV spectral region. Therefore, we can approximate the term in $\alpha_{zz} \approx 0$ in the denominator of Eq. (2.9) and rewrite it as follows

$$\frac{p_y}{p_x} \approx \frac{\alpha_{S0}\,\alpha_{yy}\,\alpha_{zz}\,sin\gamma}{\alpha_{xx}\,cos^2\gamma} \tag{2.10}$$

In terms of phases the contribution of $\phi(\alpha_{zz})$ can be set equal to 0 as well, so finally we have obtain

$$\phi\left[\frac{p_y}{p_x+p_z}\right] \approx \phi\left[\frac{p_y}{p_x}\right] = [\phi(\alpha_{yy}) - \phi(\alpha_{xx})] + \phi(\alpha_{S0}) + \phi(\alpha_{zz}) \tag{2.11}$$

From Eq. (2.11) we can see how the phase difference between the in-plane LSPRs $[\phi(\alpha_{yy}) - \phi(\alpha_{xx})]$ defines the broadband tunability observed experimentally (top panels of Figure2.7(b)). It is important noting that, although in P-MOKE (see Chapter 2.2) we observe θ_K absolute values about one order of magnitude larger than the values obtained in L-MOKE configuration, in the former case the tunability is substantially less due to the fact that the MOKE response only relies on the phase of the MO-induced LSPR and its dependence on the size (axis of the ellipse).

Finally, it is worth mentioning the s-polarized light case. Assuming that incident electric field E^0 is applied along the *y*-direction, in this case only one in-plane nanoantenna plasmonic mode (α_{yy}) can be directly excited, and θ_K is defined only by the out-of-plane MO-induced plasmonic mode (α_{zz}), which is not resonant in the spectral region explored (see Figure 2.8).

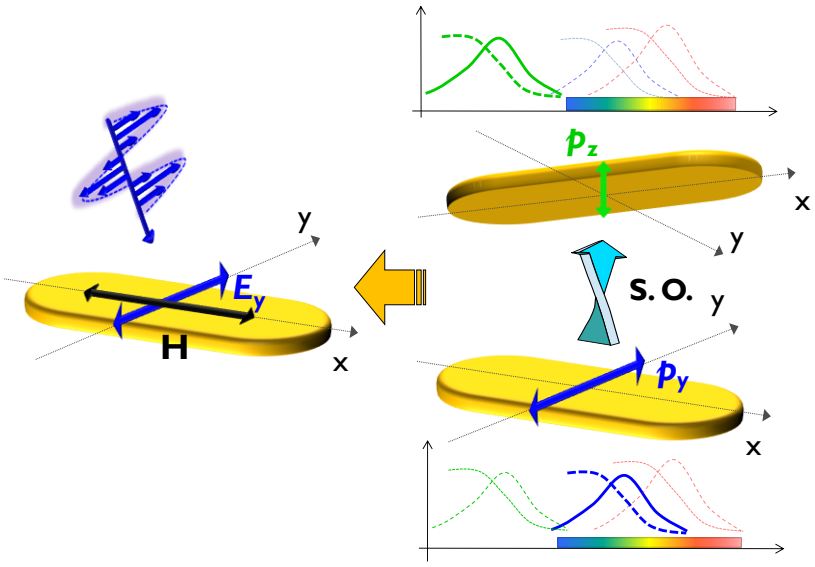

Figure 2.8: Schematic of L-MOKE in s-polarization when the incident electric field E^0 is applied along the short axis of a nanoellipse. Only one component of the electric field is involved: the in-plane component (blue arrow in right panel of the schematic). This component, through the SOC interaction, allows the activation the off-resonant plasmonic mode along the out-of-plane direction.

Similarly to the p-polarized case, we can calculate the phases governing the MO response. In this case the phase of the Kerr angle is

$$\phi\left[\frac{p_z}{p_y}\right] = \phi(\alpha_{SO}) + \phi(\alpha_{zz}) \approx \phi(\alpha_{SO}) \tag{2.12}$$

Eq (2.12) yields to a θ_K identical to that of the reference Ni film. As shown in Figure 2.9(a),(b) the experimental θ_K is very similar to that one of the single disk but different from that of a continuous Ni film. This apparent discrepancy is solved by including the substrate contribution into the modeling by using the MG-EMA and the TMM, from which we obtain the curves shown in Figure 2.19(c),(d). The glass substrate contribution blue-shifts the response of the nanoparticles with respect to the reference film, as also demonstrated in Ref [102]. In addition, the elliptical particles, when excited with s-polarized light, show a similar response as the nanodisks, almost independently on the mutual orientation respect the incident electric field and the nanoantenna axis.

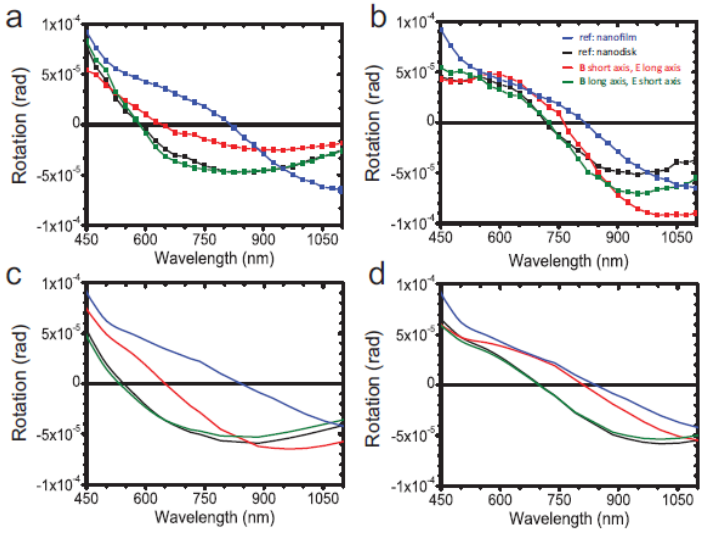

Figure 2.9: Measured L-MOKE spectra in s-polarization for "100 nm" (a) and "170 nm" (b) particles. Calculated L-MOKE spectra in s-polarization for "100 nm" (c) and "170 nm" (d) particles.

2.4 Towards magnetoplasmonics in 3D-nanoantennas

In this Section we extend the model developed above to 3D magnetoplasmonic metasurfaces and generalize the concepts presented above to all three the conventionally employed MOKE geometries, namely, L-MOKE, P-MOKE, and transverse MOKE (T-MOKE), for incident p-polarized light and γ = 25° (for the s-polarized see Appendix B2).

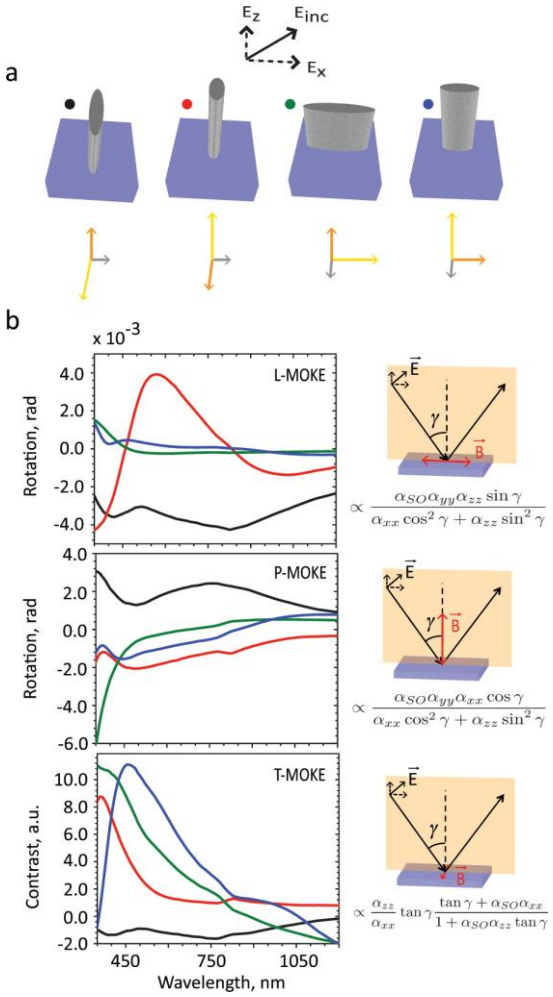

Figure 2.10: (a) Schematic set of 3D nanoantennas (top row) with highlighted resonant (yellow, orange) and off resonant (gray) modes (bottom row). (b) Calculated Kerr signals in L-MOKE (top), PMOKE (middle), and T-MOKE (bottom). Right panels feature schematics of the corresponding MOKE configurations, along with the analytical expressions for the observed polarization rotations.

For this purpose, we designed a set of 3D elliptical nanoantennas of similar dimensions (top panel of Figure 2.10(a)), with a resonant out-of-plane LSPR, one in-plane resonant LSPR, and one off-resonant in-plane LSPR. The bottom panel of Figure 2.10(a) shows the sets of the aforementioned LSPRs (resonant, orange/yellow arrows; off-resonant, gray arrow). Analytical expressions for the three MOKE configurations are featured next to the schematics of the related geometries in Figure 2.10(b) (see also Appendix B2). First, L-MOKE configuration is studied for all the configurations shown in the top panel of Figure 2.10(a). By bringing α_{zz} into play with the third dimension, and by reducing at the same time the depolarizing effect given by α_{xx}, from Eq. (2.9), which is reported also in the top-right panel of Figure 2.10(b), it is immediately clear that in the first two cases (red and black curves) we can reach θ_K values one order of magnitude larger than those plotted in Figure 2.7(b). In the other two cases (green and blue curves) θ_K values similar to those of the 2D case are observed, due to the large depolarizing contribution of α_{xx} and the almost ininfluent (off-resonant) contribution of α_{yy}. In the middle panel of Figure 2.10(b) we plot the calculated P-MOKE θ_K. Here the only way to maximize the signal is to enter at normal incidence, hence, 3D nanostructures are not the best systems to be exploited using this configuration. The striking result here is that with 3D nanoantennas L-MOKE is brought at the same level of intensity as in P-MOKE, recovering the intrisinc 1-order of magnitude smaller L-MOKE response observed in continuous films and in 2D nanoantennas (Figure 2.7(b)). Finally, in the bottom panel of Figure 2.10(b) the T-MOKE signals are shown. As mentioned in Chapter 1.3, in this configuration the MO response is detected as the ratio between the difference in intensity of the reflected light for both magnetization directions and the reflected light intensity in the non-magnetized state, namely ($\Delta I/I_0$). Although in T-MOKE we do not alter the polarization state as such, the calculated curves prove that this configuration can be a practical geometry for the modulation of the amplitude of the reflected light.

Finally, it is worth mentioning that another degree of freedom is played by the angle of incidence of the incoming light. By playing with this parameter one can reach specific conditions of "topological darkness" (Brewster condition), where the amplitude of the Kerr effect can be largely amplified until exceeding the degree of rotation. A simple

example is given in Figure 2.11, where we show Reflectivity (panel (a)) and L-MOKE (panel (b)) spectra of 3D elliptical cones with nominal in-plane dimensions of 340 nm (long-axis) and 170 nm (short-axis), and thickness t = 170 nm. As it can be seen, when the Reflectivity reaches a minimum at $\gamma \approx 50°$, θ_K exceedes 1°, and decreases when we go away from the darkness conditions. The drawback of this approach is that when the Kerr effect is maximized, the number of photons reaching the detector is really small, as the Reflectivity itself is small. The advantage is that one can exploit, in principle, the strong phase variation of the Kerr response close to the Brewester condition upon changing the refractive index of the dielectric environment, as demonstrated recently for gold plasmonic nanoantenna-based metasrufaces.[103]

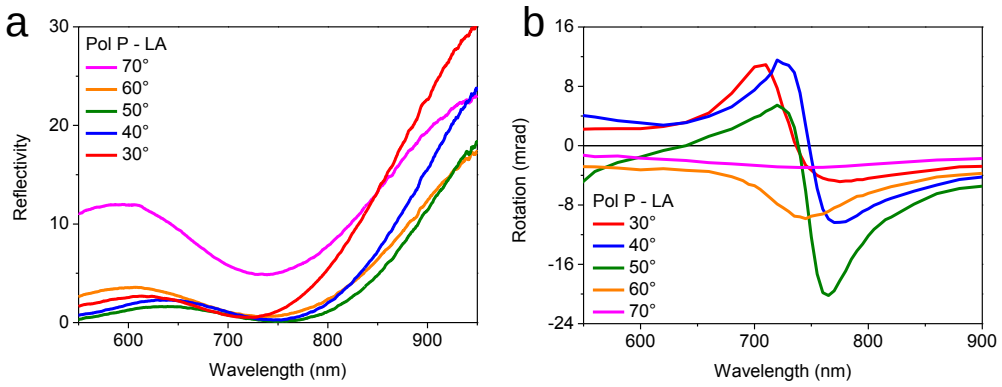

Figure 2.11: (a) Reflectivity and (b) L-MOKE spectra of 3D elliptical cones.

2.5 Conclusions

In this Chapter we have investigated the spectral MO response of circular and elliptical magnetoplasmonic nanostructures in the most common MOKE configurations. By studying the P-MOKE response of these systems and modeling the structures as two orthogonal damped harmonic oscillators coupled by SOC interaction, we were able to unveil the fundamental physics that is responsible for the characteristic features in the

MO spectra. Our results provide a new insight to the understanding of magneto-optics in magnetic plasmonic nanostructures. We furthermore experimentally verified that a highly tunable broadband control of the polarization states of the reflected light in the visible and near-infrared spectral regions is possible using the L-MOKE configuration. Finally, we derived analytical expressions with a predictive power for the Kerr response in all MOKE geometries. This generality prompts the use of the developed design principles for the emerging magnetoplasmonic metasurfaces that would deliver to an outstanding control over the polarization state of light under the application of relatively small magnetic fields (< 0.1 T) in a whole range of future active nano-optic devices. Moreover, it is worth mentioning that, although devised for pure ferromagnetic nanostructures of simple shapes, the physical picture unveiled here can apply to a broader class of nanostructures of complex shape and combining different materials, such as, e.g., multilayered and core-shell nanoparticles.

3. Polarization conversion-based sensing schemes using plasmonic and magnetoplasmonic nanostructures

Systems allowing label-free molecular detection are expected to have enormous impact on bio-chemical sciences. Many efforts are focused on materials and technologies based on exploiting surface plasmon resonances in metallic nanostructures. The suitability for single molecule sensing, arising from intrinsically nanoscopic sensing volume and the high sensitivity to the local environment, makes nanostructures supporting localized surface plasmon resonances very appealing to reach this goal. In this Chapter we propose a novel method enabling high sensitivity, which is achieved by exploiting the polarization conversion capabilities of both magnetic plasmonic nanoantennas and noble metal-based anisotropic nanostructures. We show a raw surface sensitivity (i.e., without applying any fitting procedures) up to 0.2 ng cm^{-2}. Moreover, we propose a practical implementation of our measurement set-up, and demonstrate the possibility to perform real-time single-wavelength sensing measurements in a miniaturized set-up, tracking changes in the light polarization induced by bio-molecular adsorption.

3.1 Introduction

The most prominent routes for high-sensitivity and label-free detection in a compact nano-device setting presently rely on technologies based on the explotation of localized surface plasmon resonances (LSPRs) in metallic nanostructures. The greatly enhanced electromagnetic fields at the surface of a resonant plasmonic nanostructure[6, 7] allow for probing minute changes in the surrounding environment.[103-105] Due to the evanescent nature of the near-fields, the sensing volume of plasmonic nanostructures is only marginally larger than the structures themselves, making them ideal probes for localized changes in a medium. For these reasons, the utilization of LSPRs for label-free molecular detection is under very active investigation for bio-chemical and bio-medical applications.[106-113] They feature optical interrogation schemes, small footprint, flexibility in geometry design, high sensitivity of refractometric detection, potentially down to single-molecule level, and easy integration with a wide range of fluidic systems for analyte delivery.[114, 115]

During spectroscopic LSPR-based sensing, the red shifts of the LSPR peak associated with changes of the refractive index (RI) surrounding a plasmonic system are tracked, providing a method to analyze molecular interactions at the nanoscale level.[106] In order to quantify the sensing performance of a LSPR-based sensor, the bulk RI sensitivity $S_{RI} = \Delta\lambda^*/\Delta n$ is usually considered, where $\Delta\lambda^*$ quantifies the spectral shift of the LSPR peak wavelength λ^* in the extinction spectra over the change in the environment RI Δn. For detection at the molecular level, sensitivity to *local* variation of the index of refraction is most relevant. In this case sensor performances are quantified in terms of surface sensitivity $S_{Surf} = \Delta\lambda^*/\Delta t$, where t is the thickness of an assembled thin layer of the material with RI n being sensed on top of the active surface. Since the final accuracy of the peak tracking depends both on the magnitude of the peak shift and on the resonance line-width, together with the signal-to-noise ratio (SNR) of the measurement methodology, an important performance-defining parameter is the figure-of-merit (FoM), conventionally defined by dividing either S_{RI} or S_{Surf} by the full width at half maximum (FWHM) of the resonance. However, as in the last years novel sensing schemes have

been proposed, which are not based on the direct detection of a resonance with a Breit-Wigner lineshape, it not always possible to apply this definition. For this reason, it is worth mentioning that a rivisitations of the FoM concept have been proposed recently.[103, 116] Moreober, a deep discussion on this concept and how it can be applied to our case is out of the scope of the present Chapter. However we will briefly discuss the issue in the conclusive Section. To make a fair comparison with standard LSPR-based sensors, we will focus on the sensitivity concept in combination with the SNR of the experimental readout approach utilized.

Current LSPR-based sensors show sensing performances lower or at most comparable to that of propagating surface plasmon polaritons (SPPs) resonances based sensors[117-119], which at present are the core and reference systems for label-free optical detection. On the other hand, SPPs-based sensors are not an alternative for single-molecule level detection due to the lack of local sensitivity to the index of refraction. Therefore, tremendous research efforts aimed at improving the performances of LSPR-based sensors have been conducted[111-113, 120-122]. In a typical LSPR sensing experiment, the intensity of reflected or transmitted light is spectrally analyzed and the LSPR spectral position is tracked versus time or wavelength. Alternative methodologies towards improved LSPR-based sensing have utilized complementary properties of light rather than intensity, such as optical phase[122-124], directionality[125] or ellipsometric parameters.[126-129] In the next Section we unveil a novel sensing modality that utilizes the unique optical properties of nanostructured magnetic plasmonic nanoantennas or, alternatively, of anisotropic noble metal-based plasmonic nanostructures, namely the possibility to induce a polarization conversion of the incident light. The measured change in the light polarization upon transmission/reflection from the system is then used as observable to track environmental changes due to RI variation or molecular adsorption.

3.2 Introduction to polarization conversion-based sensing

The approach we propose in this Thesis relies on systems showing natural optical activity or, in general, the capability to change the polarization of the incident light upon the application of external agents such as a magnetic field or due to their intrinsic shape anisotropy. The systems studied in this Chapter are i) magnetic plasmonic circular nanoantennas made of Ni and ii) Au nanodimers. Both systems were fabricated on glass substrates using hole mask colloidal lithography technique (HMCL, for more details see Appendix A3). In the case of Ni nanoantennas the key point is their design in order to produce exact *phase compensation* in the electric field components of the elliptically polarized transmitted/reflected light at a specific wavelength λ_ε. Under this condition, a *vanishing ellipticity* ε (ε null-point, i.e. full linear polarization) is produced at λ_ε. The determination of λ_ε provides a *phase sensitive* identification of the nanoantennas LSPR position λ^*, as shown in Chapter 2.2 when the magnetic field $\boldsymbol{H}$ applied along the normal of the surface plane. Recently, a study based on Finite Difference Time Domain (FDTD) simulations predicted that this sensing scheme can be expanded also to anisotropic non-magnetic particles.[130] Moreover, this approach is also very suitable in case of nanomaterials showing natural optical activity, like chiral metallic nanostructures, as recently demonstrated by other groups.[131]

3.2.1 Magnetoplasmonic nanoantennas

When an incident light beam hits a magnetic plasmonic nanoantenna, the conduction electrons inside the nanostructure oscillate driven by the electric field E_{inc} (see bottom panel of Figure 3.1(a)). A LSPR is induced at a specific photon wavelength λ^*, yielding a peak in the extinction spectrum $(I_0 - I_t)/I_0 = 1 - (E_t/E_{inc})^2$, displayed in the top panel of Figure 3.1(a). If the nanoantenna is magnetized perpendicularly to the surface plane, a MO activity is turned on inducing a second SOC-induced LSPR (MO-LSPR) orthogonal to that directly driven by E_{inc}. In a circular nanoantenna the MO-LSPR

resonates at the same λ^* (see bottom panel of Figure 3.1(b)). The simultaneous excitation of LSPR and MO-LSPR induces an elliptical polarization ε of the transmitted(reflected) field $E_t(E_r)$. The null condition $\varepsilon = 0$ is generated at a desired $\lambda_\varepsilon(\lambda_\varepsilon')$ simply through engineering of the size of the circular nanoantenna. In general $\lambda_\varepsilon \neq \lambda_\varepsilon' \neq \lambda^*$. Measurement of $\lambda_\varepsilon(\lambda_\varepsilon')$ performed with a photo-elastic phase modulator (PEM) analyzer based set-up provides a precise *phase sensitive* detection of the LSPR position (see Appendix A1.3 for a detailed description of the experimental set-up). We determine the ε null-point wavelength $\lambda_\varepsilon(\lambda_\varepsilon')$ by measuring the spectral dependence of the polarization ellipticity variation $\Delta\varepsilon$ of the transmitted(reflected) light, induced by applying and reversing the MO activation field $\boldsymbol{H}$. The top panels of Figure 3.1(b) and (c) display typical $\Delta\varepsilon$ (red solid line) and $1/|\Delta\varepsilon|$ (blue solid line) spectra for the transmission and reflection geometries, respectively. Plotting $1/|\Delta\varepsilon|$ makes it much easier to visualize the enormous gain in precision (limit of detection) and sensitivity of our approach.

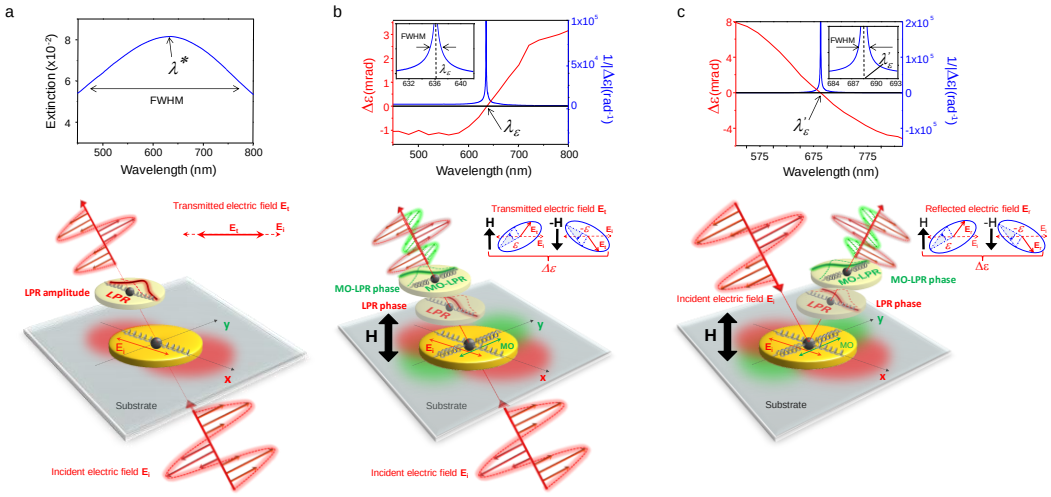

Figure 3.1: (a) Standard detection scheme based on the measurements of the LSPR peak position as function of the wavelength. Detection scheme introduced in this Thesis in transmission (b) and in reflection (c) geometry.

3.2.2 Anisotropic noble metal-based nanostructures

If linearly polarized monochromatic light is sent at normal incidence towards an optical anisotropic plasmonic nanostructures, such as elliptical antennas or dimers, and the polarization plane does not coincide with one of the principal axes of the anisotropic system, the outgoing beam will in general be elliptically polarized with a polarization axis rotated by an angle θ. The concept is presented in Figure 3.2.

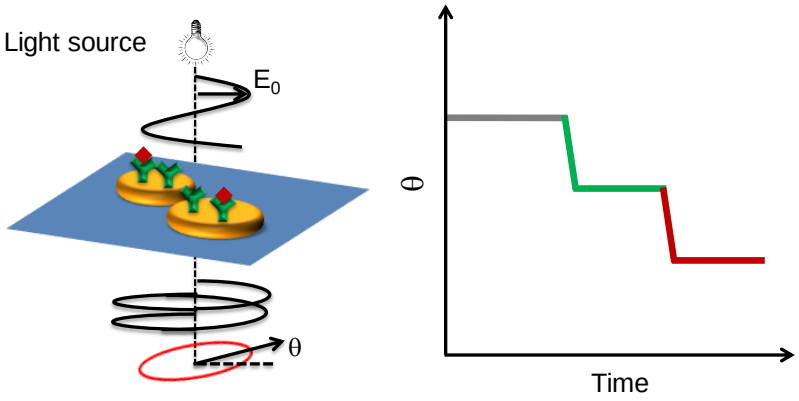

Figure 3.2: Refractometric sensing using polarization conversion. When a linearly polarized beam is sent at normal incidence towards an optical anisotropic system, the transmitted beam is elliptically polarized and the polarization axis is rotated with respect to the incident orientation. Polarization rotation changes due to local RI variations can be measured as a function of time at a chosen wavelength λ^*.

It is worth mentioning that, if Au dimers are the constituent anisotropic nanostructures, as in our case, a very high electric field enhancement in the gap region can be generated, resulting in a high sensitivity to local refractometric changes compared to isolated nanoparticles.[115] A SEM image of one of the samples fabricated using HMCL is shown in Figure 3.3(a). Each particle in the dimer has a height of ~ 40 nm (with 1 nm of Cr adhesion layer), an in-plane diameter of ~ 100 nm and a gap distance of ~15 nm, which ensures a strong near-field coupling along the dimer axis and a large field enhancement in the gap. The optical anisotropic response of the dimers was verified by measuring their

extinction spectrum at normal incidence. As expected, two in-plane resonances corresponding to dipolar plasmon oscillations along (long wavelength resonance) and perpendicular (short wavelength resonance) to the dimer axis were found, as shown in Figure 3.3(b). We also performed FDTD simulations, which confirmed the strong field enhancement in the gap region (Figure 3.3(c)).

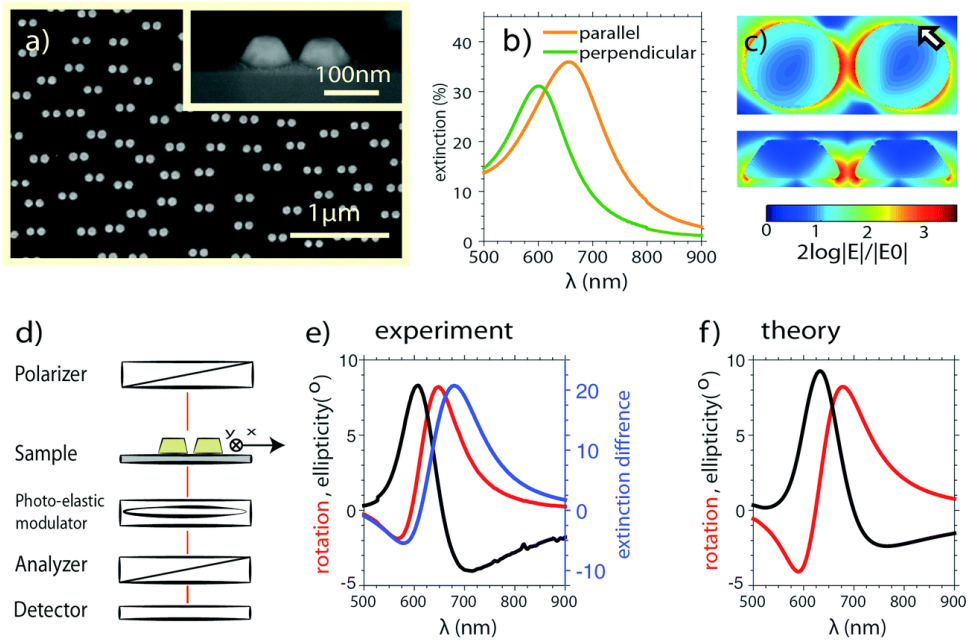

Figure 3.3: (a) SEM image of the fabricated Au dimers on glass. (b) Experimental extinction of Au dimersfor polarization parallel (orange line) and perpendicular (green line) to the dimer axis. (c) FDTD simulation of the near field intensity in a single Au dimer at λ = 650 nm. Both top view at the center of the nanoparticle (top) and side view along the dimer axis (bottom) are shown. The arrow indicates the polarization direction of the incoming light (45° from the dimer axis). (d) Sketch of the polarization sensitive setup. (e) Experimentally measured polarization rotation (red curve) and ellipticity (black curve). The rotation spectrum is essentially proportional to the difference in extinction spectra between the two principal directions (blue line). (f) Calculated rotation and ellipticity.

Figure 3.3(d) schematically illustrates the polarization sensitive measurements. The sample is illuminated with normally incident light polarized 45° with respect to the dimer axis, and the transmitted polarization state is measured with the same PEM-analyzer-

based set-up used for Ni nanoantennas. The measured θ shows a negative peak at short wavelengths, at around 590 nm, and a positive and more intense peak (as high as 8°) at around 670 nm (red curve in Figure 3.3(e)).

To understand the origin of the measured spectral features, we utilized an effective medium approximation (EMA) approach. In the limit of a thin layer of thickness d, the polarization state of the transmitted light transmitted can be approximated as

$$\theta + i\varepsilon = \frac{2\pi d\ i}{\lambda}\frac{(\epsilon_{L,x} - \epsilon_{L,y})}{1 + n_s} \tag{3.1}$$

where $\epsilon_{L,j}$ is the effective dielectric function of the metasurface along the j in-plane direction, λ is the wavelength and n_s is the RI of the substrate (for a complete analytical derivation see Appendix B4). Eq. (3.1) essentially states that $\theta(\varepsilon)$ is proportional to the anisotropy in the imaginary (real) parts of the metasurface dielectric function and to d. If the particles are small and close enough to disregard diffuse scattering, the extinction is $A_J = c/\lambda\, Im(\epsilon_{L,j})$. One thus expects θ to be proportional to the difference in extinction between the two principal directions.[132] We verified that this is effectively the case (compare red and blue lines in Figure 3.3(e)). In order to gain more quantitative informations and devise a guideline for the design of this kind of sensors, we also developed a theoretical approach based on the coupled dipoles approximation (CDA).[133-135] We calculated the effective anisotropic layer dielectric function of the system using Maxwell-Garnett EMA, with the experimental dimer surface density extracted from SEM images as filling factor. Finally, using the transfer matrix method (TMM), the rotation and the ellipticity were calculated from the complex transmission coefficients (see also Appendix B4.2). The numbers used to reproduce the experimental results are D = 80 nm, t = 40 nm. The gap is assumed to be 15 nm and the filling factor of 20% as in the real sample. The results of our calculations are shown of Figure 3.3(f) and reproduce the experimental results extremely well.

3.2.2.1 Engineering the polarization rotation tunability in plasmonic dimers

We studied the spectral dependence of θ for different dimer dimensions and verified that, by changing the nanoparticle geometries, the features observed in Figure 3.3(e) can be tuned through the VIS to NIR spectral regions. The calculations, performed using the numerical approach used before and combining CDA, EMA and TMM, indicate that the measured rotation angle of 8° can be more than doubled by increasing the spectral separation of the two in-plane resonances or by engineering the geometry of the single disk composing the dimer.

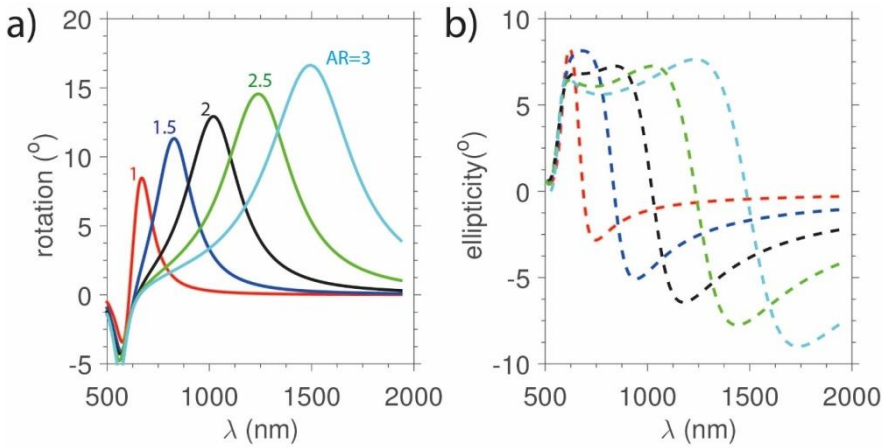

Figure 3.4: Tunability of the simulated rotation. Calculated rotation(a) and ellipticity (b) for metasurfaces of Au dimers for different in-plane aspect ratio (AR): larger rotations and shifts in the rotation peaks are observed for increasing aspect ratios due to further detuning of the in-plane resonances.

This is shown in Figure 3.4(a)-(b), where the simulated ellipticity and rotation are plotted for different particle aspect ratio (AR), keeping the other parameters (gap, filling factor, dielectric function of the medium, etc…) unvaried. AR =1 corresponds to a dimer where each disk is symmetric. In particular, in these simulations, the in-plane axis along the dimer axis and the height of the nanoparticles were kept constant to 80nm and 40nm respectively and the in-plane axis perpendicular to the dimer axis was progressively decreased.

3.3 Bulk refractometric sensing

Here we experimentally prove the concept presented in the previous Section for both magnetoplasmonic nanoantennas and plasmonic dimers. As proof of principle, in the former case we performed spectroscopic bulk sensing experiments by changing the RI of the embedding medium, passing from air (n = 1) to pure ethylene glycol (EG, n = 1.47), which was first diluted in water (50% EG 50% water, n = 1.41). In the latter case we performed real-time measurements at a single wavelength using the same approach (mixing water with EG), but in this case we used very small amount of EG (up to 10%).

3.3.1 Refractive index sensing with Ni nanoantennas

For determining S_{RI}, we measured the extinction spectra of our nanoantennas by immersing them in solutions with different RI (clean n = 1, water n = 1.33, 50% Vol. glycerol n = 1.41, and glycerol n = 1.47), as sketched in Figure 3.5(a). The observed shifts of λ^* lead to S_{RI} of 180 and 230 nm per refraction index unit (nm RIU^{-1}) (Figure 3.5(b)) for 30 nm thick Ni nanoantennas with diameters of 100 (top-left panel of Figure 3.5(c)) and 160 nm (top-right panel of Figure 3.5(c)), respectively. The $1/|\Delta\varepsilon|$ spectra of the two samples in transmission geometry (as sketched in Figure 3.1(b)) and for different values of n are shown in the lower panels of Figure 3.5(c). We observe that λ_ε undergoes the same shift asλ^*, confirming the S_{RI} values determined above. It is clear that monitoring λ_ε instead of the extinction peak λ^* enables tracking of the resonance shift with an exceptionally higher precision than in pure transmission geometry, namely tracking the spectral shift of the LSPR under RI change. It is worth mentioning that in the first part of the visible spectral range (up to 600nm), Ni nanoantennas show a higher S_{RI} as compared to Au antennas of the same dimensions, as shown in Figure 3.5(b), in spite of the higher Q-factor of gold in this spectral region.

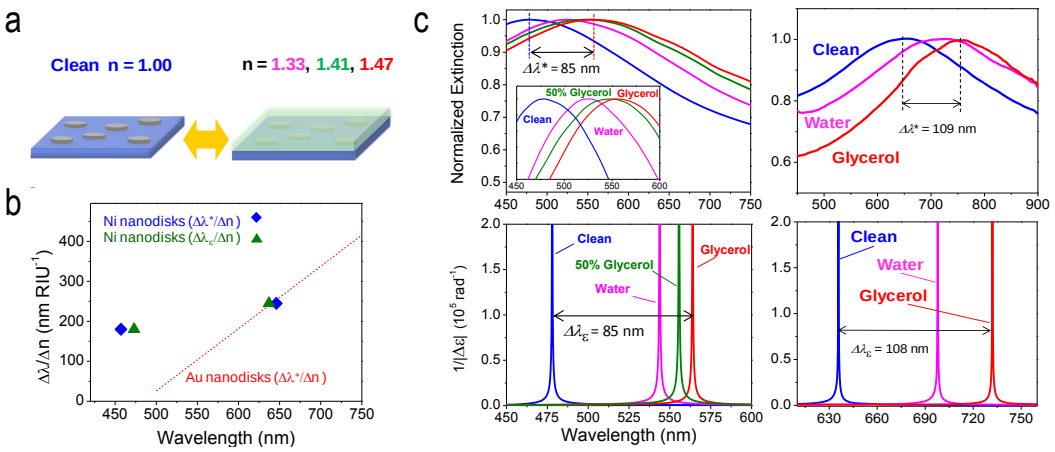

Figure 3.5: (a) Sketch of the systems studied. (b) Comparison between the bulk sensitivities of Au[136] and Ni nanoantennas. (c) Top panels show extinction spectra of Ni nanoantennas for different values of the embedding RI for nanonatennas diameter D = 100 nm (left) and 160 nm (right). The inset in the top left panel shows a zoom of the resonance peaks in the spectral region 450-600 nm. Bottom panels show $1/|\Delta\varepsilon|$ for the same values of the embedding RI as in the top panels.

3.3.2 Real time refractive index sensing with Au dimers

We now demonstrate how polarization conversion effects can be exploited using Au dimers. An increase in the RI of the surrounding medium will induce a different red shift of the long- and short-axis LSPRs shown in Figure 3.3(b). This implies that the layer dielectric anisotropy, and therefore θ (see Eq. (3.1)), will change as a function of refractive index. One can thus perform label free refractometric sensing by tracking the change of the entire θ spectrum as in the case of Ni nanoantennas, or by simply tracking the θ as a function of time at a fixed optimized wavelength λ^*. First, we performed preliminary spectroscopic RI sensing measurements by changing the RI surrounding the particles from n = 1.33 (water) to 1.34 (Figure 3.6(a)). The experiment was done by mixing water with different concentrations of EG. In Figure 3.6(b), we plot the change in rotation spectra $\Delta\theta(\lambda)$, induced by different EG concentrations compared to pure water. The maximum changes are seen to take place at around λ^* = 638 nm. We then performed

real time refractometric sensing measurements at this wavelength by continuously changing the RI and monitoring both θ and the transmission of the system, defined as the intensity I_t at the detector divided by the reference signal I_0 without nanostructures (Figure 3.6(c)).

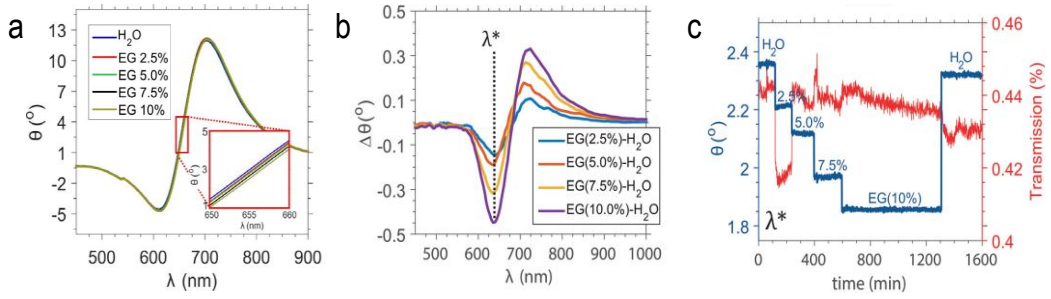

Figure 3.6: (a) Rotation spectra in different refractive index liquids. In the inset one can observe red shift in the resonances for increasing EG concentration. (b) Differential polarization rotation spectra for different concentrations of ethylene glycolin water compared to pure water. (c) Comparison between sensing performed using the polarization rotation methodology and simple transmission measurements at the optimum wavelength λ^* = 638 nm.

In the current experiment θ is measured by dividing the alternating signal at the detector induced by the PEM (see Appendix A1.2 for a detailed description of the experimental set-up) by the same I_0 signal used for the transmission measurements. While very clear and consistent changes can be observed for θ during RI changes, the transmission measurements are too noisy, although here we are not measuring the transmission at the optimal wavelength to perform standard LSPR-based sensing experiments, namely at the minimum of the transmission curve. By optimization of the SNR a base noise of 0.0006° was achieved using an integration time of 1 s. This implies that, by linear fitting of θ, changes in bulk RI as small as 10^{-6} can be detected. We also theoretically analyzed the θ sensitivity to changes in surrounding media and found that it can be improved by changing the parameters of the constituent dimer particles (Figure 3.7). In Figure 3.4 we have shown that by changing the size of the particles within a dimer, one can increase the

rotation at a fixed wavelength. However, it is not readily clear that an increase in the rotation corresponds in an increase in the rotation sensitivity during changes in the refractive index of the medium surrounding the particles. Using the numerical approach used to calculate the curves in Figure 3.4, we verified that this is exactly the case, as shown in Figure 3.7. Figure 3.7(a) shows the rotation spectra in water for the 3 different nanoparticle sizes. "Size 1" corresponds to an ellipsoid with in-plane semi-axes r_1= 40 nm and r_2= 40 nm and out-of-plane semi-axis r_3= 20 nm. "Size 2" corresponds to an ellipsoid with in-plane semi-axes of r_1= 55 nm, r_2= 27nm and out-of-plane semi-axis r_3= 27 nm. "Size 3" corresponds to an ellipsoid with in-plane semi-axes of r_1= 40 nm, r_2= 20 nm and out-of-plane semi-axis r_3= 30 nm. Afterwards, we changed the dielectric function of the medium surrounding the particles from 1.33 to 1.35 and calculated the changes in rotation as a function of wavelength, verifying that a larger increase in the rotation variation $\Delta\theta = \theta_{1.33} - \theta_{1.35}$ per refractive index unit can effectively be realized (see Figure 3.7(b)), namely the rotation sensitivity increases by augmenting the rotation itself.

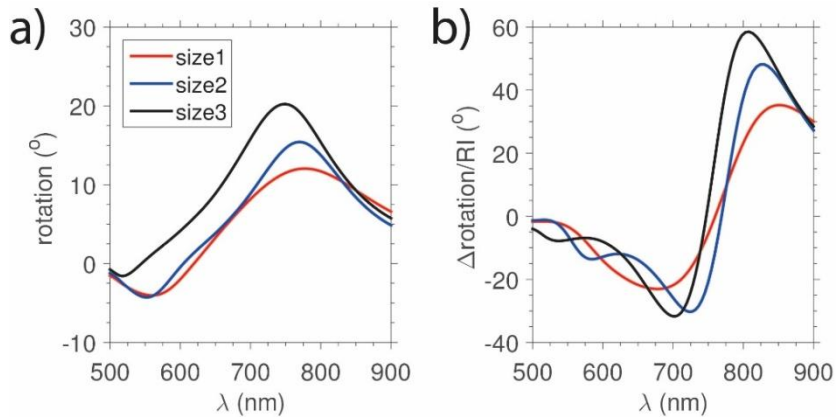

Figure 3.7: (a) Calculated θ for nanoparticles of different sizes in water. (b) Calculated $\Delta\theta$ per refractive index unit.

3.4 Molecular-level detection experiments

Applications to molecular detection rely on high sensitivity to the local variation of the index of refraction n. A reliable and precise assessment of the detection performance is an experimental challenge, as control of Δn on the molecular level is needed. A suitable method of choice is the controlled deposition of extremely thin and removable films using molecular layer deposition (MLD), an organic variant of atomic layer deposition.[137,138]

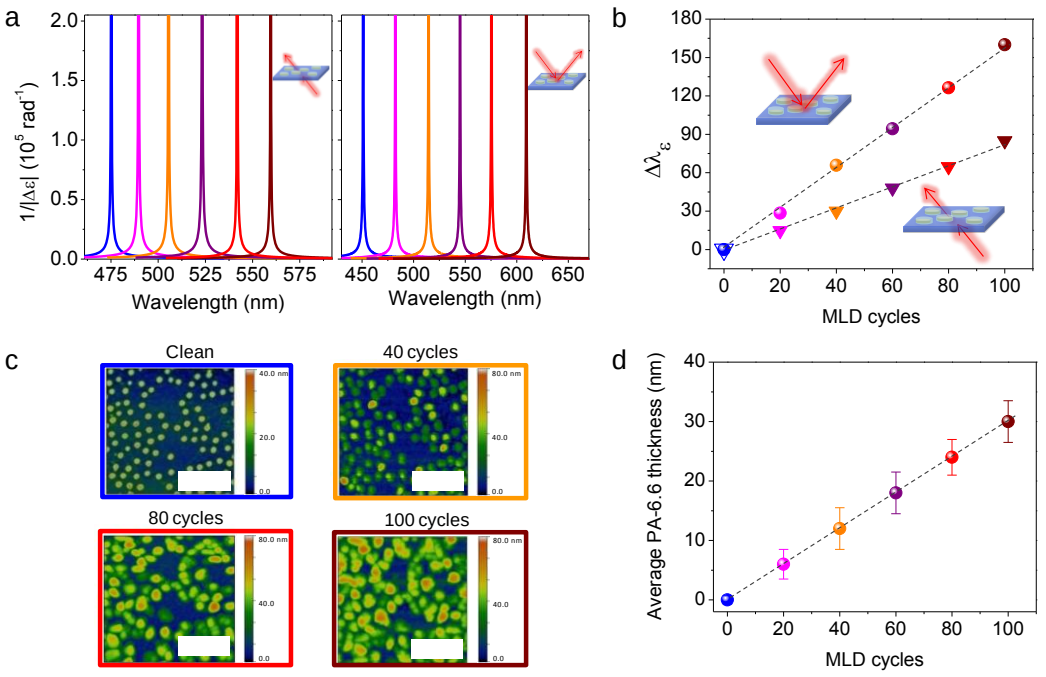

Figure 3.8: (a) $1/|\Delta\varepsilon|$ spectra in transmission (left panel) and reflection (right panel) geometry as a function of MLD cycles for Ni nanonatennas with D = 100 nm and t = 30 nm. (b) λ_ε as a function of the MLD cycles. (c) AFM images taken from the same sample region (total area imaged 2.7 x 2.7 μm^2) after different numbers of MLD cycles. The colors of the frames are referred to the corresponding colored polarimetry (b) and thickness (d) data points (black dashed lines are guide for eyes). Scale bars 1 μm. (d) PA-6.6 average thickness as function of the MLD cycles. The error bars indicate the standard deviation from the average thicknesses measured analyzing the AFM images.

The cyclic and self-terminating growth mechanisms of this method allow molecular scale control of the polymer film growth and surface-dependent nucleation characteristics can be used for area selective growth through matching of substrate and precursor chemistries. More importantly, MLD deposits polymer films from vaporized pure molecular fragments avoiding potentially negative impact of solvents. In the case of Ni nanonatennas-based sensors we used MLD of polyamide 6.6 (PA-6.6) with n=1.51.[138] This polymer was chosen for convenience as its MLD process is well established and, more importantly, being a polyamide, it is representative for a large variety of polymers, peptides, and proteins. Nominally the process has a growth rate of ~0.8 nm/cycle.[139] In a first experiment, PA-6.6 was deposited 20 cycles at a time (for a detailed description of the process see Appendix A2.2). The film thickness was measured by AFM. The corresponding change of the local RI was monitored by tracking λ_ε. Since the surface was modified only locally, we conducted polarization measurements also in reflection geometry as an alternative way to track λ_ε (see Figure 3.1(c)). The experimental spectra and the resulting shift of λ_ε are shown in Figure 3.8(a)-(b). AFM images and their quantitative analysis show that PA-6.6 nucleated selectively on the Ni nanodisks and linearly grew up to ~100 cycles (Figure 3.8(c)). In both the configurations, a linear dependence of λ_ε versus the number of MLD cycles is observed. The shift of λ_ε saturates for a number of MLD cycles equal to 120, corresponding to a PA-6.6 thickness of ~35 nm, as shown in Figure 3.9(a) for the transmission geometry case. Such PA-6.6 thickness is very close to the spatial extension of the electromagnetic near-field spatial extension (~35 nm) of a Ni nanoantenna (see top panel of Figure 3.9(b)). Combining the two plots in Figures 3.8(b) and 3.8(d), we find S_{Surf} values of ~3 and ~5.3 in transmission and reflection geometry, respectively.It is worth noting that a comparison between bulk RI sensitivity experiments conducted in both transmission and reflection geometry shows similar bulk refractive index sensitivity S_{RI}. On the other hand, local refractive index experiments as those shown in Figures 3.8, show the remarkable boosting by a factor 1.7 in the surface sensitivity $S_{Surf} = \Delta\lambda_\varepsilon/\Delta t$ of reflection experiments as compared to transmission ones.

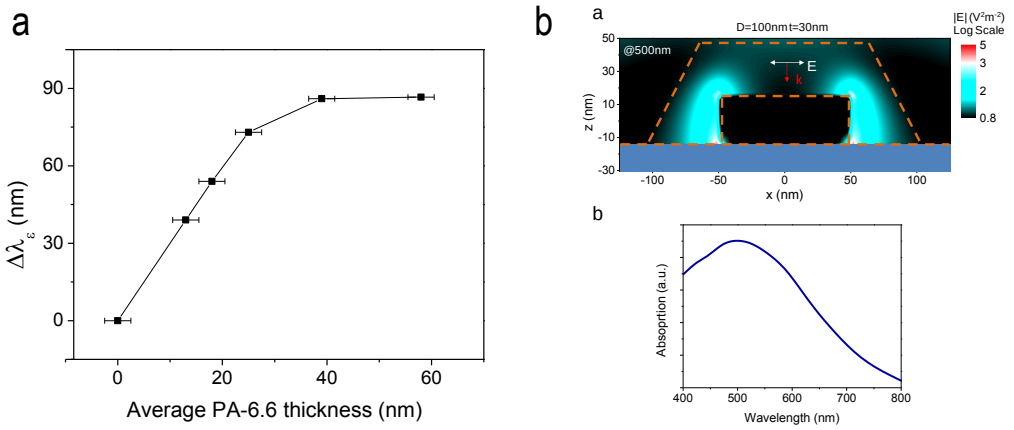

Figure 3.9: (a) $\Delta\lambda_\varepsilon$ in transmission geometry for Ni nanodisks with D = 100 nm and t = 30 nm as a function of the PA-6.6 average thickness. (b) Top panel: simulated near field amplitude $|E|^2$ of a Ni nanodisk on glass with diameter D = 100 nm and t = 30 nm. The orange dashed-line marks the near-field spatial distribution. The light blue bar under the disk is the substrate. Bottom panel: corresponding calculated absorption cross section.

This remarkable enhancement of the S_{Surf} in reflection geometry, confirmed also by calculations (see Figure 3.10), is consequence of a larger shift of λ_ε caused by the additional phase contribution of *uncovered* substrate reflectivity. In order to prove this, we performed calculations using the EMA and TMM methods. The upper panel of Figure 3.10 shows the bilayer system we have used to simulate the bulk sensitivity experiments, both in transmission and in reflection geometry, which show almost the same sensitivity. The case of local sensitivity experiments is shown in the bottom panel. In the latter case, the nanoantennas are modeled as core-shell ellipsoids, with the shell of variable thickness t with n = 1.5. The calculations yield a boosting factor of 1.65 which is in excellent agreement with the value of 1.7 found experimentally. Such boosting effect in S_{Surf} makes the reflection geometry more appealing for local sensitivity applications also because the detection can be done with the light probe coming from the substrate side, as shown in the schematic in Figure 3.11, where we show a simple practical implementation of our detection scheme. The shift of λ_ε caused by variations of the local refractive index can be precisely determined without the need of recording a full spectrum $\Delta\varepsilon$. Using only

two light wavelengths, one before and one after the zero-crossing of ε (violet and green vertical lines in the plot), which can be provided by two light emitting diodes (LEDs, as depicted in the schematic of the setup), the light intensity of the two LEDs or the photodetectors gain is adjusted to compensate the signal ($\Delta[\Delta\varepsilon] = 0$) for the clean sample.

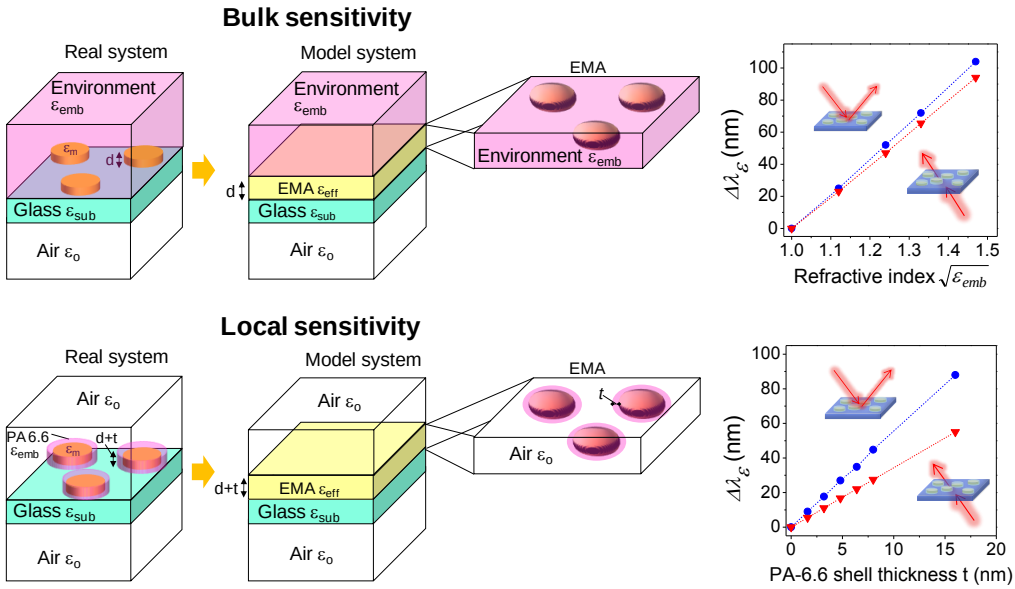

Figure 3.10: Left panels: system used to simulate the bulk (top) and surface (bottom) sensitivity experiments. Right panels: calculated S_{RI} (top) and S_{Surf} (bottom) in reflection (blue curves) and in transmission (red curves).

As the zero-crossing wavelength λ_ε shifts upon nylon deposition, this causes $\Delta[\Delta\varepsilon]$ to become positive and proportional to the PA-6.6 thickness, as shown in Figure 3.11(c). The plot shows that given the typical error bars in the measurement of $\Delta\varepsilon$, sub-nm variations of PA-6.6 thickness are easily detectable in this simple way. It is worth mentioning that this configuration does not change the sensitivity of the sensor as it does not matter from which side of the substrate the light is shone.

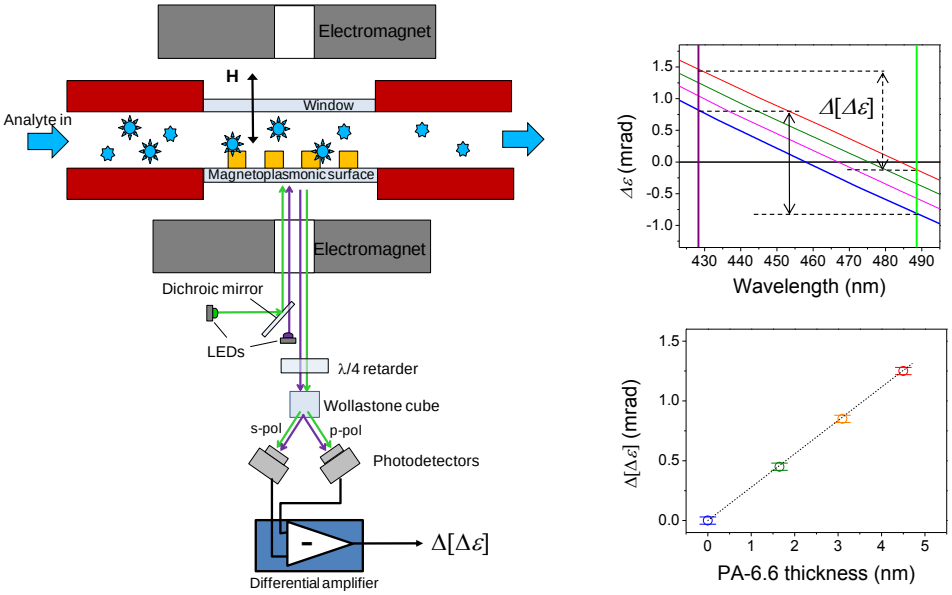

Figure 3.11: (a) Schematic of the setup for practical RI sensing applications. (b) $\Delta\varepsilon$ spectra of the clean sample and after a few cycles of PA-6.6 MLD (2, 4, and 6 cycles). (c) $\Delta[\Delta\varepsilon]$ vs. PA-6.6 thickness.

In order to demonstrate that very small quantities of material can be detected, PA-6.6 deposition, polarization ellipticity measurements and AFM characterization were performed sequentially for the very first cycles of MLD. Figure 3.12 shows that already after 2 MLD cycles an average increase in t of ~1.6 nm is determined by AFM. Based on our very conservative error bar estimate in the measurement of $\Delta\varepsilon$, we can detect λ_ε with ~0.5 nm precision without the application of any fitting procedure (*raw limit* of detection). Surface sensitivities of ~3.1 (transmission) and ~5.4 (reflection) are found, in excellent agreement with the results presented in Figure 3.8. Given the S_{Surf} values ~3 and ~5.3 of our approach (transmission and reflection geometry, respectively), detection of sub-nanometer thick PA-6.6 coverage, viz., a discontinuous monolayer (ML) of PA-6.6 on individual cylindrical Ni nanoantennas is achievable. A ML of PA-6.6 is ~8.5Å thick,[139] the precision above corresponds to a thickness of a virtual continuous layer of PA-6.6 of ~1.7 Å and ~1.0 Å for the two measurement geometries.

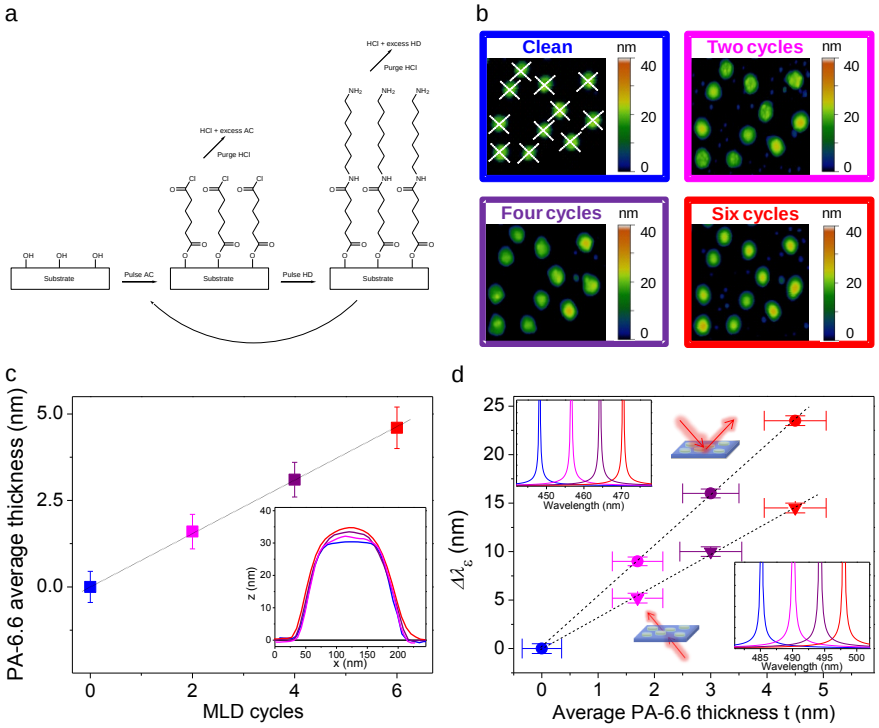

Figure 3.12: (a) Schematic of one cycle of the MLD process for PA-6.6. (b) AFM images taken from the same sample region (total area imaged 1.2 x1.2 μm^2) before and after PA-6.6 MLD. The colors of the frames are referred to the corresponding colored thickness (c) and polarimetry (d) data points. (c) PA-6.6 average thickness as function of the MLD cycles after AFM topography image analysis. The error bars indicate the standard deviation from the average thicknesses shown in the inset, where are shown the line profiles of all the disks included in the images in (b). The line profiles are taken along two orthogonal directions, which are shown as white dashed lines only in the AFM image of the clean sample in (b). (d) Plot of the inverse of transmitted and reflected light ellipticity λ_ε as a function of MLD cycles (black dashed lines are guide for eyes). The horizontal error bars indicate the standard deviation from the average thicknesses shown in the inset in (c). The vertical error bars indicate the experimental error in the measurements. The insets show the corresponding $1/|\Delta\varepsilon|$ spectra for the two measurement geometries (reflection – top-left inset, and transmission – bottom-right inset).

In the case of transmission geometry, this translates to a coverage of less than 0.2 ML, namely a ML covering less than 20% of the nanoantenna exposed surface. The minimum detectable coverage reduces to 0.1 ML in reflection geometry. Such sub-ML coverage

values are equivalent to PA-6.6 volumes of ~1200 and 800 nm^3, i.e. a remarkable mass sensitivity of ~1.2 ag and 0.8 ag per disk corresponding to about 3300 and 2200 molecules of PA-6.6 per disk (density of amorphous PA-6.6 is 1.05 g/cm^3 and its molecular weight is 226 g/mol). Such minimum detectable coverage is based on extrapolation and assumes that the electric near field is uniformly distributed in the vicinity of the Ni nanoantenna surface exposed to the environment, i.e., S_{Surf} is not, or weakly, space-dependent. This condition is fulfilled to a good extent for our nanodisks with a diameter of 100 nm as we verified by the simulations of the near field produced by the excitation of a LSPR performed using FDTD method (see Figure 3.9(b)). A raw limit of detection of a few zg (zepto-grams, 10^{-21}g) per nanoantenna can be achieved considering the sub-micro-radiant resolution of advanced polarimetry tools. These sensing performances could be further improved by applying the same strategies as employed for noble metal-based nanostructures, such as lifting of the nanostructures from the substrate and exploiting resonant coupling between LSPRs to modes with narrow FWHM.

So far, the limit of detection of our approach was derived based on the SNR of the measurements, without any mathematical fit of the data, and compared with those of similar raw estimates of sensitivity based on extinction measurement. This comparison demonstrates the radically improved S_{Surf} enabled by our approach with respect to plasmon based sensors. Higher sensitivity and limit of detection values are reported in literature for plasmon based sensors, which are achieved by application of fitting procedures.[140, 141] We mention here that the application of fitting procedures to our data confirms the higher sensitivity of our approach as shown in the Figure 3.13, where we perform a linear fit of $\Delta\varepsilon$ in transmission geometry of the clean sample with D = 100 nm in the vicinity of ε null-point. Based on this experimental data set (λ step of 0.2 nm) the standard deviation σ for λ_ε is 1.0×10^{-4} nm. The inset in Figure 3.13 shows the variation of σ for six $\Delta\varepsilon$ measurements of the clean sample taken in sequence before the MLD experiment.

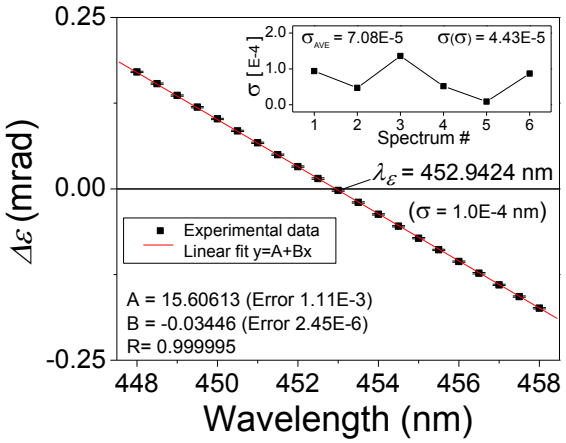

Figure 3.13: Sensitivity estimation through fitting procedure. Linear fit of $\Delta\varepsilon$ in transmission geometry of the clean sample with D = 100 nm in the vicinity of ε null-point. The inset shows the variation of σ for six $\Delta\varepsilon$ measurements of the clean sample taken in sequence before the MLD experiment.

We obtain an average standard deviation σ_{Ave} = 7.1x10^{-5} nm in the determination of λ_ε which is about 7 times smaller than that of 5.0x10^{-4} nm reported in Ref. [140] and about 3 times smaller than that reported in Ref. [141] (in the latter case the standard deviation of the peak position is 1.8-2.0x10^{-4} nm from *Figure 3(b)* in that work). The standard deviation of these sequences of measurements, $\sigma(\sigma)$ in the inset, also referred to as short-term noise level figure, in our case resulted in 4.4x10^{-5} nm to be smaller than the value of 9.9x10^{-5} nm quoted in Ref. [141]. This analysis demonstrates that even after a mathematical fit of the data, the higher sensitivity of our approach in comparison to the best values reported so far in literature, is confirmed. Indeed, a mass sensitivity in the sub-zg per nanoantenna, down to a few yg (yocto-grams, 10^{-24}g) per nanoantenna, can be achieved through the application of fitting procedures opening a pathway to mass sensitivity corresponding to ~10 molecules of PA-6.6 per disk (or, equivalently, of any material having n~1.5 and a density of ~1 gcm^{-3}, which is the case of many polymers and bio-molecules). It is worth mentioning here that a bio-molecule is normally a macromolecule made by 10s, 100s, and even 1000s of the "polymeric monomers" detected in this experiment. So, for most macromolecules of interest in biology our

technique is already capable to detect single molecules without applying any fitting procedure. Thus, magnetoplasmonic nanoantennas can be used also in nanoplasmonic biosensing (for instance detection of cancer biomarkers in serum). Ni surfaces are covered by an ultrathin layer of oxidized Ni. Such surfaces can be functionalized with either silanes or even better with Histidin tags (His6)[142] on par with Au surface functionalization with thiolate chemistry, thus informing our selected Ni as the material for our nanoantennas. As an alternative, one could even deposit a thin layer of Au (few nm), and use conventional thiolate chemistry. An alternative solution is to focus on pure Au nanostructures showing an optical anisotropy, as the dimers introduced in Chapter 3.2. As shown in Figure 3.14(a), we verify that the technique proposed so far can be used for tracking protein adsorption using this kind of non-magnetic nanostructures, which induce a polarization conversion of the incident light purely through their anisotropic shape.

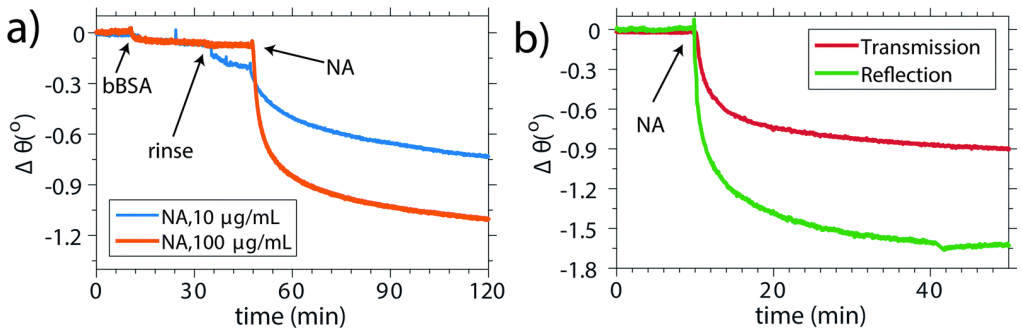

Figure 3.14: (a) Real time molecular sensing using polarization rotation analysis for two different NA concentrations. (b) Real time NA adsorption monitoring using the microscope setups and for an illumination area of ~100 × 100 µm^2 performed in transmission and reflection.

Biotylinated bovine serum albumin (bBSA), with a concentration of 100 µg mL^{-1} and diluted in a phosphate buffer solution (~0.01 M), was first adsorbed on the metasurface and, after rinsing, neutravidin (NA, molecular weight ~60 kDa), which couples to biotin, was injected in the same flow cell. Real-time measurements were performed with different NA concentrations and the induced changes in θ during adsorption were

tracked. We observe a saturated change in rotation of ~1°, which is around 1000 times larger than the base line noise using a 1 s integration time. The saturated signal corresponds to a monolayer of NA on the dimers, or about 400 NA molecules per dimer and 150 ng cm^{-2} total surface area (assuming ~55% surface coverage obtained through random sequential adsorption).[143-145] The base-line noise then gives a detection limit of 0.2 ng cm^{-2}, corresponding to ~0.05 ag or 0.5 NA molecules per dimer. Finally, rather than trying to further optimize the system for ultimate performance, we preferred to focus on a more practical aspect, namely the miniaturization and practical implementation of the set-up. This is a key aspect of multiplexed sensing, for example based on multi-channel microfluidics. A 100× long working distance air objective was placed before the sample and, using an aperture, a reduced area of the order 100 x 100 μm^2 could be selected. The rotation induced by NA adsorption (a concentration of 100 μg mL^{-1} was used) could then be tracked both in transmission and reflection (see Figure 3.14(b), red and green lines, respectively), which means that the technique can be easily implemented using both upright and inverted microscopes. Interestingly, θ in reflection is approximately twice that in transmission, as observed also in Ni nanoantennas in MLD experiments. In this case, the signal is inversely proportional to the overall light intensity I_{DC}. As glass was used as a substrate, the isotropic background in reflection is smaller than the one measured in transmission, which explains the observed different signal amplitudes.

For the system and the technique presented here it could be possible to define a FoM, which would essentially be an estimate of the "detectability" of the peak shifts for bulk changes of the RI of the medium. However, to analyze the performance of the system for biosensing, one should also consider the spatial confinement of the field. For example, while SPP-based sensors exhibit much larger FoM for bulk RI sensing compared to LSPR-based ones, the two methodologies yield similar resonance shifts upon molecular adsorption. For this reason, we rather consider the change in the observable and compare it to the baseline noise (i.e., the limit of detection). In the case of magnetoplasmonic nanoantennas, our approach is characterized by a virtually unlimited value of the FoM since $1/|\Delta\varepsilon|$ is diverging at the resonant wavelength λ_ε Practically,

however, we can estimate a FWHM by accounting for experimental errors. Although polarization parameters can be determined with sub-micro-radiant resolution (down to 10 nrad), here we assume an experimental resolution of 5 micro-radians in the determination of $\Delta\varepsilon$, which is easily achievable without the utilization of advanced tools and/or fitting procedures, and consequently truncate the $1/|\Delta\varepsilon|$ spectra at 2×10^5 rad^{-1} (see the insets in the top panel of Figure 3.1(b),(c)). We obtain a FWHM ranging from 1.5 to 1.8 nm for the resonance of the $1/|\Delta\varepsilon|$ spectra of nanoantennas with D = 100 nm and 160 nm, respectively. Taking the average FWHM of ~1.7 nm means a FoM of more than 100 RIU^{-1} and approaching 150 RIU^{-1} for Ni nanoantennas with diameters of 100 and 160 nm, respectively. Such large FoM values greatly exceed even those for SPP-based sensors in the same spectral range, which are often considered as theoretical limit references.[111] More recently similar values for SPPs-based magnetoplasmonic sensors were also predicted theoretically by Caballero et al.[146]

3.5 Conclusions

In conclusion, we have demonstrated that a polarization conversion-based sensing scheme is a very suitable alternative to conventional spectroscopic RI sensing methods. Magnetoplasmonic nanostructures or anisotropic metasurfaces were used as a transducer of molecular adsorption through detection of light polarization states. Moreover, our approach requires simple and scalable nanostructuring processes and offers a remarkably improved sensitivity performance. We demonstrated that the methodology can be adapted to reflection and transmission microscopy geometries, which indicates that the method is compatible with microfluidics. The reported sensitivity can most likely be much further improved by precise optimization of the nanostructures design and further development of measurement and analysis methodologies. Finally, in addition to bio-sensing, there are also many other potential applications that do not require surface functionalization and would enormously benefit from our approach like: chemical sensing of toxic materials, explosives, and ultra-precise thickness monitoring applications.

4. Anisotropic nanoantenna-based magnetoplasmonic crystals

In this Chapter we introduce a novel concept of magnetoplasmonic crystal based on the excitation of Fano lattice surface modes in periodically arranged nickel nanoantennas that show anisotropic in-plane plasmonic responses.The excitation of lattice surface modes in this kind of system is governed by the polarizability of the single antenna and the relative position between dipolar in-plane localized resonances in the individual building blocks and the diffraction edges induced by the periodicity of the crystal lattice. We show that the magnetic field-induced Fano lattice surface modes leads to highly tunable and amplified magneto-optical effects in either narrow or large regions of the visible and near-infrared spectrum. We demonstrate a significant strengthening of magneto-optical effects due to the coherent excitation of radiative far-field interactions between the nickel particles as compared to a continuous film or metasurfaces made of randomly distributed nanoantennas.

4.1 Introduction

Magnetic nanoantennas display larger non-radiative losses yielding to higher damping compared to conventional metals used in plasmonics, which results in broader and less intense localized surface plasmon resonances (LSPRs).[147-149], To overcome the problem, various strategies have been applied so far, such as the creation of complex hybrid noble-metal/ferromagnetic structures or by inducing a strong coupling between broad localized modes in ferromagnetic antennas with narrow excitations such as surface plasmon polaritons in noble metal-based thin films.[13, 31, 150-154] Likewise, systems based on ordered arrays of metallic antennas, called plasmonic crystals (PCs), were shown to produce an exceptional sharpening of plasmonic resonant features.The presence of a periodic lattice structure gives rise to a collective resonant diffractive coupling between the far-fields scattered by the nanoantennas at particular wavelengths dictated by the geometry and periodicity of the PC, leading to the excitation of a particular kind of plasmonic Fano resonances, also known as lattice surface modes (LSMs) or surface lattice resonances.[82, 155-163] In this framework magneto-optical (MO) properties of periodic arrangements of magnetic plasmonic antennas are starting to attract considerable attention. In particular, periodically arranged circular ferromagnetic nanoantennas have been studied very recently, showing that LSMs with Fano lineshapes can be induced also in ordered arrays of high damped nanoantennas to overcome the aforementioned limitation of the high losses and obtain narrow and intense optical and MO responses.[164,]Whilst the effects of lattice geometries and nanoantennas size and shape on the excitation of LSMs in noble-metal based PCs has been studied extensively[82, 155-163], their effects on the MO properties of PCs made of pure ferromagnetic elements are still unexplored. In this Chapter we generalize and broaden the implementation of PC concept to the magnetoplasmonics framework to design a new kind of magnetoplasmonic crystal (MPC). Such a MPC is based on the excitation of LSMs in ordered arrays made of ferromagnetic elliptical nanoantennas, leading to an enhanced and highly tunable magneto-optical activity (MOA), achieved via proper engineering of the shape and size of the individual antennas and of the periodicity of the lattice.

4.2 Lattice surface modes in magnetic nanoantenna-based plasmonic crystals

We first analyze the key mechanism that governs the dependence of LSMs on the size of the individual building blocks of the MPC, whilst the period of the lattice, assumed to be square, is fixed. In the sketch shown in the top-left panel of Figure 4.1(a) the electric field E_{inc} of the incident radiation propagating perpendicular to the the crystal plane is assumed to oscillate along one of the principal direction of a MPC, labeled with *x* and *y*. We initially consider a MPC made of magnetic plasmonic nanoantennas with in-plane aspect ratio (AR) equal to 1, namely circular disk shaped antennas. As discussed in Chapter 1.1.5, LSMs arise from the onset of in-plane diffractive coupling between the fields scattered by the individual antennas, according to the criterion developed by Rayleigh.[79] In the spectral region of interest, the strongest diffractive interaction occurs in the in-plane direction perpendicular to E_{inc}, at a wavelength $\lambda_R = a \cdot n$ ($< 1,0 >$ diffraction modes), where a is the array pitch the perpendicular direction, n is the refractive index of the surrounding medium and λ_R corresponds to the photon energy at which the wavelength of the radiation scattered by the individual antenna is commensurate with the periodicity of the array and is related to the incipent appearance of the first order diffracted radiation in the free space. Depending on the relative position between the LSPR of the single disk and λ_R, the diffractive coupling between the radiation fields produces Fano LSMs with different lineshapes.[134] This is clearly shown in the calculated Q_{ext} spectra plotted in the right-panel of Figure 4.1(a), where we vary the diameter D of circular Ni disks, arranged in a periodic fashion (a = 500 nm along both *x*- and *y*-direction), from 100 to 200 nm and embedded in a medium with n = 1.5. The thickness of the disks is 30 nm. Calculations were performed using the Coupled Dipole Approximation (CDA) method (see Appendix B3 for a detailed derivation), which is known to give an excellent description of the optical response of this kind of systems and it is based on the assumption that the individual antennas behave as a point-dipole.[134] We observe a different lineshape depending on the position of the LSPR of the isolated disk (red curve in each frame) with respect to λ_R (solid green line in each frame). Given the symmetry of the MPC considered here, it is clear that Q_{ext} does not change when the

array is illuminated by either *x*- or *y*-polarized radiation impinging perpendicularly on the array plane. If now the circular nanoantennas are replaced by elliptical shaped ones, the C_4 or 90° rotational symmetry of the MPC is broken resulting in two different, spectrally separated LSPRs for *x*- and *y*-polarized incident radiation.

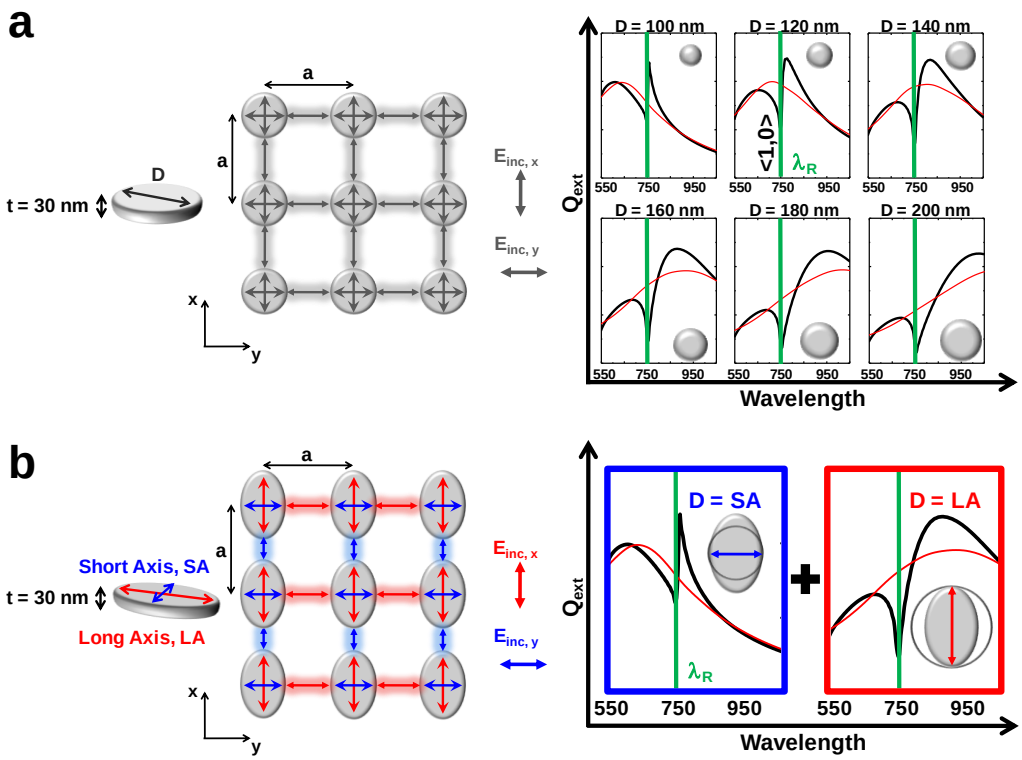

Figure 4.1: (a) Left panel: schematic of a MPC made of 30 nm thick Ni nanodisks with pitch a = 500 nm. Right panel: calculated Q_{ext} spectra for disk diameters varying from 100 nm to 200 nm (black curves). The red curves indicate the LSPR of an isolated nanodisk. (b) Left panel: schematic of the system studied in this Chapter. The single 30 nm thick Ni nanoantenna displays two different optical responses along the two in-plane principal *x*- and *y*-axis, aligned with the nanodisk long-axis (180 nm) and short-axis (100 nm), respectively. (b) Right panel: Q_{ext} spectra of the MPC sketched in the left panel (black curves). The red curves indicate the LSPR of the isolated nanoantenna. The vertical green solid lines indicate the spectral position of the Rayleigh's anomaly λ_R.

As a result, two LSMs with different Fano lineshapes are excited depending on the relative orientation of the elliptical Ni nanoantennas with respect to the polarization of the incident light, as sketched in the left panel of Figure 4.1(b). More importantly, in the case of ferromagnetic nanoantennas, the intrinsic MOA activated by the application of a magnetic field perpendicular to the crystal plane leads to the *simultaneous* and coherent excitation of two in-plane orthogonal LSPRs, as shown in Chapter 2.2. Therefore, the resonant diffractive coupling of these two antenna modes induced by the periodicity of the lattice, leads to the simultaneous excitation of two perpendicular LSMs with different Fano resonant lineshapes that can be precisely tailored through the design of the individual building blocks of the MPC. We consider that the nanoantennas have an edge-to-edge distance large enough (> 100 nm) that we can neglect near- and mid-field (NF and MF, respectively) interactions in the visible (VIS) and near-infrared (NIR) spectral region. This is indeed the case, as shown in Figure 4.2, where we plot the calculated extinction efficiency Q_{ext} of a MPC made of Ni circular disks with diameter D = 160 nm, thickness t = 30 nm and array pitch a = 500 nm embedded in a medium with n = 1.5. It's clear that Q_{ext} is dominated by the far-field (FF) interactions (green dashed line). In fact, if we switch off FF interactions, leaving only NF and MF interactions (cyan solid line), the lineshape of Q_{ext} is the same as that of an individual isolated Ni nanoantenna (red solid line), a part for a slight variation close to the diffraction edge at λ_R = 750 nm.

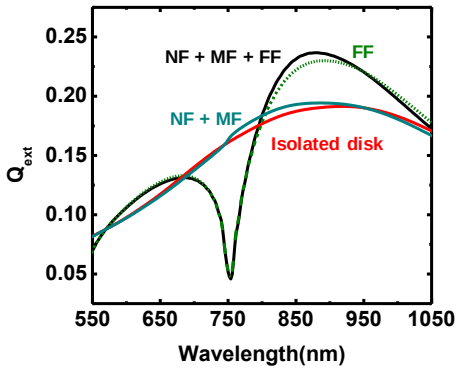

Figure 4.2: Q_{ext} spectra of a MPC made of Ni nanoantennas, with diameter D = 160 nm and thickness t = 30 nm, taking into account all the fields interactions (black solid line), only FF interactions (green dashed line), only NF and MF interactions (solid cyan line) and Q_{ext} of an isolated Ni nanonatenna (red solid line).

In order to verify the physical picture presented above, we first designed and fabricated a sample made of randomly distributed elliptical Ni antennas on a glass substrate using e-beam lithography (EBL, see Appendix A3.3 for detailed information about the fabrication process). The elliptical nanoantennas have an in-plane aspect ratio AR ≈ 2.5, to display LSPRs at markedly different wavelengths when the two axes are selectively excited by linearly polarized radiation impinging perpendicular to the sample surface. The nominal in-plane dimensions of the nanoantennas are 100 nm for the short-axis (SA) and 250 nm for the long-axis (LA). The thickness of the nanoantennas is 30 nm. The system is then embedded in a homogenous medium with n = 1.5 after immersion in refractive index matching oil. A SEM image of a portion of the fabricated system is shown in the top panel of Figure 4.3(a). The Q_{ext} spectra of this sample for the two polarizations of the incident radiation are shown in the central panel of Figure 4.3(b) (dashed blue line and dashed red line for light polarized along SA- and LA-direction, respectively). The spectra show broad peaks at 580 nm (polarization along SA) and 1050 nm (polarization along LA) arising from the excitation of the corresponding LSPR. We then fabricated a MPC in which elliptical nanoantennas with the same dimensions of the randomly distributed ones, are arranged on a square array with a lattice constant a = 400 nm. We assume the LA and SA lying along the *x*- and *y*-direction, respectively, as sketched in the left panel of Figure 4.1(b). As for the random sample, the MPC is fabricated on a glass substrate and embedded in refractive index matching oil with n = 1.5. A SEM image of a portion of the fabricated system is shown in the bottom panel of Figure 4.3(a).The experimental Q_{ext} spectra of the MPC are plotted in the central panel of Figure 4.3(b) with solid lines using the same color code as for the random sample. When the electric field of the incident radiation oscillates along the LA-direction (red curve), we observe the excitation of a LSM with a Fano lineshape featuring a dip around λ_R = 600 nm, followed by a broad peak in the near-infrared region close to 1000 nm. In contrast, when the incident electric field is parallel to the SA-direction (blue curve), a LSM is excited with a dip around the same λ_R but now followed by a narrow and sharp peak in the visible spectral region close to 650 nm. This behavior was expected based on the discussion of Figure 4.1 (see right panel of Figure 4.1(b)).

Using the CDA, the Q_{ext} for the two polarizations of the incident field can be expressed as follows

$$Q_{ext-LA} \propto Im\{\tilde{\alpha}_{xx}^{eff}\} = Im\left\{\frac{1}{\frac{1}{\tilde{\alpha}_{xx}} - \varepsilon_0 \tilde{S}_{xx}^{FF}(\hat{y}_i)}\right\} \tag{4.1}$$

$$Q_{ext-SA} \propto Im\{\tilde{\alpha}_{yy}^{eff}\} = Im\left\{\frac{1}{\frac{1}{\tilde{\alpha}_{yy}} - \varepsilon_0 \tilde{S}_{yy}^{FF}(\hat{x}_i)}\right\} \tag{4.2}$$

where $\tilde{\alpha}_{xx}(\tilde{\alpha}_{yy})$ is the polarizability tensor element of the individual dipole along the LA (SA) direction, $\tilde{\varepsilon}_M$ is the permittivity tensor element of the embedding medium, and $\tilde{S}_{xx}^{FF}(\hat{y})$ ($\tilde{S}_{yy}^{FF}(\hat{x})$) is the dipolar FF interaction factor for LA-(SA-) direction. The latter depends only on the geometrical parameters of the lattice, specifically on the *y*- (or *x*-) direction, indicated by the $\hat{y}$ (or $\hat{x}$) unit vector dependence. From the experiments and the above formulas it is straightforward to see that when E_{inc} is oscillating along the LA-direction Q_{ext} is determined by a LSM involving the antennas LA-LSPR and the far-field diffractive interaction along the SA-direction. Likewise, Q_{ext} for E_{inc} along the SA-direction is determined by a LSM resulting from the SA-LSPR excited in each antenna and the far-field diffractive interaction along the LA-direction. In the present case of square lattices $\tilde{S}_{xx}^{FF}(\hat{y}) = \tilde{S}_{yy}^{FF}(\hat{x})$, so λ_R does not change and the lineshape of the LSMs is determined by the relative position between the LSPR peak and the wavelength of the first order diffraction edge $< 1,0 >$. Two important observations can be made at this point regarding the optical properties of a MPC made of ferromagnetic nanoantennas: i) the periodic arrangement of the scatterers induces a marked sharpening of the extinction features near λ_R, as compared to Q_{ext} of randomly distributed antennas[165] and, more importantly, ii) the optical anisotropy ΔQ induced in the system, defined as $Q_{ext-LA} - Q_{ext-SA}$ (solid violet curve in the right panel of Figure 4.3(b)), shows a clear enhancement close to the diffraction edge if compared to the randomly distributed

nanoantennas case (dashed violet curve). The second effect, which has been reported in previous studies on PCs of anisotropic gold nanoantennas[54], demonstrates how the effects of the shape anisotropy of the individual building block on the optical properties of the system can be amplified. A tuning of such effects can be obtained via proper LSMs design.

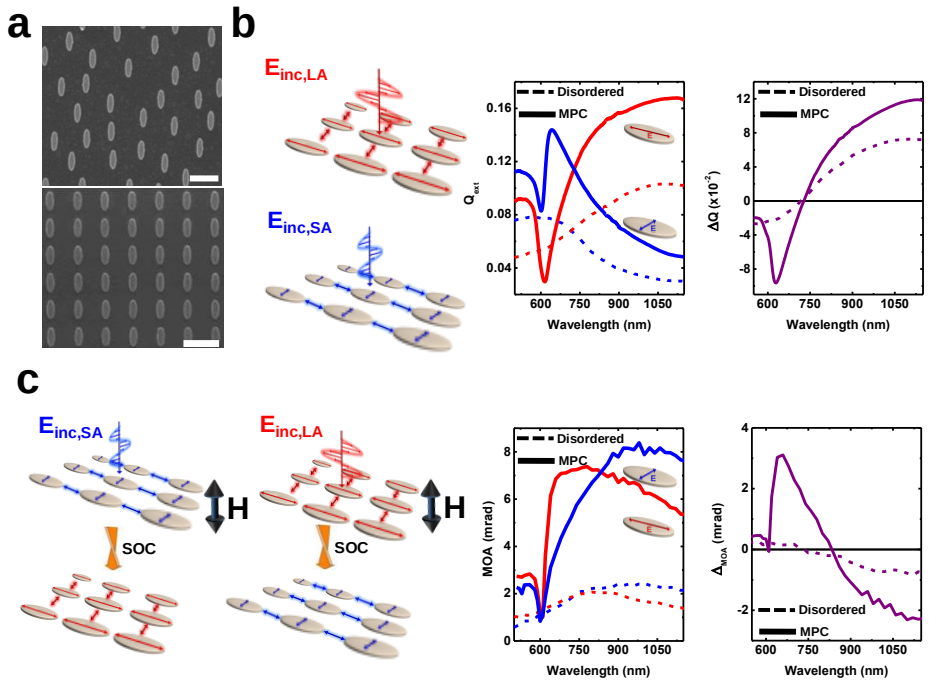

Figure 4.3: (a) SEM image of Ni elliptical nanoantennas on glass randomly distributed (top) and arranged in a square structure (bottom). The filling factor of both samples is ≈ 12%; scale bars 500 nm. Sketch of the system studied when E_{inc} is applied along the long-axis (red incident radiation) and the short-axis (blue incident radiation) (b-left panel) and of the same system shown when an external static magnetic field is applied perpendicular to the lattice plane (c-left panel). The solid arrows inside the particles represent the oscillation of the excited dipoles whereas the ones outside indicate the direction of the predominant far-field interaction in the explored spectral range. Experimental Q_{ext} (b-central panel) and MOA spectra (c-central panel) of randomly distributed elliptical nanoantennas (dashed lines) and of the MPC (solid lines) for E_{inc} applied along the short-axis (blue lines) and the long-axis (red lines). ΔQ (b-right panel) and Δ_{MOA} (c-right panel) of randomly distributed elliptical nanoantennas (violet dashed line) and of the MPC (violet solid line).

We now focus our attention on the MOA of the MPC. When E_{inc} oscillates along the SA-(LA-) direction and an external magnetic field $\boldsymbol{H}$ is applied perpendicularly to the crystal plane, the magnetic field activated spin-orbit coupling (SOC) in each nanoantenna induces a second LSPR in the LA-(SA-) direction, as demonstrated in Chapter 2.2. In our MPC, the magnitude of the magnetic field induced change in the polarization of the reflected (transmitted) light, the so-called MOA, is determined both by the electric field scattered by SOC-induced dipoles and by that originating from the dipoles directly excited by E_{inc}. The most convenient way to express the MOA of the system is through the complex Kerr angle $\widetilde{\Phi} = \theta + i\varepsilon$, where θ and ε are the Kerr (Faraday) rotation and ellipticity of the outward reflected (transmitted) electric field, respectively. Physically, the MOA is defined as the modulus of the complex Kerr angle, namely $|\widetilde{\Phi}| = \sqrt{\theta^2 + \varepsilon^2}$. Following the same reasoning used for explaining the Q_{ext} spectra in Figure 4.3(b), we now expect the MOA to be determined by MO-LSMs stemming from the diffractive coupling of the electric fields emitted by the SOC-induced dipoles and acting in the direction parallel to E_{inc}, as sketched in the left panel of Figure 4.3(c). The experimental MOA spectra measured for the present MPC, after saturating the magnetization of the nanoantennas by applying a magnetic field $|\boldsymbol{H}_{sat}|$ = 3 kOe perpendicular to the MPC plane, are shown in the central panel of Figure 4.3(c). The red and blue curves refer to an E_{inc} oscillating along the LA- and SA-direction, respectively. It is worth noting how the MOA features notably resemble those of Q_{ext} measured with the polarization of the incident field along the perpendicular direction. The experimental results in the central panel of Figure 4.3(c) confirm the intuitive picture shown in the cartoon in the left panel and are well reproduced by the following analytical formulas for the MO complex angles

$$\widetilde{\Phi}_{LA} \approx \frac{\tilde{p}_y}{\tilde{p}_x} = \frac{\tilde{\alpha}_{yx}}{\tilde{\alpha}_{xx}}\left(\frac{1}{1-\varepsilon_0\tilde{\alpha}_{yy}\,\mathcal{S}_{yy}}\right) = \frac{\tilde{\alpha}_{yx}}{\tilde{\alpha}_{xx}\,\tilde{\alpha}_{yy}}\left(\frac{1}{\frac{1}{\tilde{\alpha}_{yy}}-\varepsilon_0 S_{yy}^{FF}(\hat{x}_i)}\right) \tag{4.3}$$

$$\widetilde{\Phi}_{SA} \approx \frac{\tilde{p}_x}{\tilde{p}_y} = \frac{\tilde{\alpha}_{xy}}{\tilde{\alpha}_{yy}}\left(\frac{1}{1-\varepsilon_0\tilde{\alpha}_{xx}\,\mathcal{S}_{xx}}\right) = \frac{\tilde{\alpha}_{xy}}{\tilde{\alpha}_{xx}\,\tilde{\alpha}_{yy}}\left(\frac{1}{\frac{1}{\tilde{\alpha}_{xx}}-\varepsilon_0 S_{xx}^{FF}(\hat{y}_i)}\right) \tag{4.4}$$

where $\tilde{p}_x$ and $\tilde{p}_y$ are the LA- and SA-components of the dipole moment of the individual Ni nanoantenna, and $\tilde{\alpha}_{yx}$, $\tilde{\alpha}_{xy}$ are the off-diagonal elements of the polarizability tensor. Since the MO response is much smaller than the optical one, $\tilde{\alpha}_{yx} = -\tilde{\alpha}_{xy} \approx \tilde{x}_{SOC}\tilde{\alpha}_{xx}\tilde{\alpha}_{yy}$ with $\tilde{x}_{SOC} = -iQ\tilde{\varepsilon}_{Ni}\tilde{\varepsilon}_M/[V(\tilde{\varepsilon}_{Ni} - \tilde{\varepsilon}_M)^2]$.

Given this Eqs. (4.3) and (4.4) can be simplified as follows

$$\widetilde{\Phi}_{LA} \approx \frac{-iQ\tilde{\varepsilon}_{Ni}\tilde{\varepsilon}_M}{V(\tilde{\varepsilon}_{Ni}-\tilde{\varepsilon}_M)^2}\left(\frac{1}{\frac{1}{\tilde{\alpha}_{yy}}-\varepsilon_0 S_{yy}^{FF}(\hat{x}_i)}\right) \tag{4.5}$$

$$\widetilde{\Phi}_{SA} \approx \frac{-iQ\tilde{\varepsilon}_{Ni}\tilde{\varepsilon}_M}{V(\tilde{\varepsilon}_{Ni}-\tilde{\varepsilon}_M)^2}\left(\frac{1}{\frac{1}{\tilde{\alpha}_{xx}}-\varepsilon_0 S_{xx}^{FF}(\hat{y}_i)}\right) \tag{4.6}$$

where Q is the Voigt constant expressing the strength of the SOC, $\tilde{\epsilon}_{Ni}$ is the diagonal dielectric tensor element of bulk Ni and V the volume of the nanoantenna. From Eqs. (4.5) and (4.6) we note that the the MO complex angles $\widetilde{\Phi}_{LA}$ and $\widetilde{\Phi}_{SA}$ depend only on the MO-induced response ($\tilde{\alpha}_{yy}$ in $\widetilde{\Phi}_{LA}$ and $\tilde{\alpha}_{xx}$ in $\widetilde{\Phi}_{SA}$), in analogy with what already has been demonstrated for non-interacting magnetoplasmonic nanoantennas in Chapter 2.2. A qualitative but transparent physical insight of the result summarized in Eqs. (4.5) and (4.6) can be gained as follows. The incident radiation excites a LSM, which determines the optical response of the array. This primary LSM drives the second MO-LSM through the inherent SOC, and therefore the MO response contains both LSMs, the primary optical LSM and the SOC-induced MO-LSM. However, the MO complex angle, which identifies the polarization state of the reflected (transmitted) radiation, is the MO response divided by the optical one. This normalization "simplifies out" any effect arising from the primary LSM that is directly induced by the incident radiation. What emerges from the experimental results, which are excellently reproduced by Eqs. (4.1)-(4.6) given above, is that the MOA of the MPC is controlled by the following two key elements: i) the SOC-

induced polarizability of the individual dipole activated by $\boldsymbol{H}$, which is *transverse* to that directly excited by E_{inc} and ii) the diffractive coupling along the direction *parallel* to that of the linear polarized incident electric field leading to the excitation of a MO-LSM with a Fano lineshape. Remarkably, we observe that the excitation of MO-LSMs for both polarizations of the incident field produces a substantial enhancement and a spectral reshaping of the MOA in the MPC compared to the random case (see continuous and dashed lines in the central panel of Figure 4.3(c)). To better appreciate and quantitatively understand the advantage of exciting LSMs in MPCs with respect to random systems, we focus on the quantity plotted in the right panel of Figure 4.3(c) for the case studied here. In analogy with ΔQ we can define MOA anisotropy as

$$\Delta_{MOA} = |\widetilde{\Phi}_{LA}| - |\widetilde{\Phi}_{SA}| \tag{4.7}$$

The intrinsic shape anisotropy of the individual nanoantenna is also expected to induce a Δ_{MOA}, in analogy with the ΔQ in the optical response. However, in the disordered system this intrinsic anisotropy leads to much weaker effects in the MO spectra (violet dashed curve in Figures 4.3(c)). On the other hand, in the MPC the intrinsic shape anisotropy of the individual nanoantenna is largely amplified by diffractive coupling between the nanoantennas (violet curve in the right panel of Figure 4.3(c)) For instance, where we see almost zero Δ_{MOA} for the randomly distributed nanoantennas at λ = 740 nm, the Δ_{MOA} of the MPC shows a maximum.

Finally, we investigate what happens when the strength of $\boldsymbol{H}$ is reduced (see Figure 4.4). It is worth noting that, while the MOA intensity progressively reducesas $|\boldsymbol{H}|$ is lowered rom $|\boldsymbol{H}_{sat}|$, its pectral response does not change. This shows how the strength of the MOA and of the related polarization conversion effects, can be tuned actively and remotely by controlling the external field strength $|\boldsymbol{H}|$.

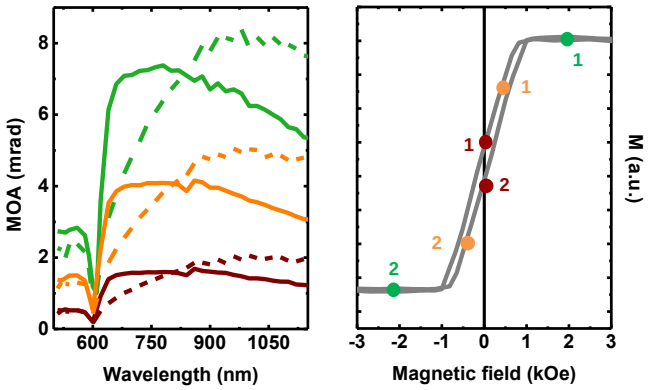

Figure 4.4: Left panel: MOA of the MPC studied in Figure 4.3 for different values of the applied magnetic field $|\boldsymbol{H}|$. Right panel: hysteresis loop of the MPC at λ = 640 nm. The curves are measured taking the value at 1 and subtracting the value at 2 for different values of $|\boldsymbol{H}|$: saturation $|\boldsymbol{H}_{sat}|$ = 3 kOe (green curve), at |H|<|Hsat| (orange curve) and at remanence $|\boldsymbol{H}|$ = 0 kOe (red curve).

4.3 Engineering of magneto-optical anisotropy

To check how far one can control the spectral lineshape of the MOA of a MPC through the in-plane plasmonic anisotropy tuning, we performed CDA calculations by fixing the square array pitch and varying the aspect ratio of the nanoantennas. By shifting the spectral position of one LSPR at a time along the principal axes of the ellipses with respect to λ_R, we first simulated square arrays of Ni nanodisks with SA = 150 nm, t = 30 nm and a LA size ranging from 187.5 nm to 487.5 nm (i.e., AR 1.25 – 3.25, respectively, see the sketch in the top panel of Figure 4.5(a)). The square lattice parameter is fixed to 500 nm: the reason for this change is to explore a wider range of LSPR blue-shifts with respect to λ_R, given also that our experimentally accessible lower wavelengths range is limited to 500 nm. A homogenous medium with refractive index n = 1.5 is assumed to model the experimental matching-oil condition. Therefore, the diffraction edge in this case is at λ_R = 750 nm. In the bottom left panel of Figure 4.5(a) we show the MOA for E_{inc} oscillating along both the SA- (solid curves) and LA-direction (dashed curves). In the latter case the MO-LSM is controlled by the lattice parameter along the LA-direction and the SA size of the Ni nanoantennas (MO-SA-LSPR), which are both fixed. As a

result, we observe that the MOA spectral lineshape does not change and its intensity slightly decreases when passing from AR = 1.25 to AR = 3.25. In striking contrast, when E_{inc} oscillates along the nanoantennas SA-direction (solid curves), we observe clear changes in the MOA spectral lineshape. In this case the MO-LSM is controlled through the nanoantennas MO-LA-LSPR, which red-shifts as we increase the AR. The calculated Δ_{MOA} is plotted in the right bottom panel of Figure 4.5(a). We observe that by manipulating the MO-LSMs lineshapes through the variation of the AR, we can produce a significant enhancement of Δ_{MOA} in a narrow spectral region centered around λ = 850 nm. Here the maximum of Δ_{MOA} increases with increasing AR and saturates at the remarkable value of almost 7 mrad (about twice the value displayed in the right panel of Figure 4.3(c)) for AR = 2.75. Complementarily, in Figure 4.5(b) we analyze the effects of SA-LSPR tuning on the MO-LSMs spectral lineshapes (see the illustration in the top panel of Figure 4.5(b)). We considered square MPCs made of Ni nanodisks with LA = 150 nm, t = 30 nm and SA ranging from 75 nm to 50 nm (i.e., AR 2 – 3, respectively). As in the previous case, a = 500 nm and n = 1.5. The results of the CDA calculations, displayed in the bottom panel of Figure 4.5(b), show that now the huge variation in the MOA spectral lineshape and intensity is occurring when the incident electric field is polarized along the LA-direction (solid curves in the left bottom panel of Figure 4.5(b)). This is consistent with the physical picture developed so far, since the MOA depends, in this case, on the MO-LSM tuning caused by the MO-SA-LSPR blue-shift with respect to λ_R induced and controlled by varying the SA of the elliptical nanoantennas. In straightforward analogy with the previous case, for E_{inc} polarized along the SA-direction the MOA spectral lineshape shows only minor changes, since the MO-LSM in this case is controlled by the nanoantennas MO-LA-LSPR, which is induced along the fixed LA dimension (see dashed curves in the left-bottom panel of Figure 4.5(b)). Interestingly, for an AR between 2 and 2.25 for the nanoantennas size and lattice parameter ranges considered here, we observe a complete isotropic MOA in a specific and narrow spectral region., in spite of the anisotropic character of the individual dipoles (see the right-bottom panel of Figure 4.5(b)). It is worth mentioning that all the above discussed effects arising from the excitation of LSMs in MPC, can be transferred to any other spectral position by varying the lattice parameter and/or the overall sizes of the nanoantennas principal axes.

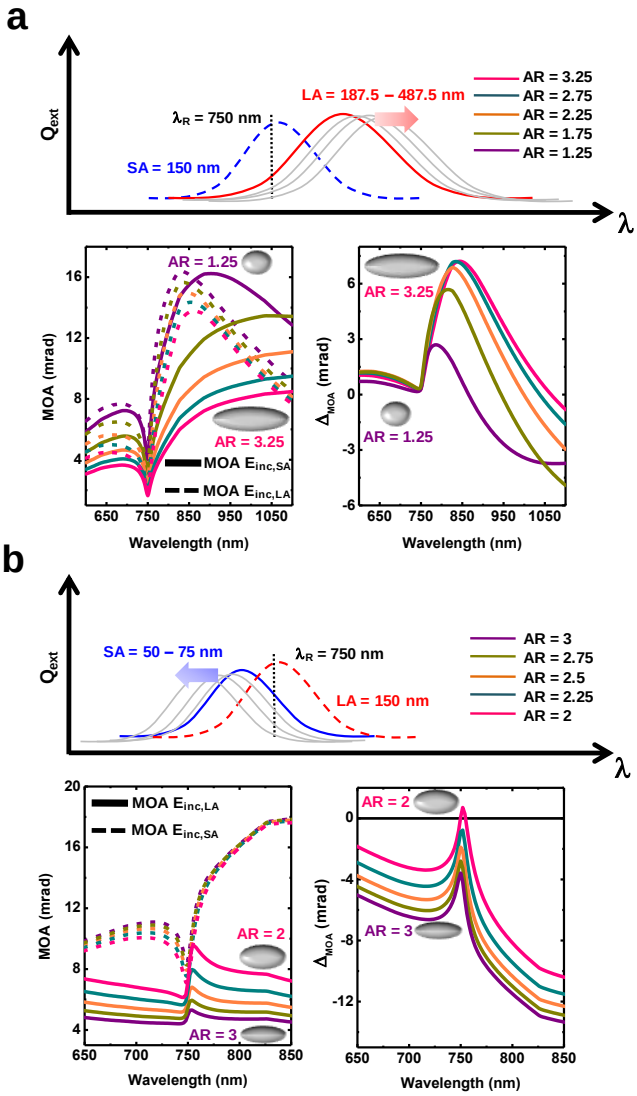

Figure 4.5: (a) Top panel: sketch of LSPRs of an isolated elliptical nanoantenna. The SA diameter is 150 nm. The LA diameter is changed from 187.5 nm to 487.5 nm (AR 1.25-3.25), a = 500 nm along both LA- and SA-direction and t = 30 nm. (a) Left-bottom panel: MOA for E_{inc} parallel to the LA (dashed curves) and to the SA (solid curves) of the antennas. (a) Right-bottom panel: Δ_{MOA} of the MPC for different AR ranging from 1.25 to 3.25. (b) Top panel: as in (a), but with the LA diameter equal to 150 nm. The SA diameter is varied from 75 nm to 50 nm; a = 500 nm along both LA- and SA-direction and t = 30 nm. (b) Left-bottom panel: MOA for E_{inc} parallel to the LA of the antennas (solid curves) and for E_{inc} parallel to the SA of the antennas (dashed curves). (b) Right-bottom panel: Δ_{MOA} for the MPC for different AR ranging from 2 to 3.

To experimentally prove the potential and versatility of MO-LSMs tuning in MPCs, we fabricated two MPCs aimed at achieving the two key cases presented in Figure 4.5, namely the enhancement of Δ_{MOA} by a factor of two as compared with the case presented in Figure 4.3, and the achievement of MOA isotropy in selected and narrow spectral ranges. Control samples with randomly arranged nanoantennas with the same filling factor and dimensions of the individual units in the MPCs, were fabricated and measured as reference. To prove the first case, namely the amplification of Δ_{MOA} in a selected spectral range, the SA and LA of the elliptical nanoantennas were chosen to be 150 nm and 400 nm, respectively, the same as for the MPC predicted to display the maximum Δ_{MOA} (case corresponding to AR = 2.75 in the bottom-right panel of Figure 4.5(a)). The fabricated nanoantennas have t = 30 nm, and in the MPC they are arranged in a square lattice with a = 500 nm. Since in this case the LA dimension of the nanoantennas is not much smaller than the wavelength of the incoming light, we checked its optical response with both CDA and FDTD simulations. We verified that, in the case of Ni nanoantennas up to the dimenisons considered in this case, the formation of LSMs is always dominated by the strongly radiating dipolar mode of the nanoantennas. This conclusion is further corroborated by the excellent agreement between the spectra calculated using the CDA (Figure 4.5) and those measured experimentally (Figure 4.6). Figure 4.6(a) shows a SEM image of a portion of the MPC (top panel) and of the randomly distributed nanoantennas (bottom panel) fabricated by EBL. In the top panel of Figure 4.6(b) we show the Q_{ext} spectra of both the MPC and the randomly distributed nanoantennas. For the MPC we observe two very different sharp features around the diffraction edge at 750 nm for E_{inc} applied along LA (red solid curve) and SA (blue solid curve), while for the random system we see two spectrally displaced and very broad plasmonic peaks (red and blue dashed curves). Similarly, both the MOA_{LA} and MOA_{SA} spectra, which are shown in the bottom panel of Figure 4.6(b), feature the expected Fano lineshape with a dip at 750 nm and enhanced peaks at λ = 850 nm (E_{inc} along LA-direction, solid red line) and at λ = 1100 nm (E_{inc} along SA-direction, solid blue line). This behavior is in excellent agreement with the calculations presented in Figure 4.5(a) and leads to the predicted enhacement of a factor of two of Δ_{MOA} (at λ = 825 nm) as compared with that of the initial MPC sample shown in Figure 4.3. It is clear from these experiments the outstanding

enhancement of Δ_{MOA} produced by the resonant excitation of MO-LSMs in the MPC when compared to that of a disordered assembly of the same constituent units. This is clearly appreciable in the bottom panel of Figure 4.6(c), where we plot the ΔQ (top-panel), and Δ_{MOA} (bottom-panel) for both the MPC (violet solid lines) and the random system (violet dashed lines).

Finally, in order to prove experimentally the predicted achievement of a wavelength-dependent isotropy of the MOA in a selected and narrow spectral range, we fabricated a MPC composed by elliptical nanoantennas with LA = 150 nm, SA = 80nm, t = 30 nm and arranged in a square lattice with a = 500 nm. The AR was chosen to be as close as possible, compatibly with our nanofabrication limits, to that prescribed by simulations in order to achieve the desired effect (AR = 1.87 for the real sample versus AR between 2 and 2.25 in the calculations). Also for this case, we fabricated a control random sample with the same type of nanoantennas and identical filling factors. SEM images of portions of both samples are shown in Figure 4.6(d).The experimental Q_{ext} and MOA spectra of the MPC are shown in Figure 4.6(e) (top and bottom panel, respectively). The MOA_{LA} and MOA_{SA} spectra (red and blue solid curves in bottom panel of Figure 4.6(e), respectively) reproduce very well the lineshapes predicted by calculations (left bottom of Figure 4.5(b)). Also in this case the excitation of MO-LSMs in the MPC induces profound differences in the MOA spectra when compared to a disordered assembly of the same constituent units (red and blue dashed curves in the bottom panel of Figure 4.6(e)). Most importantly, Δ_{MOA} spectra plotted in the bottom panel of Figure 4.6(f) for the MPC case (solid violet curve) excellently matches the modeling predictions as it displays the achievement of an almost perfect MOA isotropy in a narrow range of wavelengths around 770 nm. Noteworthy, the MOA_{LA} and MOA_{SA} spectra for the random sample (dashed red and blue curves in Figure 4.6(e)) as well as Δ_{MOA} (dashed violet curve in the bottom panel of Figure 4.6(f)) show a negligible anisotropy over the whole spectral range explored. This further confirms the key role played by the excitation of LSMs in determining the MOA of a MPC and the huge potential of using ordered systems to increase MO effects in magnetic plasmonic nanostructures.

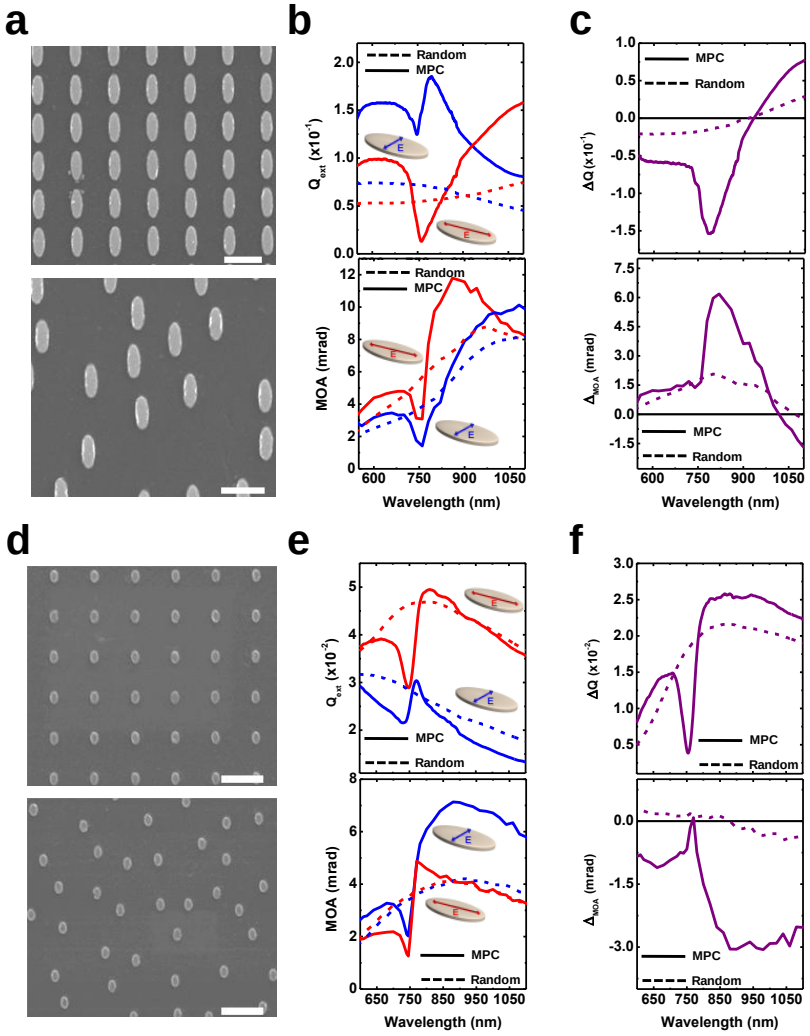

Figure 4.6: Top-panel: elliptical antennas with in-plane dimensions of 150 nm and 400 nm, and thickness t = 30 nm. (a) top: SEM image of a portion of the ordered array; pitch a = 500 nm; scale bar 500 nm. (a) bottom: SEM image of a portion of the random array; scale bar 500 nm. (b) Q_{ext} (top) and MOA (bottom) of the periodic (continuous lines) and random (dashed lines) arrays, for E_{inc} applied along the LA (red lines) and along the SA (blue lines). (c) ΔQ (top) and Δ_{MOA} (bottom) for the MPC (continuous lines) and random array (dashed lines). Bottom-panel: elliptical antennas with in-plane dimensions of 80 nm (SA) and 150 nm (LA), and thickness of 30 nm. (d)-top panel: SEM image of a portion of the ordered array; a = 500 nm. (d)-bottom panel: SEM image of a portion of the random array. Scale bars 500 nm. (e) Q_{ext} (top) and MOA (bottom) of the periodic (continuous lines) and random (dashed lines) arrays, for E_{inc} applied along the LA (red lines) and along the SA (blue lines). (f) ΔQ (top) and Δ_{MOA} (bottom) for the MPC (continuous lines) and random array (dashed lines).

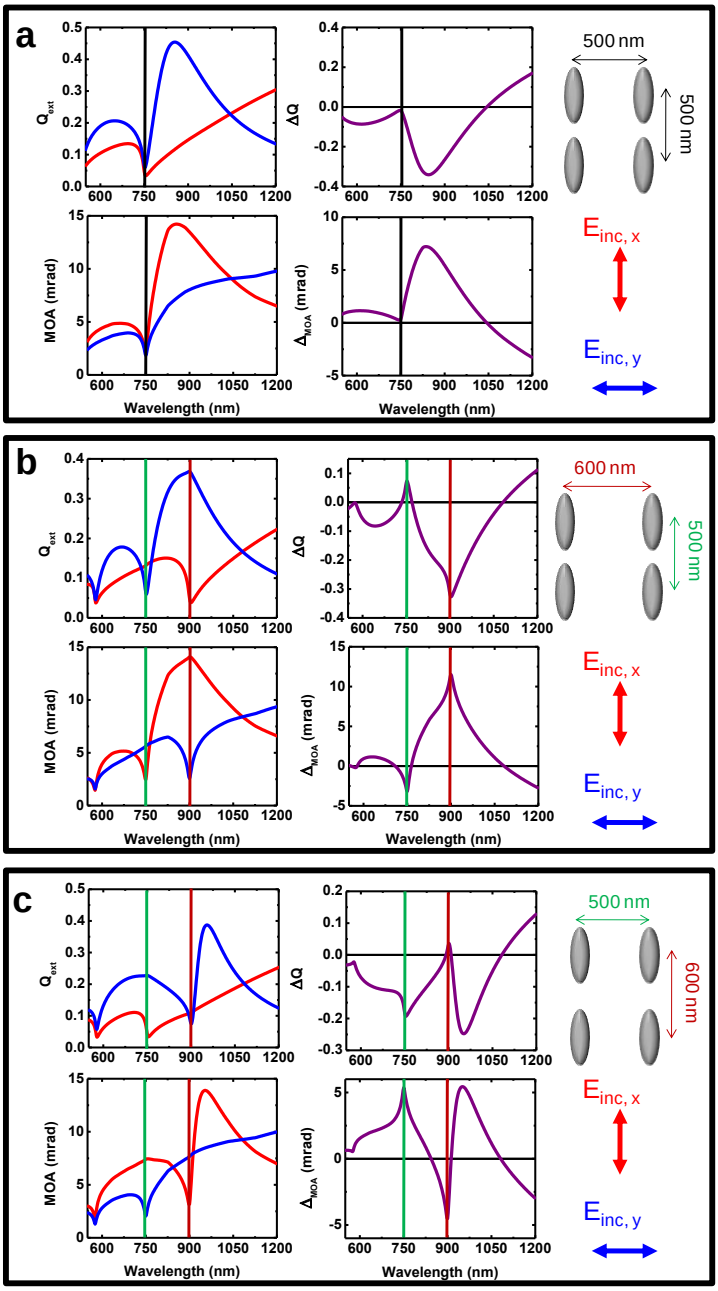

Figure 4.7: MPC of nickel antennas with LA = 400 nm, SA = 150 nm and t = 30 nm. In each panel are shown calculated Q_{ext} (top left), MOA (bottom left), ΔQ (top right) and Δ_{MOA} (bottom right). (a) Square lattice: pitch a = 500 nm along both LA- and SA-direction. (b) Rectangular lattice: pitch a = 500 nm along the LA-direction and a = 600 along SA-direction. (c) Rectangular lattice: pitch a = 600 nm along the LA-direction and a = 500 along SA-direction.

Before concluding, it is worth briefly addressing the effects arising from varying the lattice symmetry. The use of other arrangements, like hexagonal or honeycomb lattices, is not expected to display additional effects different from those occurring in square lattices. Indeed, as discussed deeply in Ref. [162], such symmetries are highly isotropic in terms of LSMs excitation (see for instance Figure 7 of the Ref. [162]). In contrast, rectangular lattices provide an additional source of anisotropy[164] that can be used, in combination with the anisotropy of the individual building block, to induce a further enhancement (Δ_{MOA} exceeding 10 mrads), a compensation or even a change of sign of ΔQ and Δ_{MOA}, respectively, at selected wavelengths. This is indeed the case, as shown by the calculated curves plotted in Figure 4.7, where the exemplary case of the MPC treated in Figure 4.6(a)-(c) has been chosen. Figure 4.7 shows that by choosing two different lattice parameters along the antennas principal directions one can induce either enhancement or suppression of ΔQ and Δ_{MOA}, in selected spectral regions.

4.4 Conclusions

We presented a new concept of magnetoplasmonic crystal based on the excitation of Fano lattice surface modes in periodically arranged magnetic antennas that show anisotropic in-plane plasmonic responses. The excitation of lattice surface modes in this kind of systems is governed by the polarizability of the single antenna and the relative position between localized resonances in the individual building blocks and diffraction edges induced by the periodicity of the crystal lattice. The different in-plane optical response, generated by the coherent excitation of radiative far-field interactions between the nickel nanoantennas, along two transverse directions, which are coupled by the application of an external magnetic field, leads to a significant enhancement of the magneto-optical effects in either narrow or large regions of the visible and near-infrared spectrum. We envisage that the concept of magnetoplasmonic crystal presented here will open up excellent nano-engineering opportunities towards enhanced and generally designed magneto-optical applications such as nanostructured magnetoplasmonic metasurfaces for the control of light polarization states and improved nanoscale detection schemes.

5. SPPs assisted magneto-optical activity in 2D magnetoplasmonic crystals

In this Chapter we explore further the potential of the synergy between intrinsic magneto-optical mediated polarization conversion and plasmon excitations in ordered systems by substituting localized with propagating surface plasmon polaritons in an archetypical 2D-magnetoplasmonic crystal made of periodic cylindrical holes in a ferromagnetic metallic layer. We present a comprehensive experimental and theoretical study demonstrating that the coupling of free space radiation to surface plasmon polariton modes in conjunction with the inherent magneto-optical activity enable cross-coupling of propagating surface plasmon polariton modes. We observe that the magneto-optical spectral response arises from all the excitable surface plasmon polariton modes in the magnetoplasmonic crystal irrespective of the incoming light polarization. We demonstrate that an enhancement of the Kerr effect is induced when special non-collinear surface plasmon polariton modes, which couple to both p- and s-polarized light, are resonantly excited. We also show how the resonant enhancement of the Kerr effect can be set at desired radiation wavelengths and incidence angles by precise plasmonic band engineering achievable through the proper design of the magneto-plasmonic lattice structure.

5.1 Introduction

A surface plasmon polariton (SPP) is a combined excitation of a transverse magnetic (p-polarized) electromagnetic wave coupled to surface plasma charge oscillations, as explained in Chapter 1.1. SPPs propagate at a metal/dielectric interface, and the associated electromagnetic field is evanescently confined in the perpendicular direction to the interface. Similar to electrons in a crystal potential, when a periodic modulation of the metal surface is introduced, the dispersion relation of SPP modes on a flat metal surface forms a band structure, bringing about band-related concepts like phase and group velocity, photonic densities of states, and propagation anisotropy. This situation can be realized in one- or two-dimensional diffraction gratings, whose optical properties rely on the generation of Bloch-like photonic band structures. Moreover, while in a continuous film SPPs can couple to the free space radiation using only impinging p-polarized light, efficient coupling of both p- and s-polarized (transverse electric polarized wave) light to SPP waves can be achieved through diffraction in metal surfaces with periodic arrangements of sub-wavelength scale structures.[166-171] This property has been widely studied in the recent years in two-dimensional (2D) periodically patterned metal surfaces, named 2D plasmonic crystals (2D-PC), for the design and optimization of SPP-light coupler devices. Remarkable examples are 2D-PC that make use of SPPs to give rise to extraordinary light transmission effects or to concentrate light in mirrors, wave guides, and cavities, whose enhanced light-matter interaction can be used in a broad variety of applications such as light modulators, devices for light energy harvesting, and bio-sensors.[172-177]

Intrinsic coupling of localized plasmonic modes through spin orbit (SO) induced polarization conversion has been demonstrated in Chapter 2.2 for LSPRs in magnetic plasmonic nanoantennas. Here, we explore further the potential of the synergy between magneto-optical (MO) mediated polarization conversion and plasmon excitations by substituting LSPRs with SPPs in an archetypical 2D-magnetoplasmonic crystal (2D-MPC) made of periodic cylindrical holes in a ferromagnetic metallic layer. Perforated magnetic films implementing 2D-MPCs have been intensely studied in recent years, focusing in particular on polar geometry[23, 178, 179] At oblique incidence, when p- and s-

polarizations are defined, the great majority of the studies focused on the transverse MO Kerr effect (MOKE), driven by the notion that SPPs are efficiently excited by p-polarized electric field.[52, 180-184] More recently the longitudinal MOKE (L-MOKE) configuration was also considered.[185] In this configuration, the incident light can be either p- or s-polarized. However, the case of s-polarized light received very limited attention. Here we show, by performing dedicated experiments and theoretical simulations, the possibility in L-MOKE geometry to excite with *both* p- and s-polarized *non-collinear* (wave-vectors of the incident light and of the SPP not parallel) and bi-directional SPPs (twofold degenerate bands with SPPs propagating in different directions) can be used for the resonant enhancement of the magneto-optical activity (MOA) of 2D-MPCs. The underlying mechanism relies on the coupling between such SPPs enabled by the MO-induced polarization conversion upon meeting specific conditions (light incidence angle and wavelength, orientation of the crystal lattice with respect to the in-plane electric field component, etc…), which are pre-settable by design the lattice geometry and symmetry. We show that the most interesting features observed in the L-MOKE spectra, namely appearance of resonant lineshapes and notable enhancement of the MOA, arise from the interference between reflected light due to SPP modes directly excited by the incident light and light re-emitted by the MO-induced SPP modes, whose polarization is perpendicular to that of the incident electric field. Besides providing a deeper understanding of light matter coupling in 2D-MPCs, our results disclose how to exploit the SPPs coupling activated by the MO-mediated polarization conversion via plasmonic band engineering leading to enhancement of MO effects at desired wavelengths.

5.2 Optical properties of 2D-MPCs supporting SPPs

The system studied was a 2D-MPC made of sub-wavelength holes in a continuous film – 80 nm thick – of Permalloy ($Ni_{80}Fe_{20}$ or Py) on a Si substrate arranged on a square lattice.[186] A SEM image of a portion of the system is shown in Figure 5.1(a). The lattice constant is 400 nm ± 5 nm and the diameter of the holes is 265 nm ± 5 nm. The system reflectivity, as well as the L-MOKE (Figure 5.1(b)), were measured.

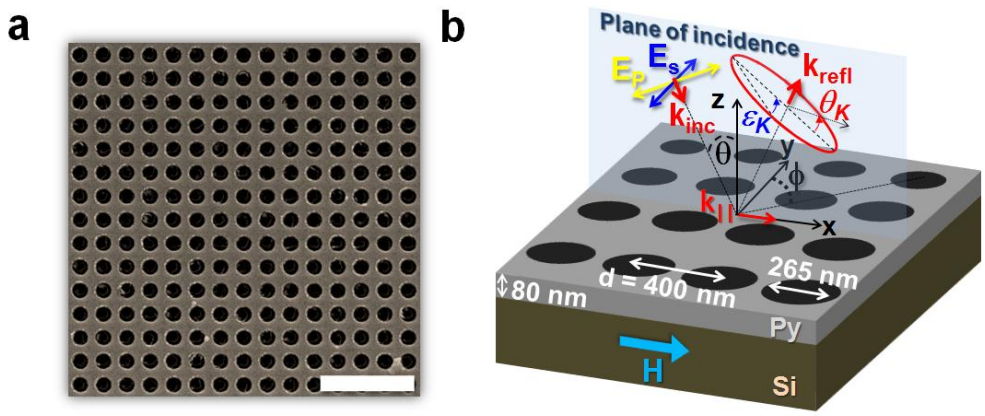

Figure 5.1: (a) SEM image of a portion of the 2D-MPC studied. Scale bar 1.5μm. (b) Sketch of the 2D-MPC in the L-MOKE configuration: upon the application of an external in-plane magnetic field ***H***, which is parallel to the plane of incidence and fully magnetizes the sample, MOA is induced in the system and the reflected light polarization is elliptical and rotated compared to the original direction.

We start investigating the plasmonic band structure of the 2D-MPC by performing angular resolved reflectivity experiments in the VIS and NIR spectral range (380-800 nm), and by numerical simulations using an adapted scattering matrix method (SMM) approach able to describe both the optical and MO effects in periodically patterned multilayer systems.[187] As input elements for the numerical simulations tabulated experimental optical and MO dielectric constants of Py were used.[188] Representative reflectivity spectra has been measured and calculated for both p- (Figure 5.2) and s-polarization (Figure 5.3), for three different angles of incidence (θ = 30°, 45° and 60°), and for the two high-symmetry azimuthal configurations (ϕ = 0° and 45°). In Figure 5.2(a) we display the measured reflectivity of a reference Py continuous film, which was deposited simultaneously during the fabrication of the 2D-MPC, for the same values of θ mentioned previously. No particular features are present in the reference film spectrum that could be ascribed to coupling of incident light to SPP modes in the explored experimental range. As discussed in Chapter 1.1, this is what is expected for a continuous metallic film where the dielectric medium hosting the incoming wave and that is in contact with the metal is air.

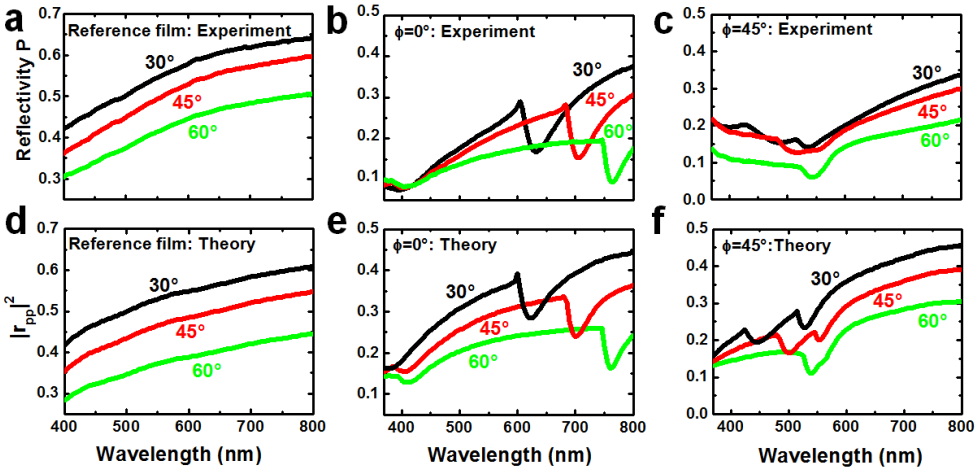

Figure 5.2: p-polarized incident light case. Reflectivity spectra of the reference film (a), of the 2D-MPC at ϕ = 0° (b) and at ϕ = 45° (c). Calculated reflectance of the reference film (d), of the 2D-MPC at ϕ = 0° (e) and at ϕ = 45° (f). Black lines – θ = 30°, red lines – θ = 45°, green lines – θ = 60°.

In Figure 5.2(b) we plot the experimental reflectivity spectra of the 2D-MPC at ϕ = 0° for the same values of θ. In this case, we notice two Wood's anomalies (WAs) clearly identifiable by two spectral dips, which are brought about by the introduction of periodicity and are the signature of light coupling to a SPP mode. We observe a slightly θ-dispersive WA in the range 380-410 nm, weakly red-shifting when increasing θ. A more θ-dispersive WA, also red-shifting as θ increases, is observed in the range 600-800 nm. In Figure 5.2(c) we plot the experimental reflectivity spectra at ϕ = 45° and for the same values of θ that clearly display two separated WAs at θ = 30° (black line), which progressively get closer to each other as θ is increased (red line θ = 45° and green line θ = 60°). These experimental results agree well with the numerical calculations performed using SMM. In the calculations the reflectance is calculated as $|r_{pp\,(ss)}|^2$, where $r_{pp\,(ss)}$ is the complex Fresnel coefficient of the reflected light for p(s)-polarized light (see Figures 5.2(d)-(f)). In Figure 5.3(a) we show the measured reflectivity spectra for s-polarized incident light of the reference continuous film for the same values of θ. Also in this case no particular features traceable to the excitation of SPP modes are present in the reference film spectrum.

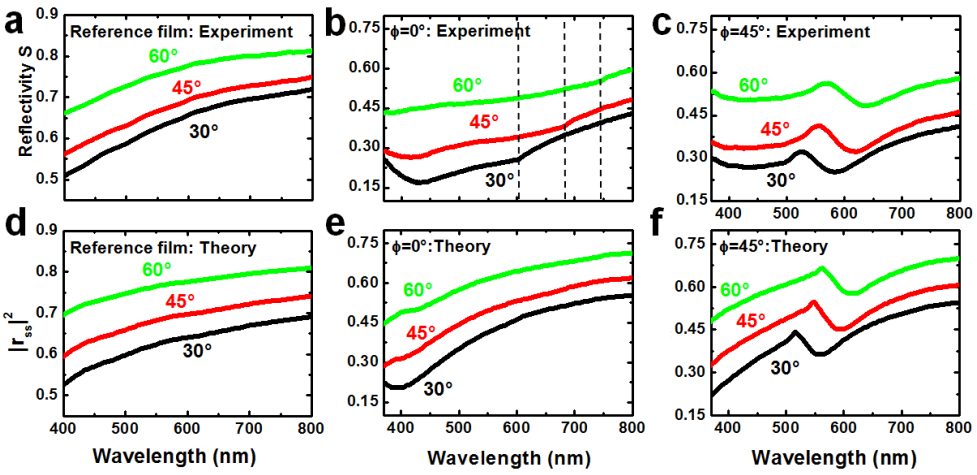

Figure 5.3: s-polarized incident light case. Reflectivity spectra of the reference film (a), and of the 2D-MPC at ϕ = 0° (b) – dashed lines indicate the position of he Rayleigh's anomalies – and at ϕ = 45° (c). Calculated reflectance of the reference film (d), and of the 2D-MPC at ϕ = 0° (e) and at ϕ = 45° (f). Black lines – θ = 30°, red lines – θ = 45°, green lines – θ = 60°.

In Figure 5.3(b) the experimental reflectivity spectra of the 2D-MPC using s-polarized light and with ϕ = 0° for the three selected values of θ do not display the resonant excitation of any SPP mode in the spectral range 600-800 nm at variance with the p-polarization case. In this case, only a small kink due to the occurrence of a Rayleigh's anomaly is visible (see the vertical dashed lines in Figure 5.3(b)). For this particular sample orientation, the reflectance spectra show a weak WA in the range 380-410 nm. The shallow dip produced by the WA in the spectra is slightly red-shifted and broader with respect to that observed using p-polarized light. This kind of broadening and red-shifting of WAs excitable with both polarizations, when the light polarization is changed from p to s, has been already observed in PCs.[167, 168] In Figure 5.3(c) we display the experimental reflectivity of the 2D-MPC for s-polarization and ϕ = 45° and for the same values of θ. Now, the s-polarized incident light can resonantly excite only one SPP mode in the wavelength range 500-650 nm, whose θ-dispersive behavior displayed by the corresponding WA is the same as that of the WA appearing at longer wavelength in the same spectral range using p-polarized light. Again, the experimental results are in

excellent agreement with numerical calculations of the Fresnel coefficients using SMM (see Figures 5.3(d)-(f)).

In order to identify the excited SPP modes that correspond to the WAs observed in the spectra, we calculated the plasmonic dispersion bands using a perturbative approach valid in the limit of vanishingly small holes[172], which does not take into account neither the dimensions of the holes nor the cross section of the light-SPP coupling[168, 172]. In this approximation the plasmonic bands are obtained from wave-vector conservation relationship, in which the contribution of the diffraction grating is included, as follows

$$|k_{SPP}|^2 = (k_x + mG_x)^2 + (k_y + nG_y)^2 \quad (5.1)$$

where $k_x = k_0 sin\theta cos\phi$ and $k_y = k_0 sin\theta sin\phi$ are the *x* and *y* projections of the incident light wave vector k_0, respectively, $G_x = 2\pi/d_x$ and $G_y = 2\pi/d_y$ are the *x* and *y* components of the lattice reciprocal vector $\boldsymbol{G}$, and n and m are relative integers $(\pm 1, \pm 2, \dots)$. The values of the lattice parameter along *x*- and *y*-direction are labeled with d_x and d_y, respectively. In the case of a square lattice investigated here, $d_x = d_y = d$. Two different kind of modes are identified (see also Figure 5.5(a)): i) plasmonic bands with $\boldsymbol{k}_{||}$ parallel to $\boldsymbol{G}$ and thus to k_{SPP} (*collinear case*); each band of this type corresponds to a a SPP wave propagating with k_{SPP} either parallel or antiparallel to $\boldsymbol{k}_{||}$; ii) plasmonic bands for which $\boldsymbol{k}_{||}$ *is not* parallel to $\boldsymbol{G}$ and, thus, neither to k_{SPP} (*non-collinear case*). In the non-collinear case, the plasmonic band originates from two *degenerate* SPP waves propagating in different directions (k_{SPP1} and k_{SPP2} with $|k_{SPP1}| = |k_{SPP2}|$). Noteworthy, the two SPP waves propagating with wave-vectors k_{SPP1} and k_{SPP2} are coupled due to their energy degeneracy. As a consequence, the non-collinear bands actually correspond to the dispersion relation of two coupled SPP modes that can be described as the superposition of the two SPP waves with k_{SPP1} and k_{SPP2}. The symmetries of the resulting coupled SPP modes impose selection rules on their coupling to linearly polarized free-space plane waves. The result is that each coupled mode can only be excited by free-space radiation with a specific polarization, either p- or s-.[172] The plasmonic dispersion

bands calculated using the perturbative approach and labeled with (m,n) indexes, correlate well to the salient features in the calculated reflectivity maps calculated using the SMM (Figure 5.5(b)-(e)), which computes the light-SPP coupling cross section taking into account the symmetry selection rules as well as the holes-size effect. The vertical colored lines in Figure 5.5(b)-(e) indicate the three values of θ corresponding to the experimental spectra shown in Figure 5.2 and Figure 5.3, namely 30°, 45°, and 60°. The intersection between these lines and the dispersion bands allow us to precisely correlate the SPP modes excited to the WAs observed in the experimental spectra. A first result from the inspection of Figures 5.5(b)-(c) is that p-polarized light can excite SPP modes of both kinds, collinear and non-collinear, although with different efficiency. On the contrary, s-polarized light can excite only SPP modes of the second kind (non-collinear case, black dashed lines). In the case of p-polarized light and ϕ = 0° (Figure 5.5(b)), the intersections with the vertical lines reveal that the excited SPP modes observed experimentally in Figure 5.2 are the mode (-1,0) in the range 600-800nm (collinear case, black solid line), and one of coupled modes originated by the (-1,+1) and (-1,-1) SPP waves in the range 380-410nm (degenerate plasmonic bands, non-collinear case, black dashed line). For ϕ = 45° (Figure 5.5(c)) the intersection indicates that the incoming p-polarized light couples to a coupled mode arising from the two degenerate directional SPP waves (-1,0) and (0,-1) (non-collinear case for this orientation of the array, black dashed lines in Figure 5.5(c)). The other SPP mode excited is the (-1,-1), which for this orientation of the sample corresponds to a collinear case (solid black line). In the case of s-polarized light and for ϕ = 0° (Figure 5.5(d)) the plasmonic band (-1,0) is not accessible due to selection rules.[172] A coupled mode arising from the SPP waves in the degenerated (-1,+1) and (-1,-1) plasmonic bands can be excited at 400 nm (non-collinear case). For ϕ = 45° (Figure 5.5(e)), s-polarized light can couple only to a coupled mode due to the two SPP waves in the degenerate (-1,0) and (0,-1) plasmonic bands (non-collinear case, black dashed line) alike in the p-polarization case. In this case, the coupling of the s-polarized light to the SPP mode in the (-1,-1) plasmonic band, corresponding to the collinear case for this orientation of the sample, is prevented by symmetry selection rules (grey dashed-line).

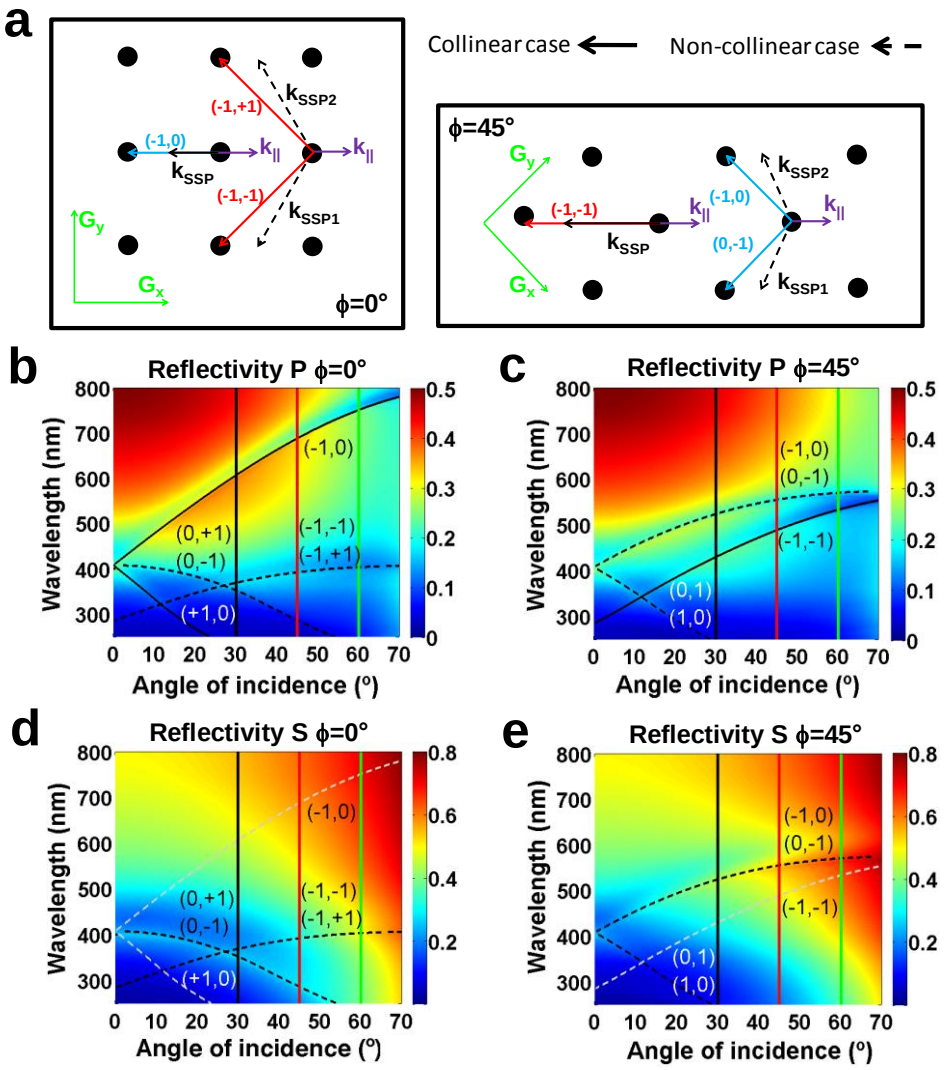

Figure 5.5: (a) Left panel: sketch of collinear and non-collinear SPP mode in the reciprocal space for ϕ = 0°. Right panel: sketch of collinear and non-collinear SPP mode in the reciprocal space for ϕ = 45°. (b) Reflectivity of the system for p-polarized light and ϕ = 0°. The vertical solid lines indicate the three angles of incidence studied experimentally. The black solid lines indicate the collinear modes, whereas the black dashed lines indicate the non-collinear modes. (c) Reflectivity of the system for p-polarized light and ϕ = 45°. (d) Reflectivity of the system for s-polarized light and ϕ = 0°. The grey dashed lines are the forbidden collinear modes for the s-polarization case. (e) Reflectivity of the system for s-polarized light and ϕ = 45°. All the lines indicating allowed/forbidden modes are calculated using Eq. (5.1). The different color (black or white) used for labelling the modes is just for improving their legibility.

To summarize and conclude this section, we highlight that for both ϕ = 0° and ϕ = 45° there are collinear SPP modes that can be excited only with p-polarized light, while there are non-collinear and degenerate SPP coupled modes that can be excited by either s- or p-polarized light: for ϕ = 0° these latter type of SPP coupled modes arise from the superposition of SPP waves whose dispersion is described by the degenerate (-1,+1) and (-1,-1) plasmonic bands, while for ϕ = 45° they result from the superposition of SPP waves in the degenerate (-1,0) and (0,-1) bands.

5.3 Magneto-optical properties of 2D-MPCs

We then investigated the plasmonic band structure in the MO response of our 2D-MPC through L-MOKE. Figure 5.6 shows the experimental and theoretical L-MOKE spectra of the reference film and of the 2D-MPC for the same three values of θ and for the two orientations of ϕ of the reflectivity spectra shown in Figures 5.2 and Figure 5.3. More precisely, Figure 5.6 displays the MOA of the reference film and of the 2D-MPC at saturation. As the reflectivity spectra, the MOA of the reference film does not display any particular feature for neither light polarization states that can be traced back to the resonant excitation of SPP modes (Figures 5.6(a)-(b)). In the case of the 2D-MPC, resonances with an asymmetric line shape are clearly observed in the spectra shown in Figures 5.6(c)-(f). The most salient result is the similarity of the spectral line shapes measured with s- and p-polarized light, which carry signatures of *all* the excitable SPP modes discussed above, *irrespective* of the incident light polarization. Given the previous discussion on Figure 5.5, namely that p-polarized light can couple to all modes present in the selected spectral range, whilst s-polarized one only to a subset of them, this result is unexpected and points to the fact that through the intrinsic MO-induced polarization conversion *all* the excitable SPP modes contribute to determine the MOA. In more detail, for ϕ = 0° we observe a deviation from the continuous film response of the MOA for both polarizations (Figures 5.6(c)-(d)), which corresponds to the excitation of the collinear SPP mode (-1,0) in the wavelength range 600-800 nm. This mode cannot couple directly to s-polarized incident light, as discussed above. Therefore, it appears in the MOA

measured with s-polarized light because it is excited via the conversion between s- and p-polarizations provided by the intrinsic MO nature of the 2D-MPC. Moreover, this polarization conversion effect seems to be very efficient as the spectral intensities of the plasmon-induced features are very similar for the two polarizations, although in the p-polarization case the mode (-1,0) is excited directly by the incident light, while in the s-polarization case it is excited via the MO coupling.

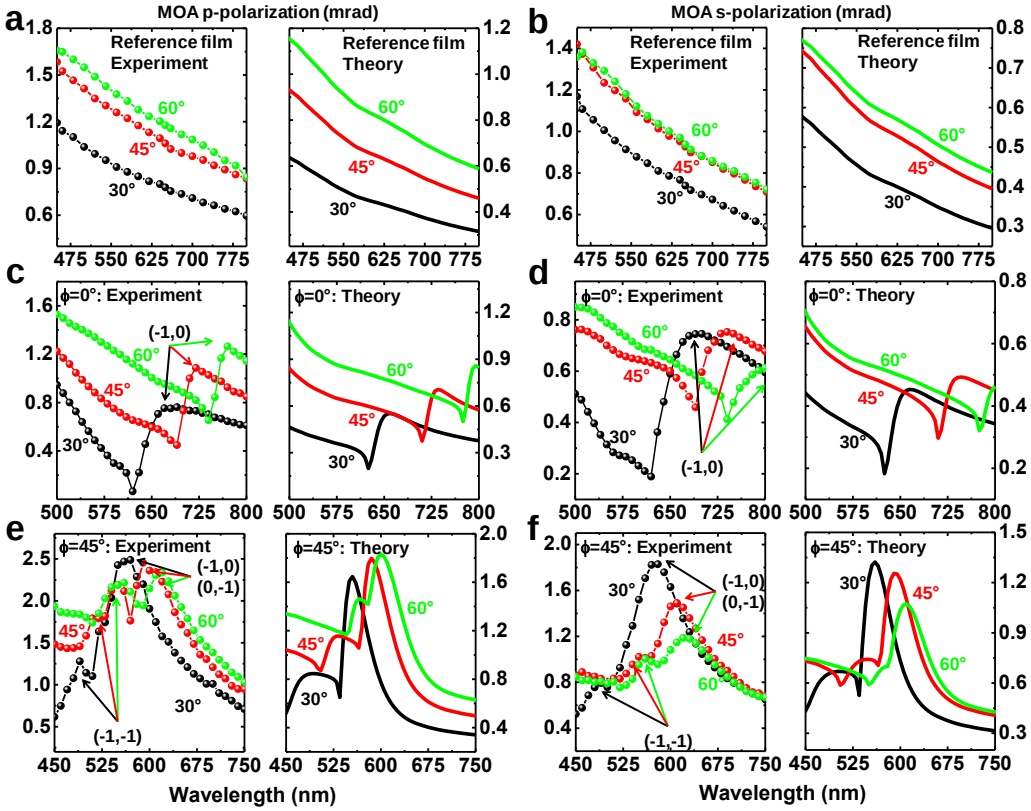

Figure 5.6: MOA of the 2D-MPC for θ = 30° (black lines), θ = 45° (red lines), θ = 60° (green lines). Experiments (left panels) and calculations (right panels). (a) MOA of the reference film with p-polarized light. (b) MOA of the reference film with s-polarized light. (c) and (e) show the MOA of the 2D-MPC with p-polarized light at ϕ = 0° and ϕ = 45°, respectively. (d) and (f) show the MOA of the 2D-MPC with s-polarized light at ϕ = 0° and ϕ = 45°, respectively.

The MO-mediated coupling between polarized light and SPP modes is further corroborated in the even more interesting case of ϕ = 45° (Figures 5.6(e)-(f)). In this case we see signatures of all the possible modes in the explored spectral range for both light polarizations. These modes are the (-1,-1) collinear case, and the two degenerate coupled modes arising from the (-1,0) and (0,-1) non-collinear SPP waves, yielding to a clear and remarkable enhancement of the MOA with respect to the non-perforated film in the wavelength range 550-600 nm, at variance with the previous case of ϕ = 0°, and up to a factor ~2.5 in the case of p-polarization. The single polarization parameters, rotation and ellipticity, show the same enhancement compared to the film case (see Figure 5.7 for the case ϕ = 45° and θ = 30°). This remarkable enhancement results from the possibility of the *simultaneous excitation* of the two degenerate coupled modes arising from the non-collinear SPP waves (-1,0) and (0,-1) with both s- and p-polarized incident light.

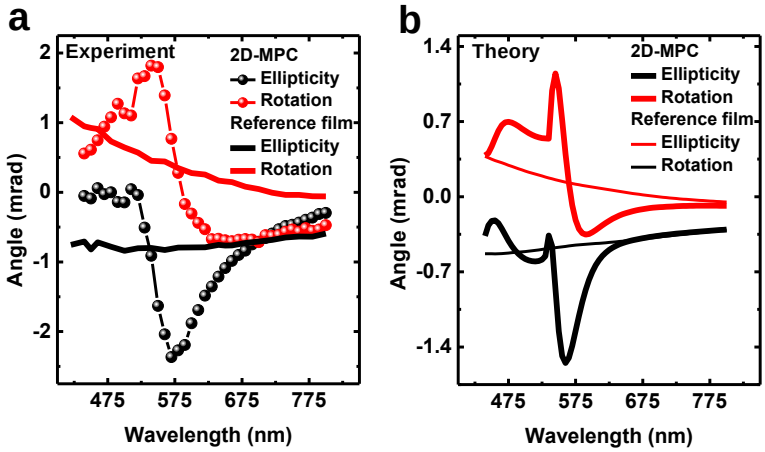

Figure 5.7: Experimental (a) and calculated (b) Kerr ellipticity and rotation for p-polarized light, ϕ = 45° and θ =30°.

The experimental data and the aformentioned conclusions are fully supported by the calculated MOAs spectra, which are shown in Figure 5.8, in the spectral range 250-800 nm, for θ ranging from 0° to 70°, and for ϕ equal to 0° and 45°.

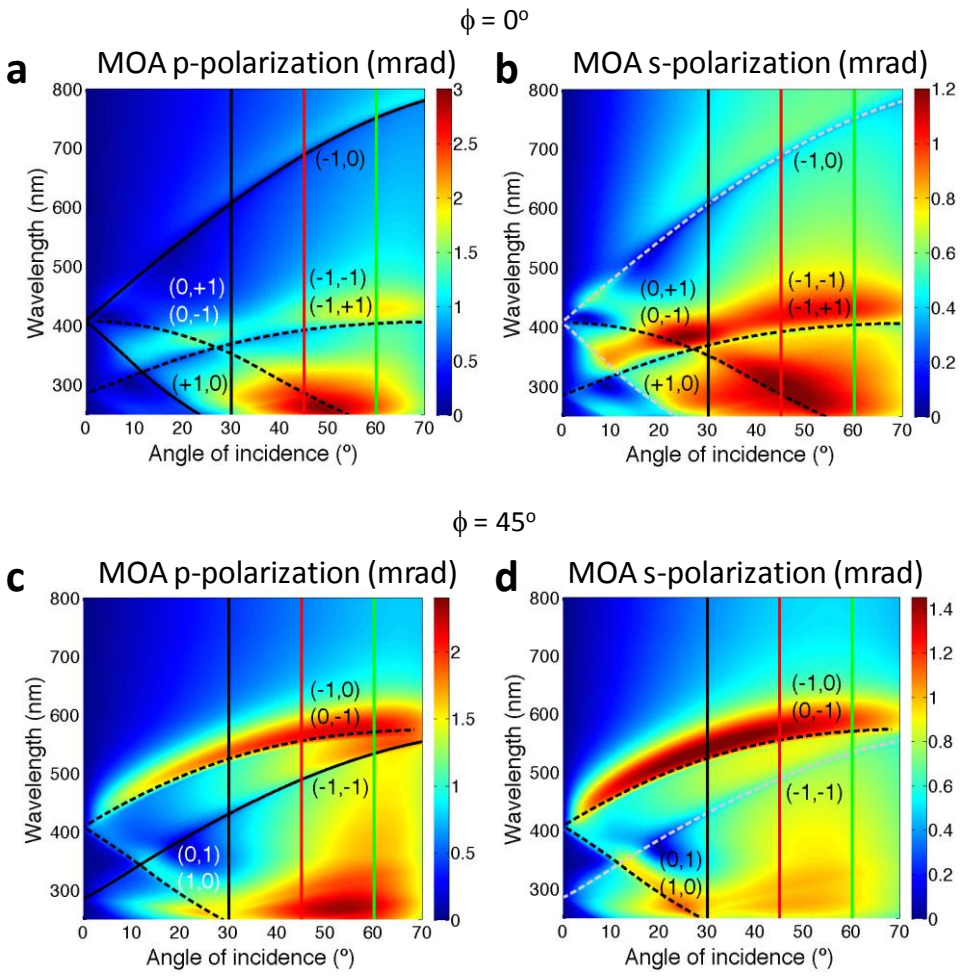

Figure 5.8: Calculated MOA of the 2D-MPC. (a) p-polarized light and ϕ = 0°. (b) s-polarized light and ϕ = 0°. (c) p-polarized light and ϕ = 45°. (d) s-polarized light and ϕ = 45°. The different color (black or white) used for labelling the modes is just for improving their legibility.

For each azimuth angle ϕ, the maps are identical, apart from their slightly different intensity, and clearly show signatures of all the excitable modes independent of the light polarization, proving that the MO coupling enables the activation of modes in the MOA that are forbidden (collinear case) for s-polarization. The difference in the intensities between the MOA with p- and s-polarization is merely due to the higher pure optical reflectivity for s-polarization as compared to p-polarization (compare panels of Figures 5.2 and Figure 5.3).

This is easy to understand from the following definition of the MOA based on Fresnel reflection coefficients, which reads

$$MOA_{S(P)} = |r_{s\to p}(r_{p\to s})|/|r_{ss}(r_{pp})| \tag{5.2}$$

Thus, the fact that $|r_{ss}|$ is larger than $|r_{pp}|$ naturally explains why the MOA for s-polarized light is less intense than that for p-polarized light. Moreover, if we check the spectra of the MO induced polarization conversion coefficients $|r_{s\to p}|$ and $|r_{p\to s}|$for the particular case of $\theta = 45^{o}$ (Figure 5.9), we clearly see that they are *totally* independent of the polarization of the incident light and contain signatures of all the SPP modes excitable in the explored wavelength range for both $\phi = 0°$ (Figure 5.9(a)) and $\phi = 45°$ (Figure 5.9(a)), in complete agreement with the physical picture disclosed above. We now focus on the most interesting result of our study, namely the observed large enhancement of the MOA at $\phi = 45°$ in correspondence of the excitation of the degenerate coupled modes originating from the non-collinear SPP waves (-1,0) and (0,-1).

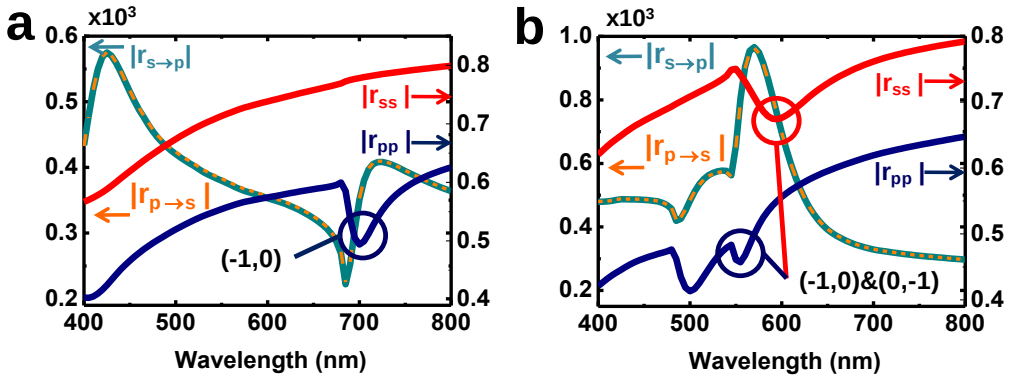

Figure 5.9: Calculated absolute values of the reflection and MO-induced polarization conversion coefficients. (a) $\phi = 0°$ and $\theta = 45°$, with highlighted the collinear mode (-1,0) (blue circle), excitable with p-polarized light only. (b) $\phi = 45°$ and $\theta = 45°$, with highlighted the non-collinear mode (-1,0)/(0,-1) (blue and red circles), excitable with both s- and p-polarized light.

In this special case, these two SPP coupled modes are resonantly excited directly by the incident light and through the MO-induced polarization conversion, for both s- and p-polarized incident light. This simultaneous availability of two resonant channels for coupling the incidence light to SPP modes, both direct and MO-induced coupling, is the key of the observed MOA enhancement. This appears clear when inspecting Figure 5.9(b), which displays the spectra of $|r_{s\to p}|$, $|r_{p\to s}|$, $|r_{ss}|$ and $|r_{pp}|$ at θ = 45°. The MO-induced polarization conversion coefficients are identical, demonstrating once more that the difference of the MOAs intensities for p and s polarizations is due to the pure optical reflectivity intensity difference.

To summarize, the key message emerging from the physical picture disclosed above is that the enhancement of the MOA is possible only when two (or more) channels are available for direct and MO-induced resonant coupling of the incidence light to SPP modes and this is possible only when degenerate and non-collinear SPP coupled modes are involved. These concepts, demonstrated for L-MOKE configuration, are also applicable to the P-MOKE geometry for $\theta \neq 0°$.

5.4 Polarization conversion tuning through plasmonic bands engineering

We envision that the MO-SPP-assisted polarization conversion can be further tuned by making more than two channels available for direct and MO-induced resonant coupling of the incidence light to SPP modes, namely designing the crystal lattice so that plasmonic bands can intersect at desired wavelengths and angles of incidence. As an illustrative example of the opportunities offered by plasmonic band engineering, we calculated using the SMM the MO-induced polarization coefficients of an anisotropic 2D-MPC having a rectangular crystal lattice. The diameter of the holes is the same as for the square lattice studied above. Using a rectangular array with d_x = 400 nm and d_y = 600 nm, and for ϕ = 0°, an intersection between the two non-collinear bands (0, ±1) and (-1, ±1) is produced at $\theta \approx 36°$ and at $\lambda \approx 500$ nm, while a second intersection between the

collinear band (0, -1) and the non-collinear bands (0, ±1) is obtained at $\theta \approx 22°$ and $\lambda \approx$ 575 nm of wavelength (see Figures 5.10(a)).

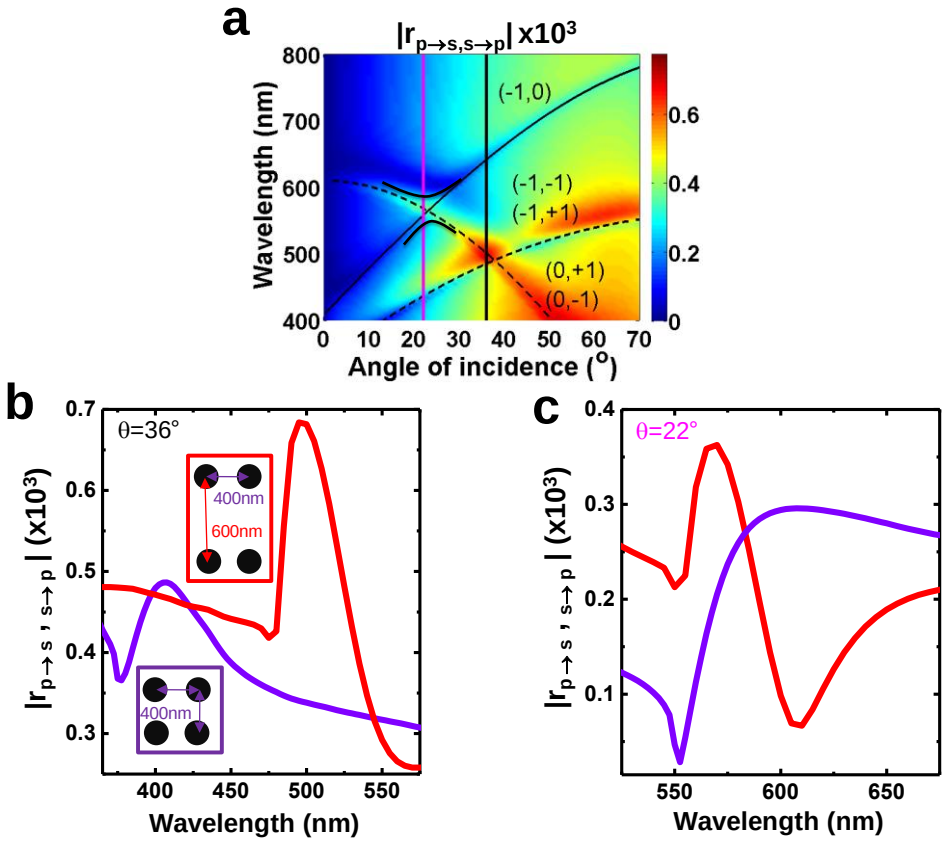

Figure 5.10: (a) Calculated absolute values of $|r_{s\to p,p\to s}|$ for a rectangular 2D-MPC (d_x = 400 nm and d_y = 600 nm) at ϕ = 0°. Vertical lines indicate the angles of incidence 22° (pink line) and 36° (black line). The black thick lines at 22° at the intersection between the bands (0, -1) and (0, ±1) are guiding lines indicating a band gap opening. Calculated absolute values of $|r_{s\to p,p\to s}|$ of rectangular (red solid line) and square (violet solid line) 2D-MPC at ϕ = 0° for θ = 36° (b) and for θ = 22° (c).

In Figure 5.10(b) we show the comparison between the calculated $|r_{s\to p,p\to s}|$ spectra at $\theta \approx 36^{o}$ for the square (violet solid line) and rectangular (red solid line) lattices. In the case of the square 2D-MPC, the peak at $\lambda \approx$ 400 nm corresponds to the enhancement of the

polarization conversion effect due to the resonant excitation of the coupled SPP modes in the (-1,±1) non-collinear bands. The intense peak at $\lambda \approx 500$ nm in the spectrum for the rectangular lattice is now produced by the resonant excitation of coupled SPP modes in the (-1,±1) and (0,±1) non-collinear bands. For the rectangular array, the enhancement of the polarization conversion is about two times that occurring in the square array as a consequence of the fact that now the channels for polarization conversion have been doubled. Therefore, the spectra in Figure 5.10(b) corroborate the physical picture put forward above and demonstrate that through plasmonic band engineering the enhancement of the plasmon-assisted polarization conversion can be further strengthened by making more than two channels available for direct and MO-induced resonant coupling of the incidence light to SPP modes. On the other hand, the spectrum of the calculated $|r_{s\to p,p\to s}|$ for the rectangular lattice that results from the other type of band intersection occurring at $\theta = 22°$ is shown in Figure 5.10(c) (red solid line). Also in this case, the spectrum at the same θ calculated for the square array is displayed (violet solid line) for comparison. For the square lattice, the broad maximum in the spectral range 550-650 nm arises from the resonant excitation of the SPP mode in the collinear band (0, -1). For the rectangular lattice, the broad peak is replaced by a narrower and more intense peak at around 565 nm immediately followed by a dip at around 610 nm, yielding to a sort of symmetric resonant-antiresonant line shape. The effects of the plasmonic bands crossing on the $|r_{s\to p,p\to s}|$ spectral behavior are now completely different with respect to the previous case. Thus, we can conclude that when a plasmonic band crossing is produced, SPP modes interfere constructively when they have the same nature (case for $\theta \approx 36^{o}$) while the interference is changing from constructive to destructive upon varying the wavelength when they are of different nature (case for $\theta \approx 22^{o}$). In this respect, it is worth mentioning that intersection between collinear and non-collinear bands was experimentally observed in non-magnetic rectangular 2D-PC, showing the possibility of inducing interference effects such as band gaps opening with the appearance of peculiar coupled SPP modes with a low group velocity and high radiative damping.[172] Figure 5.10(a) indeed displays that a clear band gap is opened by modes hybridization at the intersection of the two bands (see the black thick lines in Figure 5.10(a)). We speculate here that the suppression of the polarization conversion effect at $\lambda \approx$ 610 nm (minimum

in the red solid curve in Figure 5.10(c)) might be due to the excitation of such coupled SPP modes with a low group velocity and high radiative damping. While further investigations are needed to confirm the origin of such intriguing behavior, on a more practical footing, the calculations clearly show that the coupling of modes of different nature allows a fine tuning of the polarization conversion effects in a sharp spectral region. We finally mention that, in addition to the modification of the lattice parameters, one can also tune the MOA by playing with the holes diameter and shape. The detailed discussion of these effects is out of the scope of this Chapter, but it has been already shown that holes shape and dimensions can be tailored to tune the coupling efficiency between light and SPP modes[189] and, as direct consequence, to further tune the MOA of 2D-MPCs.[178]

5.5 Conclusions

In summary, we have investigated a 2D-MPC with a periodic array of cylindrical holes in a ferromagnetic layer supporting SPPs modes displaying a plasmonic band structure. We have demonstrated that the intrinsic MOA acting in the crystal plane allows an efficient coupling of the light to *all* the excitable surface plasmon polariton modes through the synergistic action between diffracting coupling and MO-induced polarization conversion. This leads to the same MO response *independently* of the incident light polarization. We further demonstrated that a resonant enhancement of the MO response in L-MOKE configuration is induced when two or more channels are available for direct and MO-induced resonant coupling of the incidence light to particular degenerate and *non-collinear* surface plasma polariton modes. The physics disclosed by our findings paves the way for the design of 2D-MPCs with tailored and enhanced magneto-optical response by engineering the plasmonic band structure via lattice design.

6. Conclusions and outlook

In this Thesis we investigated the optical and magneto-optical responses of planar magnetic plasmonic nanostructures supporting both localized and propagating plasmons. The results presented here provide a new insight for the understanding of linear magneto-optical effects in nanostructured materials, opening a path to the design of novel metamaterials with tailored and enhanced magneto-optical activity. The use of the developed design principles for the emerging magnetoplasmonic metasurfaces would deliver to an outstanding control over the polarization state of light and pave the way for novel sensing methodologies. Moreover, we envision that the systems studied in this Thesis offer the unique opportunity to explore other potential synergistic effects arising from peculiar static and dynamic magnetic configurations, such as periodic magnetic domains and spin waves, which can be induced and controlled in this kind of system by an external magnetic field. We speculate that, by proper design of the systems, we might expect to observe a field dependence of the magneto-optical effects. The concept of magnetically tunable resonant interaction effects between localized or propagating plasmons, magnetostatic configurations and dynamic magnetization states, could open new perspectives towards the interplay between the fields of magnonics, spintronics, and plasmonics.[190] Moreover, it is worth mentioning that all the effects disclosed in this Thesis are small for commercial nano-optics applications. The challenge is to find new materials such as ferromagnetic alloys with an improved magneto-optical response and the simultaneous possibility to excite surface plasmons, or to explore novel and more complex 3D architectures where Faraday and Kerr effects can overcome the degree of rotation. This will enable a practical implementation of the design principles developed along the Thesis towards a whole range of future active nano-optic devices. Furthermore, new physics regarding magnetic plasmonic nanostructures has still to be discovered. For instance, if the Voigt constant is comparable with the dielectric function of the material, the theory developed to describe the systems studied in this Thesis will be no more valid. The study of materials with this peculiarity will probably open the door towards not yet observed extraordinary magneto-optical effects and novel non-linear behaviors.

7. List of Publications

Publications discussed in this Thesis

1. N. Maccaferri, L. Bergamini, M. Pancaldi, M. K. Schmidt, M. Kataja, S. van Dijken, N. Zabala, J. Aizpurua, and P. Vavassori "*Anisotropic Nanoantenna-Based Magnetoplasmonic Crystals for Highly Enhanced and Tunable Magneto-Optical Activity"* Nano Letters **16**(4), 2533-2542 (2016) – **Chapter 4**.

2. R. Verre, N. Maccaferri, K. Fleischer, M. Svedendahl, N. O. Länk, A. Dmitriev, P. Vavassori, I.V.Shvets and M. Käll "*Polarization conversion-based sensing scheme using anisotropic plasmonic metasurfaces"* Nanoscale **8**, 10576-10581 (2016) – **Chapter 3**.

3. N. Maccaferri, A. García-Martín, J. C. Cuevas, X. Inchausti, D. Tripathy, A. Adeyeye, and P. Vavassori* "*Resonant enhancement of magneto-optical activity induced by surface plasmon polariton modes in 2D magnetoplasmonic crystals"* ACS Photonics **2**(12), 1769-1779 (2015) – **Chapter 5**.

4. N. Maccaferri, K. E. Gregorczyk, T. V. A. G. De Oliveira, M. Kataja, S. van Dijken, Z. Pirzadeh, A. Dmitriev, J. Åkerman, M. Knez, and P. Vavassori *"Ultrasensitive and label-free molecular level detection enabled by light phase control in magnetoplasmonic nanoantennas"*Nature Communications **6**, 6150 (2015) – **Chapter 3**.

5. K. Lodewijks, N. Maccaferri, T. Pakizeh, R. Dumas, I. Zubritskaya, J. Åkerman, P. Vavassori, and A. Dmitriev* "*Magnetoplasmonic design rules for active magneto-optics"* Nano Letters **14**(12), 7207-7214 (2014) – **Chapter 2**.

6. N. Maccaferri, A. Berger, S. Bonetti, V. Bonanni, M. Kataja, Qi Hang Qin, S. van Dijken, Z. Pirzadeh, A. Dmitriev, J. Nogués, J. Åkerman, and P. Vavassori "*Tuning the magneto-optical response of nanosize ferromagnetic Ni disks using the phase of localized plasmons"* Physical Review Letters **111**(16), 167401 (2013) – **Chapter 2**.

Other publications

7. M. Kataja, S. Pourjamal, **N. Maccaferri**, P. Vavassori, T. K. Hakala, M. J. Huttunen, P. Törmä, and S. van Dijken* "*Hybrid plasmonic lattices with tunable magneto-optical activity"* Optics Express **24**(4), 3652-3662 (2016).

8. Zubritskaya*, K. Lodewijks, **N. Maccaferri***, A. Mekonnen, R. Dumas, J. Åkerman, P. Vavassori, and A. Dmitriev* "*Active magnetoplasmonic ruler"* Nano Letters **15**(5), 3207-3211 (2015).

9. **N. Maccaferri**, M. Kataja, V. Bonanni, S. Bonetti, , Z. Pirzadeh, A. Dmitriev, S. van Dijken, J. Åkerman, and P. Vavassori* "*Effects of a non-absorbing substrate on magneto-optical Kerr response of plasmonic ferromagnetic nanodisks"* Physica Status Solidi (A), **211**(5), 1067-1075 (2014).

10. **N. Maccaferri***, J. B. González-Díaz, S. Bonetti, A. Berger, M. Kataja, S. van Dijken, J. Nogués, V. Bonanni, Z. Pirzadeh, A. Dmitriev, J. Åkerman, and P. Vavassori* "*Polarizability and magnetoplasmonic properties of magnetic generalized nanoellipsoids"* Optics Express **21**(8), 9875-9889 (2013).

Appendix A (experimental methods)

A1 Optical and magneto-optical characterization

A1.1 Optical measurements

The transmission spectra $(I_0 - I_t)/I_0$, where I_0 and I_t are the intensities of the incident and transmitted light, respectively, were taken in the wavelength range 400-2000 nm (in many figures in the Thesis the entire range is not shown). The intensity of the light passing through the substrate without nanostructures on top was taken as reference signal I_0. The reflectivity spectra $(I_0 - I_r)/I_0$, where I_0 and I_r are the intensities of the incident and reflected light, respectively, were measured using a goniometric spectrometer which allows to vary both the angle of incidence and the azimuthal angle. The intensity of the light going directly to the detector was taken as the reference signal I_0. Sketch of the two set-ups used are shown in Figure A1(a),(b). All the measurements were performed using spectrometers made by StellarWiz® or Ocean Optics®.

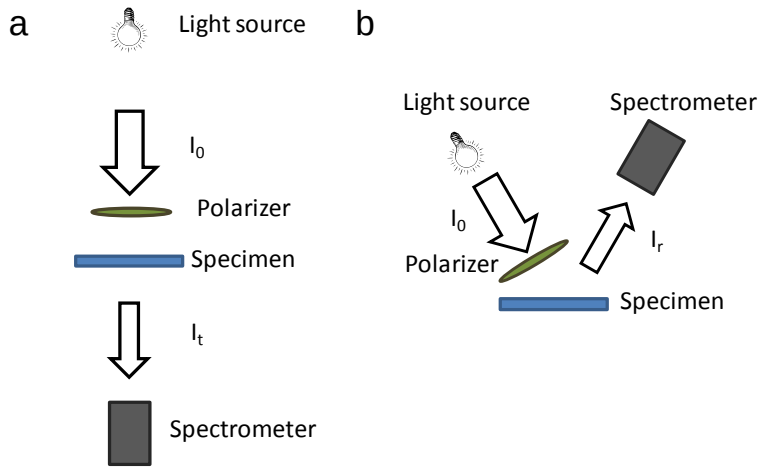

Figure A1: (a) Transmission geometry. (b) Reflection geometry.

A1.2 Magneto-optical measurements

The wavelength dependence of the magneto-optically induced θ_K and ε_K (rotation and ellipticity polarization angles) of the reflected/transmitted light, which define the magneto-optical activity $\sqrt{\theta_K^2 + \varepsilon_K^2}$, were measured using magneto-optical Kerr/Faraday effects spectrometers working in longitudinal (only Kerr effect) or polar geometry in the wavelength range 400-1100 nm. A broadband super-continuum light source (Fianium® or NKT®) is coupled via a multimode optical fiber to an acousto-optic tunable filter (AO filter) to get monochromatic light in the wavelengths range 400-1100 nm, with a resolution of 1 nm. The light beam is linearly polarized (p- or s-polarization state) passing through a Glann-Thompson polarizer and then is focused on to the sample surface and perpendicular to it via a lens with a 500 mm focal length. The sample is placed in the gap of an electromagnet. θ_K and ε_K are measured by switching the polarity of the magnetic field applied parallel (L-MOKE) or perpendicular (P-MOKE) to the sample plane. The transmitted/reflected light is then collected by a lens with equal focal length as the focusing one and directed to the detection system. θ_K and ε_K are measured at each wavelength with the reflected/transmitted beam passing through a photo-elastic phase modulator (PEM) that operates at a frequency $\omega =$ 50kHz and introduces a fixed retardation between p- and s-polarized light. Subsequently the light passes through a second polarizer (called analyzer) oriented at 5 degrees from extinction, viz., with its polarization axis at 85 degrees from that of the first polarizer. The reflected/transmitted signal is recorded by a Si (for VIS wavelengths) and InGaAs (for NIR wavelengths) photodetectors. The signal is determined by filtering out the ω component of the photedector signal using a lock-in amplifiers at 50kHz (1f) and 100kHz (2f), using the reference signal from the PEM. Both of the lock-in signals are normalized by the reflected/transmitted DC signal in order to obtain the Kerr ellipticity and rotation which are proportional to the 1f and 2f signals respectively. This technique is called polarization modulation technique.[191]

A1.2.1 Polarization measurements in sensing experiments

As shown schematically in Figure A2, $\Delta\varepsilon$ was measured at each wavelength with the transmitted (reflected geometry not shown) beam passing through a PEM and a polarizer before detection. $\Delta\varepsilon(\lambda) = \varepsilon(H) - \varepsilon(-H)$ of the transmitted or reflected light was measured using magneto-optical Faraday (incidence angle 0°) and Kerr (incidence angle 2.5°) effect spectrometers working in polar geometry in the wavelength range 400-2000 nm. $\Delta\varepsilon$ was measured by switching back and forth the saturating field $|\boldsymbol{H}|$ = 4 kOe applied normal to the sample plane. A lock-in amplifier was used to filter the signal at the modulation frequency in order to retrieve $\Delta\varepsilon$. The rotation of light polarization θ induced by the plasmonic dimers was measured using the same setup, but in this case without applying the magnetic field. For microscope measurements, a long working distance 100X Nikon objective was inserted in the light path before the sample.

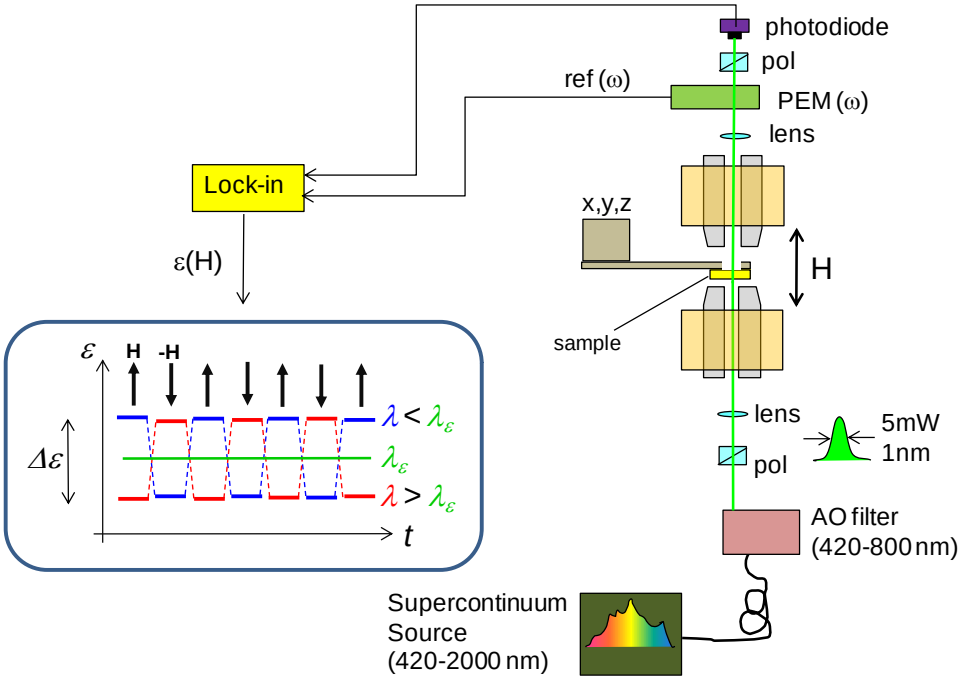

Figure A2: Schematic of the experimental setup utilized for sensing experiments.

A2 Sensing experiments

A2.1 Bulk refractive index experiments

Bulk sensitivity experiments were performed in a microfluidic cell where different liquids, with different refractive index, were injected every time. We used liquids and mixtures whose refractive indexes are well known, viz. water (n=1.33), glycerol (n=1.47) and *X*% glycerol volume in water ($0<X<50$).

A2.2 Surface sensitivity with Ni nanoantennas

For surface sensitivity assessment, molecular layer deposition (MLD) of polyamide 6.6 (PA-6.6) was done in a commercially available Cambridge Nanotech/Ultratech Savannah system using alternating pulses of adipoyl chloride (AC) (Sigma Aldrich) and 1,6-hexamethylenediamine (HD) (Sigma Aldrich) with the following pulse/purge/pulse/purge parameters; 0.5s/30s/0.5s/30s. The AC and HD were heated to 70°C and 80°C respectively. The reaction chamber was maintained at 85°C throughout the reaction. Before deposition the samples were treated using 5 min cycles of acetone and isopropanol ultrasonication, and then exposed to Ar plasma at 90 W for 60 sec to eliminate residues of organic materials. Coating and cleaning procedures were repeated several times to ensure the reproducibility of the experiment (both polarization and thickness of PA-6.6 deposits). Schematic of one cycle of the MLD process for PA-6.6 is shown in Figure A3. The thickness of the PA-6.6 deposits was monitored via AFM. The AFM measurements were done in the same region after each MLD cycles and MOKE measurement step, using an Agilent® 5500 AFM microscope with a Si tip operated in tapping mode. The images were analyzed using the Gwyddion® software package in order to extract the average thickness values of PA-6.6 deposits.

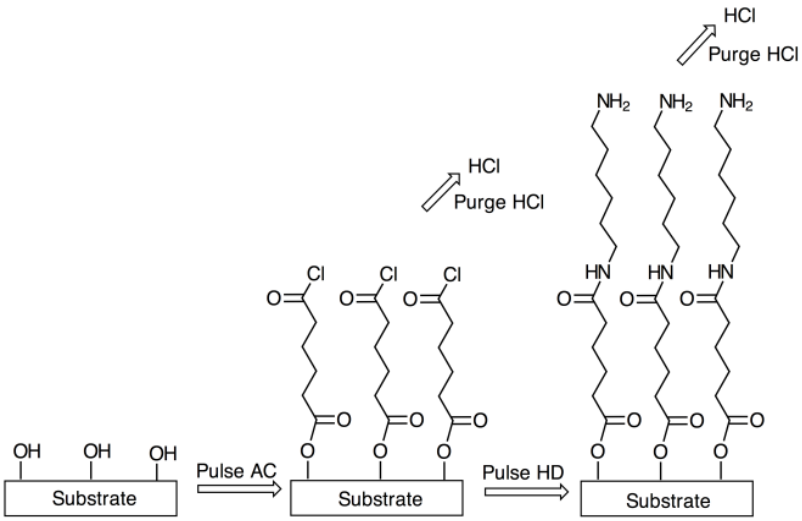

Figure A3: One cycle of the MLD process for PA-6.6. A substrate with –OH surface groups is exposed to a pulse of AC. The AC reacts with these –OH groups creating the by-product HCl, which is purged away along with any unreacted AC. Next, a pulse of HD is introduced to the reaction chamber and reacts with the available –Cl groups. Again, the by-product is HCl, which is purged away along with any unreacted HD. This process is repeated until the desired thickness is achieved. Nominally, the process has a growth rate of ~ 0.8 nm per cycle.

A2.3 Surface functionalization of gold dimers

Prior to the sensing experiments, the samples were cleaned in a basic piranha solution (H_2O: H_2O:H_2O in a ratio of 6:1:1) at 80°C for 10 minutes and rinsed in deionized water before loading the sample in a flow cell. Biotylinated bovin serum albumin (bBSA, Sigma Aldrich) with a concentration of 100ug/mL was diluted in a phosphate buffer solution (~0.01mol/L), it was first adsorbed on the surface, and, after rinsing, neutravidin (~60 kD) was diluted in another phosphate buffer solution and injected in the microfluidic cell.

A3 Fabrication processes

A3.1 Hole mask colloidal lithography

A sketch of the hole-mask colloidal lithography[192] (HMCL) fabrication scheme is reported in Figure A4.

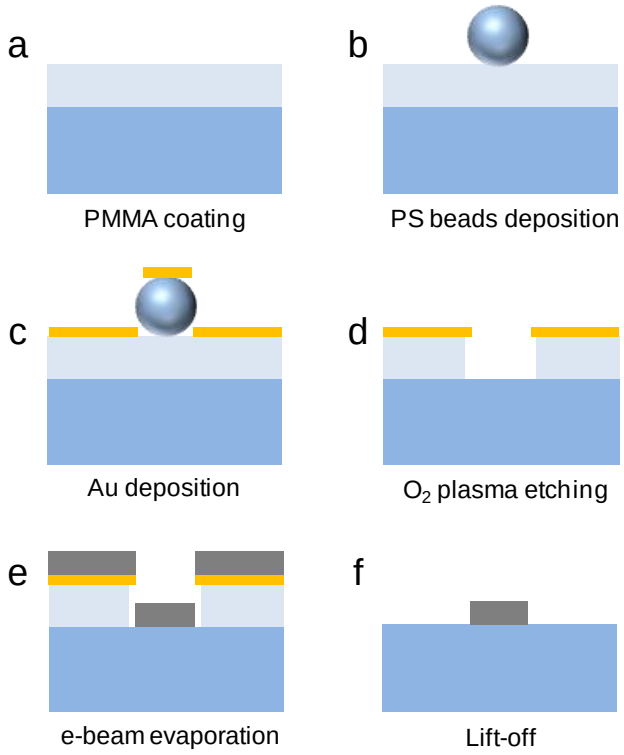

Figure A4: (a) Deposition of sacrificial PMMA layer. (b) Deposition of polystyrene spheres in an arbitrarily distributed arrangement. (c) Evaporation of oxygen plasma resistant Au-mask. (d) Removing polystyrene spheres with ultrasonic bath and subsequent isotropic dry etching leads to extended holes in PMMA layer. (e) Evaporation of the structures. (f) Lift-off of the sacrificial PMMA layer.

The substrates used are 10x10x1 mm^3 pieces of microscope slide glass (VWR International). The glass substrates were first cleaned through 5 min cycles of Acetone, Isopropanol (IPA) and water ultrasonication. A polymethyl methacrylate (PMMA) A4

film (2 wt % PMMA diluted in anisole, MW = 950000) was spin coated on the clean glass surface at 3000 rpm and annealed in an oven furnace at 180°C for 10 minutes. Reactive O_2 plasma treatment (50 W, 5 s, 250 mTorr, Plasma Therm Batchtop RIE 95m) was applied in order to decrease the polymer film hydrophobicity and avoid spontaneous de-wetting of the surface, which would introduce inhomogenities in the particles distribution. Providing a net charge to the PMMA surface by dispersing for 30 s a solution containing a positively charged polyelectrolyte onto the film (polydiallyldimethylammonium (PDDA) MW 200000–350000, Sigma Aldrich, 0.2 wt % in Milli-Q water, Millipore), followed by careful rinsing with de-ionized water for 10 s in order to remove excess PDDA and blow-drying with a N_2 stream. Deposition of a water suspension containing negatively charged polystyrene (PS) particles (sulfate latex, Invitrogen, 0.2 wt % in Mili-Q water) for 45 s, and N_2 drying in a similar fashion as described above, leaving the PMMA surface covered with uniformly distributed PS-spheres. Evaporation of an oxygen plasma resistant thin film of Au or Cr (10nm) at perpendicular/45° incidence, resulting in a shadow mask with round/elliptical holes (to obtain circular/elliptical disks, respectively; the angle can be modified to increase or decrease the aspect ratio of the elliptical disks). Removing the PS-spheres using tape stripping (SWT-10 tape, Nitto Scandinavia AB), resulting in a mask with holes arranged in a pattern determined by the self-assembled colloidal particles. O_2 plasma treatment (50 W, 250 mTorr, Plasma Therm Batchtop RIE 95m), to remove all PMMA situated underneath the holes in the film, leaving the surface covered with a thin film mask supported on a perforated, undercut polymer film. Ni and Au deposition is done by electron beam (e-beam) assisted evaporation. For the Au dimers a seed layer of Cr (1nm) was first deposited at both positive and negative angles of incidence of ϕ = 13.5°. Afterwards, Au dimers of a total thickness of 40 nm each were deposited by evaporating at both positive and negative angles of incidence ϕ = 13.5° and lift-off in acetone was performed. As the deposition would induce also a shrinking of the mask due to side deposition, positive and negative deposition were alternated every 5nm. Lift off was done using acetone at room temperature or 50 °C for 5–10 min. The filling factor can be varied between 5% and 30% in a controlled manner.

A3.2 Electron beam lithography

The samples have been fabricated by EBL and lift-off procedure. As first step, a 5 nm thick Ti layer has been e-beam evaporated (evaporation rate: 0.3 Å/s) onto a cleaned Pyrex substrate, both as an adhesion layer for the final Ni evaporation and as a metallic coating for avoiding charging effects during e-beam lithography. Subsequently, a positive resist (ZEP520A-7) has been spin-coated onto the substrates at 2500 rpm for 60 s. The resist has been exposed by a 20 KV electron beam inside a RAITH150 Two system. Exposition time has been adjusted according to the dot size. After developing the exposed resist (with ZED-N50 developer), a 30 nm thick Ni layer has been e-beam evaporated (evaporation rate: 0.4Å/s). Finally, the lift-off has been carried out by dipping the samples in the proper solvent (ZDMAC).

A3.3 Phase-shift mask lithography

Large-area (4 mm x 4 mm) antidot structures were fabricated on commercially available Si substrates using deep ultraviolet lithography at 248 nm exposing wavelength, followed by e-beam evaporation and lift-off processes. To create patterns in the resist, the substrate was coated with a 60 nm thick anti-reflective layer followed by a 480 nm positive deep UV photoresist, which is four to five times thicker than those used typically in e-beam lithography (EBL). This allows one to fabricate antidots with high aspect ratio and makes the lift-off process easier. A Nikon lithographic scanner with KrF excimer laser radiation was used to expose the resist. To convert the resist patterns into antidots, 30 nm thick was deposited using the e-beam evaporation technique at a rate of 0.02 nm s^{-1}. The pressure was maintained at about 2×10^{-6} torr at during the deposition at room temperature. Lift-off processing of the deposited film was carried out in isopropyl alcohol. More details of the processing steps can be found elsewhere.[186]

Appendix B (theoretical methods)

B1 Polarizability of a general ellipsoid

A numerical implementation of the Meier and Wokaun Long Wavelength Approximation (MWLWA) is introduced.[67, 68, 193] We extend this model to the general ellipsoidal shape including also the optical anisotropy effects arising from the magneto-optical properties of a ferromagnetic material. This simple and fast method allows us to calculate the far-field optical and MO spectral responses of an ensemble of non-interacting ferromagnetic nanoparticles embedded in an arbitrary medium, which can be also magnetic. For the calculation of the far-field optical and MO spectral responses we first employ the polarizability of a single nanoparticle computed with our approach in a standard effective medium approximation (EMA)[96, 194, 195], used to model the ensemble of ferromagnetic ellipsoidal particles embedded in a medium as an effective composite film. Then we apply the Transfer Matrix Method (TMM)[99, 100, 101], for the calculation of the optical and magneto-optical far-field responses of multi-layered systems.

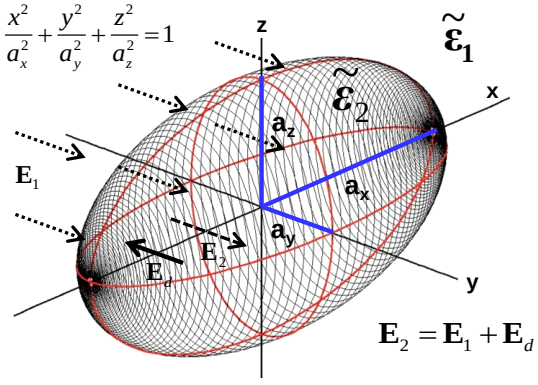

Figure B1: Scheme of a general ellipsoid embedded in a host medium. The ellipsoid is under the influence of an acting field $\mathbf{E}_1$, and due to the induced dipole moments, the electric field $\mathbf{E}_2$ inside itchanges.

To obtain the polarizability tensor $\tilde{\tilde{\alpha}}$ of a general ellipsoidal magnetic nanoparticle with semi-axes a_x, a_y, and a_z (see Figure B1), let's consider the particle embedded in a non-magnetic host medium described by a diagonal dielectric tensor $\tilde{\varepsilon}_1 = \varepsilon_1 \tilde{I}$, where $\tilde{I}$ is the identity matrix. Given the magnetic character of the nanoparticle, its dielectric tensor, in the presence of an external magnetic field high enough to saturate the particle, presents non-diagonal components. Including terms which are of first order in $\widehat{\boldsymbol{m}} = (m_x \hat{\boldsymbol{x}} + m_y \hat{\boldsymbol{y}} + m_z \hat{\boldsymbol{z}})$, the unit magnetization vector expressed in terms of the Euler's angles director cosines, it can be represented, for a material having cubic symmetry, by a non-diagonal, anti-symmetric, tensor $\tilde{\varepsilon}_2$[196]

$$\tilde{\varepsilon}_2 = \begin{pmatrix} \varepsilon_2 & -iQ\varepsilon_2 m_z & iQ\varepsilon_2 m_y \\ iQ\varepsilon_2 m_z & \varepsilon_2 & -iQ\varepsilon_2 m_x \\ -iQ\varepsilon_2 m_y & iQ\varepsilon_2 m_x & \varepsilon_2 \end{pmatrix}$$

where Q is the Voigt magneto-optical constant. Let's consider an incident plane electromagnetic wave $\boldsymbol{E}(\boldsymbol{r}, t) = \boldsymbol{E}_1 e^{[i(\boldsymbol{k}\cdot\boldsymbol{r} - \omega t)]}$ impinging on the particle. Following Refs. [96, 193], we initially neglect the space variation of $\boldsymbol{E}(\boldsymbol{r}, t)$ over the nanoparticle volume, viz., $\boldsymbol{E} = \boldsymbol{E}_1 e^{-i\omega t}$. Under this assumption and through the weak Eshelby conjecture, the internal field $\boldsymbol{E}_2$ and therefore the induced polarization **P** can be assumed uniform over the volume of a particle of ellipsoidal shape.[63] Following Bragg and Pippard[197] we can write

$$\mathbf{P} = \varepsilon_0(\tilde{\varepsilon}_2 - \tilde{\varepsilon}_1)V\boldsymbol{E}_2 = \varepsilon_0 V(\tilde{\varepsilon}_2 - \tilde{\varepsilon}_1)(\boldsymbol{E}_1 + \boldsymbol{E}_d) = \varepsilon_0 \tilde{\tilde{\alpha}}\, \boldsymbol{E}_1 \qquad \text{(B1)}$$

where the polarizability $\tilde{\tilde{\alpha}}$ can be obtained once the depolarization field $\boldsymbol{E}_d$ is determined. Strictly speaking, Eq. (B1) is valid only for very small ellipsoidal particles, for which the external field can be assumed uniform. According to Meier and Wokaun [193], using Eq. (B1) the finite size of the particle can be approximately accounted for in the calculation of $\boldsymbol{E}_d$. This is done by assigning a dipole moment $d\boldsymbol{p} = \boldsymbol{P}dV(\boldsymbol{r})$ to each volume element

dV and calculating the retarded depolarization field $d\boldsymbol{E}_d$ generated by $d\boldsymbol{p}$, in the center of the ellipsoid. At this point one should consider also the phase difference due to the incoming light hitting a finite size body. There are several ways to account for this phase difference reported in literature.[67, 198, 199] Although, we verified that inclusion of these corrections have negligible effects, and therefore for sake of clarity we neglect them. We point out, in addition, that for the particular geometry used in our experiments, namely perpendicular incidence over flat disks, this phase difference effects are rigorously zero. Passing in spherical coordinates and integrating over all the particle volume we obtain the following expression

$$\boldsymbol{E}_d = \int d\boldsymbol{E}_d = \int \left(\frac{3\hat{\boldsymbol{u}}(\boldsymbol{P}\cdot\hat{\boldsymbol{u}}) - \boldsymbol{P}}{r^3} + i\frac{2\boldsymbol{P}}{3}k^3 + \frac{\hat{\boldsymbol{u}}(\boldsymbol{P}\cdot\hat{\boldsymbol{u}})}{2r}k^2 \right) dV \qquad \text{(B2)}$$

being k the light wave vector modulus, r the distance from the center of the ellipsoid, and $\hat{\boldsymbol{u}}$ a unit vector in the direction of $\boldsymbol{r}$. The depolarization field $\boldsymbol{E}_d$ in the center of the ellipsoid given by Eq. (B2) is assumed to be the average depolarization field inside the particle. The first term in the integral in Eq. (B2) corresponds to the static depolarization due to a uniform $\boldsymbol{E}_1$ and accounts for the shape of the nanoparticle. The second term is the radiative reaction due to the recoil force, known also as the Abraham–Lorentz force, acting on an oscillating dipole emitting electromagnetic radiation.[193] The integration of this term is straightforward and yields to $(i(2/3)k^3r^3\boldsymbol{P})$. The third term is the so called dynamic depolarization and arises from de-phasing of the radiation emitted by different points in the ellipsoid. This term is considered negligible, and therefore normally discarded, for particles size in the Rayleigh regime ($r << \lambda$, where r is the radius or any semi-axis of the particle).. The inclusion of this term complicates substantially the calculation of the integral in Eq. (B2). It can be shown that Eq. (B2) can be cast in the following, most convenient, tensorial form by factorizing out the polarization density $\boldsymbol{P}$

$$\boldsymbol{E}_d = -(\varepsilon_0\tilde{\varepsilon}_1)^{-1}\left(\tilde{L} - i\frac{k^3V}{6\pi}\tilde{I} - \frac{k^2V}{4\pi}\tilde{D}\right)\cdot\boldsymbol{P} \qquad \text{(B3)}$$

where $\tilde{L} = diag(\mathrm{L}_x, \mathrm{L}_y, \mathrm{L}_z)$ and $\widetilde{D} = diag(\mathrm{D}_x/a_x, \mathrm{D}_y/a_y, \mathrm{D}_z/a_z)$ are the static and dynamic geometrical tensors, and $V = (4\pi/3)a_x a_y a_z$ is the particle volume. The static tensor has been calculated in previous works.[64, 200, 201] As stated above, this tensor is related to the shape of the ellipsoids with semi-axes a_x,a_y, and a_z, and its elements can be calculated as follows[89]

$$L_{ii} = \frac{a_i a_j a_k}{2} \int_0^\infty \left(q + a_i^2\right)^{-\frac{3}{2}} \left(q + a_j^2\right)^{-\frac{1}{2}} \left(q + a_k^2\right)^{-\frac{1}{2}} dq \qquad \text{(B4)}$$

where $i = x, y, z$ and $j, k \neq i$, and $L_{ij} = 0$ if $i \neq j$. The integrals in Eq. (B4) have to be computed numerically for general magnetic ellipsoids. The second term in the expression of $\boldsymbol{E}_d$, the radiative reaction tensor $(i/6\pi)k^3 V\tilde{I}$, within the MWLWA model, is determined only by the time variation of the electric field and is simply proportional to the volume V of the particle. The third term is the most complicated to calculate and its explicit expression has been derived only for the particular cases of a sphere[67] as well as of prolate and oblate spheroids[198], since only in these cases it admit an analytical solution. In the more general case treated here, the diagonal elements of this tensor have to be calculated numerically. In order to facilitate the implementation of such calculations, we devised their expressions in cylindrical coordinates

$$D_x = \frac{3a_x}{4\pi} \int_0^1 dz' \int_0^{2\pi} d\theta \int_0^{\sqrt{1-z'^2}} \frac{\rho^2\left(2a_x^2 cos^2\theta + a_y^2 sin^2\theta\right) + a_z^2 z'^2}{\left[\rho^2\left(a_x^2 cos^2\theta + a_y^2 sin^2\theta\right) + a_z^2 z'^2\right]^{\frac{3}{2}}} \rho d\rho \qquad \text{(B5a)}$$

$$D_y = \frac{3a_y}{4\pi} \int_0^1 dz' \int_0^{2\pi} d\theta \int_0^{\sqrt{1-z'^2}} \frac{\rho^2\left(a_x^2 cos^2\theta + 2a_y^2 sin^2\theta\right) + a_z^2 z'^2}{\left[\rho^2\left(a_x^2 cos^2\theta + a_y^2 sin^2\theta\right) + a_z^2 z'^2\right]^{\frac{3}{2}}} \rho d\rho \qquad \text{(B5b)}$$

$$D_z = \frac{3a_z}{4\pi} \int_0^1 dz' \int_0^{2\pi} d\theta \int_0^{\sqrt{1-z'^2}} \frac{\rho^2\left(a_x^2 cos^2\theta + a_y^2 sin^2\theta\right) + 2a_z^2 z'^2}{\left[\rho^2\left(a_x^2 cos^2\theta + a_y^2 sin^2\theta\right) + a_z^2 z'^2\right]^{\frac{3}{2}}} \rho d\rho \qquad \text{(B5c)}$$

The integrals in Eqs. (B4) and (B5) have to be computed numerically for general magnetic ellipsoids. Once the depolarization field $\mathbf{E}_d$ is calculated including the static, dynamic and radiative corrections, it is straightforward to obtain the polarizability of a nano-particle from Eq. (B1):

$$\tilde{\tilde{\alpha}} = V\tilde{\varepsilon}_1(\tilde{\varepsilon}_2 - \tilde{\varepsilon}_1)\left[\tilde{\varepsilon}_1\tilde{I} + \left(\tilde{L} - \frac{k^2V}{4\pi}\tilde{D} - i\frac{k^3V}{6\pi}\tilde{I}\right)(\tilde{\varepsilon}_2 - \tilde{\varepsilon}_1)\right]^{-1} \quad \text{(B6)}$$

In this form, Eq. (B6) can be applied also to calculate the MO response of a general ellipsoidal magnetic particle by using the appropriate anti-symmetric tensor $\tilde{\varepsilon}_2$. Since we aim at comparing the predictions of our approach with experiments preformed on samples where the nanoparticles are distributed with a low concentration over a glass substrate, we selected the Maxwell-Garnett Effective Medium Approximation (EMA) approach for such a calculation. This approach models the nanoparticles in the embedding medium, a mix of air and glass in our case, as a homogeneous film described by an effective dielectric tensor. This approximation is known to provide an accurate description of the reflected field if the nanoparticles are small and do not interact among them. The formalism to obtain such effective dielectric tensor of a magneto-optically active system follows that developed by M. Abe and T. Suwa[202, 203] and is based on the earliest works of Stroud and co-workers.[96, 194, 195] In the case of non-spheroidal elements, we furthermore consider the particles all oriented in the same spatial direction, as they actually are in our samples. Then following Ref. [203] and using Eq. (B6), the relative effective dielectric constant is obtained as

$$\tilde{\varepsilon}_{eff} = \tilde{\varepsilon}_1 + f\tilde{\varepsilon}_1(\tilde{\varepsilon}_2 - \tilde{\varepsilon}_1)\left[\tilde{\varepsilon}_1\tilde{I} + (1-f)\left(\tilde{L} - \frac{k^2V}{4\pi}\tilde{D} - i\frac{k^3V}{6\pi}\tilde{I}\right)(\tilde{\varepsilon}_2 - \tilde{\varepsilon}_1)\right]^{-1} \quad \text{(B7)}$$

The last step is to add the glass under-layer and compute the far-field magneto-optical response of the obtained by-layers system using the TMM[99, 100, 101], which can generate the reflection and transmission matrices for an arbitrary multilayered system.

B2 Analytical expression for MOKE in elliptical nanodisks

We look at an incident p-polarized wave that hits the sample surface at an incident angle with respect to the surface normal. The wave is incident in the *xz*-plane with an electric field $\vec{E}$ as depicted in the sketches in Table B1. The electric field can be decomposed into an *x*- and a *z*-component:

$$E_x = cos\gamma E \tag{B8}$$

$$E_z = sin\gamma E \tag{B9}$$

Additional $cos\gamma$ and $sin\gamma$ terms appear in the expressions of the Kerr signals to include the far-field radiation direction of the different plasmonic modes in p_x and p_z respectively.

	L-MOKE	P-MOKE	T-MOKE
Geometries	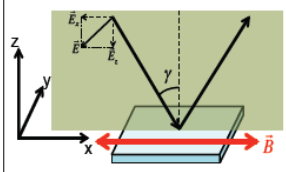	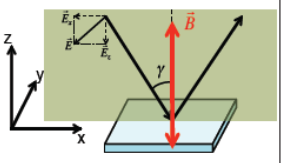	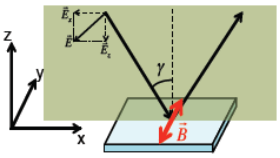
Polarizabilities	$p_x = \alpha_{xx}E_x$ $p_y = \alpha_{yz}E_z$ $p_y = \alpha_{so}\alpha_{yy}\alpha_{zz}E_z$ $p_z = \alpha_{zz}E_z$	$p_x = \alpha_{xx}E_x$ $p_y = \alpha_{yx}E_x$ $p_y = \alpha_{so}\alpha_{yy}\alpha_{xx}E_x$ $p_z = \alpha_{zz}E_z$	$p_x = \alpha_{xx}E_x + \alpha_{xz}E_z$ $p_x = \alpha_{xx}E_x + \alpha_{so}\alpha_{xx}\alpha_{zz}E_z$ $p_y = 0$ $p_z = \alpha_{zz}E_z + \alpha_{zx}E_x$ $p_z = \alpha_{zz}E_z + \alpha_{so}\alpha_{zz}\alpha_{xx}E_x$
Kerr signal	$\propto \frac{p_y}{p_x cos\gamma + p_z sin\gamma}$ $\propto \frac{\alpha_{so}\alpha_{yy}\alpha_{zz}E_z}{cos\gamma\alpha_{xx}E_x + sin\gamma\alpha_{zz}E_z}$ $\propto \frac{\alpha_{so}\alpha_{yy}\alpha_{zz}\sin\gamma E}{\alpha_{xx}\cos^2\gamma E + \alpha_{zz}\sin^2\gamma E}$ $\propto \frac{\alpha_{so}\alpha_{yy}\alpha_{zz}\sin\gamma}{\alpha_{xx}\cos^2\gamma + \alpha_{zz}\sin^2\gamma}$	$\propto \frac{p_y}{p_x cos\gamma + p_z sin\gamma}$ $\propto \frac{\alpha_{so}\alpha_{yy}\alpha_{xx}E_x}{cos\gamma\alpha_{xx}E_x + sin\gamma\alpha_{zz}E_z}$ $\propto \frac{\alpha_{so}\alpha_{yy}\alpha_{xx}\cos\gamma E}{\alpha_{xx}\cos^2\gamma E + \alpha_{zz}\sin^2\gamma E}$ $\propto \frac{\alpha_{so}\alpha_{yy}\alpha_{xx}\cos\gamma}{\alpha_{xx}\cos^2\gamma + \alpha_{zz}\sin^2\gamma}$	$\propto \frac{p_z sin\gamma}{p_x cos\gamma}$ $\propto \frac{sin\gamma(\alpha_{zz}E_z + \alpha_{so}\alpha_{zz}\alpha_{xx}E_x)}{cos\gamma(\alpha_{xx}E_x + \alpha_{so}\alpha_{xx}\alpha_{zz}E_z)}$ $\propto \frac{\alpha_{zz}\sin^2\gamma E + \alpha_{so}\alpha_{zz}\alpha_{xx}\sin\gamma\cos\gamma E}{\alpha_{xx}\cos^2\gamma E + \alpha_{so}\alpha_{xx}\alpha_{zz}\sin\gamma\cos\gamma E}$ $\propto \frac{\alpha_{zz}}{\alpha_{xx}}\tan\gamma\frac{\tan\gamma + \alpha_{so}\alpha_{xx}}{1 + \alpha_{so}\alpha_{zz}\tan\gamma}$

Table B1: Analytical formulas for all the MOKE geometries when the incident light is p-polarized.

We look then at an incident s-polarized wave that hits the sample surface at an incident angle with respect to the surface normal. The wave is incident in the *xz*-plane with an electric field $\vec{E}$ as depicted in the sketches in Table B2. The electric feld only has an in-plane component along the *y*-axis.

	L-MOKE	P-MOKE	T-MOKE
Geometries	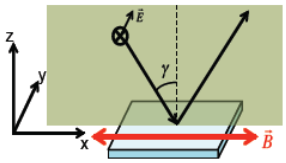	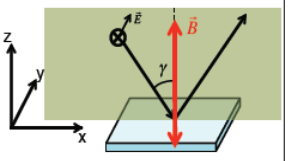	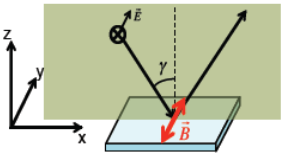
Polarizabilities	$p_x = 0$ $p_y = \alpha_{yy}E$ $p_z = \alpha_{zy}E$ $p_z = \alpha_{so}\alpha_{zz}\alpha_{yy}E$	$p_x = \alpha_{xy}E$ $p_x = \alpha_{so}\alpha_{xx}\alpha_{yy}E$ $p_y = \alpha_{yy}E$ $p_z = 0$	$p_x = 0$ $p_y = \alpha_{yy}E$ $p_z = 0$
Kerr signal	$\propto \frac{p_x \sin\gamma}{p_y}$ $\propto \frac{\alpha_{so}\alpha_{zz}\alpha_{yy}E\sin\gamma}{\alpha_{yy}E}$ $\propto \alpha_{so}\alpha_{zz}sin\gamma$	$\propto \frac{p_x \cos\gamma}{p_y}$ $\propto \frac{\alpha_{so}\alpha_{xx}\alpha_{yy}E\cos\gamma}{\alpha_{yy}E_y}$ $\propto \alpha_{so}\alpha_{xx}cos\gamma$	$\propto 0$

Table B2: Analytical formulas for all the MOKE geometries when the incident light is s-polarized.

B3 Couple Dipole Approximation (CDA)

The Coupled Dipole Approximation (CDA) is used to obtain semi-analytical results for periodically arranged nanoantennas. This method relies on the formalism introduced by Draine and Flatau for the Discrete Dipole Approximation (DDA).[134, 156, 204] When an ensemble of ordered nanoantennas is illuminated by an electromagnetic wave, the total field affecting the dipolar response of each nanoantenna is the sum of the incident field and the scattered fields produced by all the other nanoantennas of the array. Within the CDA, each nanoantenna of the system is treated as a point-dipole characterized by the polarizability $\bar{\bar{\alpha}}$ defined in Eq. (B6). This leads to a system of coupled equations to be solved self-consistently, the solution of which provides the dipole momenta of all the nanoantennas. In the case of an infinite rectangular 2D array of indistinguishable

nanoantennas illuminated at normal incidence by a plane-wave (we set the array lying on the *xy*-plane and the wavevector of the incident light parallel the *z*-axis), the dipole moment of each nanoantenna reads as follows[134]

$$\tilde{\bar{p}} = \varepsilon_0 \left(\bar{\bar{I}} - \varepsilon_0 \tilde{\bar{\bar{\alpha}}} \tilde{\bar{\bar{S}}}\right)^{-1} \tilde{\bar{\bar{\alpha}}} \tilde{\bar{E}}_0 = \varepsilon_0 \tilde{\bar{\bar{\alpha}}}^{eff} \tilde{\bar{E}}_0 \quad \text{(B10)}$$

with $\tilde{\bar{E}}_0$ being the electric field vector of the incident radiation and $\tilde{\bar{\bar{\alpha}}}^{eff}$ the effective polarizability tensor of the particle. $\tilde{\bar{\bar{S}}}$ is the so-called geometrical factor tensor accounting for contributions from all the other dipoles of the array:

$$\tilde{\bar{\bar{S}}} = \sum_j \frac{1}{4\pi\varepsilon_0 \tilde{\bar{\varepsilon}}_M} \frac{e^{i\tilde{k}r_j}}{r_j^3} \left[\frac{1}{r_j^2}\left(3\bar{r}_j\bar{r}_j - \bar{\bar{I}}r_j^2\right) - \frac{i\tilde{k}}{r_j}\left(3\bar{r}_j\bar{r}_j - \bar{\bar{I}}r_j^2\right) + \tilde{k}^2\left(\bar{\bar{I}}r_j^2 - \bar{r}_j\bar{r}_j\right)\right] \quad \text{(B11)}$$

In this expression $\bar{r}_j = (x_j, y_j)$ is the vector linking the considered nanoantenna with the *j*th nanoantenna of the array and r_j its norm. We have implemented the above model and performed the CDA calculations presented in Chapter 4 for an array of 1000 x 1000 scatterers. By verifying the convergence of the series, we have ensured that such a finite system reproduces well the optical response of an infinite array. Once $\tilde{\bar{\bar{\alpha}}}$ or $\tilde{\bar{\bar{\alpha}}}^{eff}$ are known, the extinction cross section and the complex Kerr angle can be calculated. Experimentally we measure the Extinction Q_{ext} of the sample. For these reasons we converted σ_{ext} in Q_{ext} through the following formula[158]

$$Q_{ext} = \frac{\sigma_{ext}}{S} \quad \text{(B12)}$$

For the array $S = h_x h_y$, with $h_x(h_y)$ is the array pitch in the *x*-(*y*-)direction, while for a single nanoantenna $S = \pi a_x a_y$, with $a_x(a_x)$ the semi-axis of the antenna along the *x*-(*y*-) direction.

B4 Optical response of plasmonic dimers

B4.1 Analytical method

Let´s consider a triple layer stack as sketched in Figure B2. The first and the last layer are semi-infinite medium characterized by homogeneous and isotropic dielectric functions ε_1 and ε_3 respectively. The middle layer has a thickness d and an in-plane anisotropic delectric medium $\varepsilon_L = \varepsilon_2$. For s-polarized light, the transmission and reflection Fresnel coefficients can be written as

$$t_{ij} = \frac{2C_i}{C_i + C_j} \tag{B13}$$

$$r_{ij} = \frac{C_i - C_j}{C_i + C_j} \tag{B14}$$

where $C_i = \varepsilon_i \cos\theta_i$ and θ_i is the illumination angle.

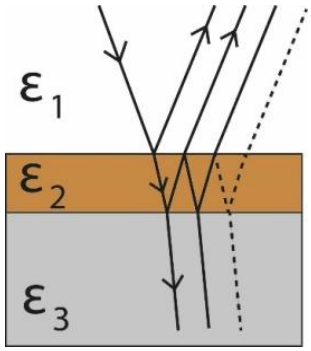

Figure B2: Sketch of the 3 layers model used for the derivation of Eq. (3.1).

Taking into account multiple reflections and writing $\beta = (2\pi d/\lambda)\sqrt{\varepsilon_2}\cos\theta_i$., the transmission coefficient for the three layers system reads as[205]

$$t_{123} = \frac{t_{12}t_{23}e^{i\beta}}{1 + r_{12}r_{23}e^{i2\beta}} \tag{B15}$$

Usually, the absolute transmission t_{123} is difficult to evaluate. However, the quantity t_{123}/t_{13} can be measured easily due to cancellation of common errors. We can also assume that system is illuminated at normal incidence with polarization 45° with respect to the eigen-direction x of the anisotropic layer. The changes in transmission due to the presence of the thin layer can then be written as

$$\frac{\Delta t^x}{t_{13}} = \frac{t_{123}^x - t_{13}}{t_{13}} \tag{B16}$$

Now, in the limit of small thickness $d \ll \frac{2\pi}{\lambda}\sqrt{\varepsilon_2}\cos\theta_i$, the exponential factor can be expanded into $e^{i\beta} \sim 1 + \frac{2\pi d}{\lambda}\sqrt{\varepsilon_2}\cos\theta_i$ and, for normal incidence illumination and using Eqs. (B13), (B14) and (B15), Eq. (B16) can then be approximated to

$$\frac{\Delta t^x}{t_{13}} \sim \frac{2\pi d\sqrt{\varepsilon_1}\, i}{\lambda}\frac{((\varepsilon_3)^2 - \varepsilon_{L,x})}{1 + \sqrt{\varepsilon_3}} \tag{B17}$$

If the substrate is then isotropic (as in this case), the analysis of the data is simplified as the rotation in tansmission is small enough to be treated in the first order in the optical functions, similar to what was previously shown for reflection.[206] The rotation can then be written as

$$\theta + i\xi = \frac{t_{123}^x - t_{123}^y}{t_{123}^x + t_{123}^y} = \frac{\Delta t^x - \Delta t^y}{2\, t_{13} + (\Delta t^x + \Delta t^y)} \approx \frac{\Delta t^x - \Delta t^y}{2\, t_{13}} \tag{B18}$$

where we have assumed that the transmission without the presence of the layer is much larger than the changes in transmission due to the presence of the anisotropic metasurface, i.e. $2\,t_{13} \gg (\Delta t^x + \Delta t^y)$. If measurements were performed in air ε_1=1, and combining Eq. (B17) and Eq. (B18), we obtain that

$$\theta + i\xi = \frac{\pi d\, i}{\lambda} \frac{(\varepsilon_{L,x} - \varepsilon_{L,y})}{1 + \sqrt{\varepsilon_3}} \tag{B19}$$

If we rewrite the dielectric function of the substrateas $n_s = \sqrt{\varepsilon_3}$, we retrieve thus Eq. (3.1).

B4.2 Couple dipoles method

The optical polarizability of the single dimer building block, which is assumed to be a point-like dipole and it is modeled as an oblate ellipsoid, is calculated using the quasistatic approximation presented in Appendix B1. The polarizability tensor of the single ellipsoid expression reads, in Gauss units, as follows

$$\bar{\bar{\alpha}} = \frac{V}{4\pi} \varepsilon_m (\varepsilon - \varepsilon_m) \bar{\bar{I}} \cdot \left[\varepsilon_m \bar{\bar{I}} + (\varepsilon - \varepsilon_m) \left(\bar{\bar{L}} - \frac{Vk^2}{4\pi} \bar{\bar{D}} - ik^3 \frac{V}{6\pi} \bar{\bar{I}} \right) \right]^{-1} \tag{B20}$$

Where $V = 4\pi r_1 r_2 r_3/3$ is the volume of the ellipsoid with radii r_i $(i = 1,2,3)$, $k = 2\pi n/\lambda$ the wavevector of the incoming light in the medium with index $n = \sqrt{\varepsilon_m} = \sqrt{({n_{sub}}^2 + {n_0}^2)/2}$ and ε is the dielectric function of gold.[75] Using the CDA method and assuming the polarization plane of the incident electric field lying on the *x*-axis (direction defined by r_1 and also corresponding to the long-axis of the dimer), one can write the effective polarizability tensor as follows[207]

$$\overline{\overline{\alpha_{eff}}} = \begin{pmatrix} \alpha_{||} & 0 & 0 \\ 0 & \alpha_{\perp} & 0 \\ 0 & 0 & \alpha_{\perp} \end{pmatrix} \tag{B21}$$

where

$$\alpha_{||} = \frac{2\alpha_1 + 2{\alpha_1}^2 k^3 [A(kR) + B(kR)]}{1 - {\alpha_1}^2 k^6 [A(kR) + B(kR)]^2} \tag{B22}$$

and

$$\alpha_{\perp} = \frac{2\alpha_1 + 2{\alpha_1}^2 k^3 A(kR)}{1 - {\alpha_1}^2 k^6 A(kR)^2} \tag{B23}$$

Here R is the distance between the centers of the two dimer building blocks, namely $2r_1 + g$, where g is the gap between the two disks. Experimentally g = 15 nm, which is also the value assumed in the calculations. The functions $A(kR)$ and $B(kR)$ read as follows

$$A(kR) = \left(\frac{1}{kR} + \frac{i}{(kR)^2} - \frac{1}{(kR)^3}\right) e^{ikR} \tag{B24}$$

$$B(kR) = \left(-\frac{1}{kR} - \frac{3i}{(kR)^2} + \frac{3}{(kR)^3}\right) e^{ikR} \tag{B25}$$

Once the effective polarizability of the dimer is known, one can apply the Maxwell-Garnett Approximation for calculating the effective dielectric tensor of the metasurface layer made by the dimmers in contact with the glass substrate and the air. To do so we normalized the quantity expressed by Eq. (B20) to the volume of the dimer, namely $2V$, and obtained the following expression for the effective dielectric tensor[7]

$$\bar{\bar{\varepsilon}}_{eff} = \left(f_1\bar{\bar{I}} + 2f_2\bar{\bar{\alpha}}_{eff}\right) \cdot \left(f_1\bar{\bar{I}} - f_2\bar{\bar{\alpha}}_{eff}\right)^{-1} \tag{B26}$$

This quantity allow us to calculate the Fresnel transmission and reflection coefficients of a multilayered system, which is assumed to model the real system studied in the experiments. Using the TMM, it is possible to calculate the angles of ellipticity and rotation. The dimensions of the single disk composing the dimer used to reproduce the experimental results are D = 95 nm, h = 45 nm, f_2 = 20%. The effective medium layer thickness was used as fitting parameter to reproduce the intensity of the measured quantities. In our case we assumed such a thickness to be 1.5h.

B5 Derivation of the Faraday and Kerr angles

According to Eq. (1.37), the electric field after propagating a distance *z* in the medium is

$$e^{i\psi}\begin{bmatrix}\cos(\delta)\\ \sin(\delta)\end{bmatrix} = e^{i\psi}\,\mathbf{A} \tag{B27}$$

where

$$\psi = \frac{\pi z}{\lambda_0}(n_R + n_L) \tag{B28a}$$

$$\delta = \frac{\pi z}{\lambda_0}(n_R - n_L) \tag{B28b}$$

The nature of the resulting (elliptical) polarization is defined by the vector $\mathbf{A}$. Rotation angle and the ellipticity angle are defined as ϑ and $\tan(\varepsilon) = \boldsymbol{b}/\boldsymbol{a}$ ($\boldsymbol{a}$ is the major semi-axis, $\boldsymbol{b}$ is the minor semi-axis, as sketched in Figure B3).

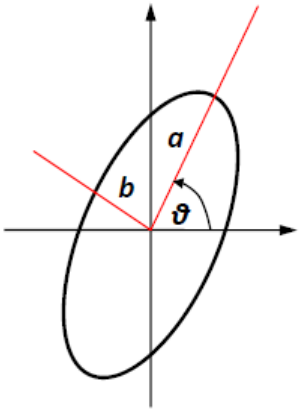

Figure B3: Sketch of elliptical polarized light, rotated with respect to the direction of oscillation of the incident electric field.

Since the ellipticity $\tan(\varepsilon) = b/a$ it absolute value is ≤ 1, so the absolute value of the ellipticity angle is ≤ 45°.[208] Then, ϑ expresses the "orientation" of the ellipse and the sign of ε expresses the "handedness" (R or L). Writing δ as

$$\delta = x + iy \tag{B29}$$

We get

$$\begin{bmatrix} cos(\delta) \\ sin(\delta) \end{bmatrix} = \begin{bmatrix} cosx & -sinx \\ sinx & cosx \end{bmatrix} \begin{bmatrix} coshy \\ isinhy \end{bmatrix} = \bar{\bar{R}} \cdot \boldsymbol{E} \tag{B30}$$

Now, $\boldsymbol{E}$ represents an ellipse "aligned" with the reference axes, whose semi-axes are $coshy$ and $sinhy$. So we have

$$\tan(\varepsilon) = \frac{sinhy}{coshy} = \tanh[Im(\delta)] \tag{B31}$$

which is Eq. (1.40). $\bar{\bar{R}}$ is a rotation matrix, so x represents the angle at which the ellipse is rotated:

$$\vartheta = Re(\delta) \tag{B32}$$

which is Eq. (1.39). In principle, all these formulas are valid for any angle, not only in the small angle approximation. Regarding Eq. (1.43), the proportional symbol expresses the fact that a global factor that doesn't modify the type of polarization (in terms of rotation and ellipticity) was omitted. We can define two parameters, C and D according to the following criterion:

$$\begin{bmatrix} 1 \\ i\left(\dfrac{n_R - n_L}{1 - n_R n_L}\right) \end{bmatrix} = \begin{bmatrix} 1 \\ \mathrm{C} + iD \end{bmatrix} \tag{B33}$$

Under the assumption of small effects, the involved angles are also small and C can be identified with rotation, whereas D can be identified with ellipticity. Indeed, for small angles it turns out that

$$\lim_{\delta \to 0} \begin{bmatrix} cos(\delta) \\ sin(\delta) \end{bmatrix} = \begin{bmatrix} 1 \\ \delta \end{bmatrix} = \begin{bmatrix} 1 \\ Re(\delta) + iIm(\delta) \end{bmatrix} \tag{B34}$$

And so $\lim_{\varepsilon \to 0} \tan(\varepsilon) = \lim_{\delta \to 0} \tanh[Im(\delta)]$ implies that $\varepsilon = Im(\delta)$, and so we recover Eq. (1.37).

Bibliography

[1] https://www.pa.msu.edu/~yang/RFeynman_plentySpace.pdf

[2] Taniguchi, N. *On the Basic Concept of 'Nano-Technology*. Proc. Intl. Conf. Prod. Eng. Tokyo, Part II, Japan Society of Precision Engineering, 1974.

[3] http://www1.appstate.edu/dept/physics/nanotech/EnginesofCreation2_8803267.pdf

[4] Yu, N.; Capasso, F. *Nat. Mater.* **2014**, 13, 139−150.

[5] Cai, W.; Shalaev, V. M. *Optical Metamaterials: Fundamentals and Applications*. Springer, 2010.

[6] Sandtke, M.; Kuipers, L. *Nat. Photon.* **2007**, 1, 573–576.

[7] Ferry, V. E.; Sweatlock, L. A.; Pacifici, D.; Atwater, H. A. *Nano Lett.* **2008**, 8, 4391–4397.

[8] Sepulveda, B.; Calle, A.; Lechuga, L.; Armelles, G. *Opt. Lett.* **2006**, 31, 1085.

[9] Belotelov, V. I.; Doskolovich, L. L.; Zvezdin, A. K. *Phys. Rev. Lett.* **2007**, 98, 077401.

[10] Belotelov, V. I.; et al. *Nature Nanotechnol.* **2011**, 6, 370−376.

[11] González-Díaz, J. B. et al. *Adv. Mater.* **2007**, 19, 2643.

[12] Jain, P. K.; Xiao, Y.; Walsworth, R.; Cohen, A. E.; *Nano Lett.* **2009**, 9, 1644.

[13] González-Díaz, J. B.; et al. *Small* **2008**, 4, 202−205.

[14] González-Díaz, J. B.; Sepúlveda, B.; García-Martín, A.; Armelles, G. *Appl. Phys. Lett.* **2010**, 97, 043114.

[15] Insin, N. et al., *ACS Nano* **2008**, 2, 197.

[16] Weng, K. C. et al., *Nano Lett.* **2008** 8, 2851.

[17] Temnov, V. V.; Armelles, G.; Woggon, U.; Guzatov, D.; Cebollada, A.; García-Martín, A.; García-Martín, J.-M., Thomay, T.; Leitenstorfer, A.; Bratschitsch, R. *Nat. Photon.* **2010**, 4, 107-111.

[18] Tomita, S. et al., *Phys. Rev. Lett.* **2006**, 96, 167402.

[19] Wang, L.; Clavero, C.; Huba, Z.; Carroll, K. J.; Carpenter, E. E.; Gu, D.; Lukaszew, R. A. *Nano Lett.* **2011**, 11, 1237-1240.

[20] Liu, Z. et al. *Appl. Phys. Lett.* **2009**, 95, 032502.

[21] Du, G. X.; Mori, T.; Saito, S.; Takahashi, M. *Phys. Rev. B* **2010**, 82, 161403.

[22] Melle, S. et al. *Appl. Phys. Lett.* **2003**, 83, 4547.

[23] Ctistis, G.; Papaioannou, E.; Patoka, P.; Gutek, J.; Fumagalli, P.; Giersing, M. *Nano Lett.* **2009**, 9, 1−6.

[24] González-Diaz, J. B. et al. *Appl. Phys. Lett.* **2009**, 94, 263101.

[25] Armelles, G.; Cebollada, A.; García-Martín, A.; González, M. U. *Adv. Opt. Mater.* **2013**, 1, 10−35.

[26] Armelles, G.; et al. *J. Opt. A: Pure Appl. Opt.* **2009**, 11, 114023.

[27] Chin, J. Y.; et al. *Nat. Commun.* **2013**, 4, 1599.

[28] Temnov, V. V. *Nat. Photonics* **2012**, 6, 728−736.

[29] Belotelov, V. I.; et al. *Nat. Commun.* **2013**, 4, 2118.

[30] Temnov, V. V.; et al. *Nat. Commun.* **2013**, 4, 1468.

[31] Banthí, J. C.; Meneses-Rodríguez, D.; García, F.; González, M. U.; García-Martín, A.; Cebollada, A.; Armelles, G. *Adv. Mater.* **2012**, 24, OP36−OP41.

[32] Papaioannou, E. T.; et al. *Opt. Express* **2011**, 19, 23867−23877.

[33] Razdolsky, I.; et al. *Phys. Rev. B* **2013**, 88, 075436.

[34] Valev, V. K.; et al. *ACS Nano* **2010**, 5, 91−96.

[35] J. Chen et al., *Small* **2011**, 7, 2341.

[36] Bonanni, V. et al. *Nano Lett.* **2011**, 11, 5333-5338.

[37] Novotny, L.; Hecht, B. *Principles of Nano-Optics.* Cambridge University Press, 2006.

[38] Maier, S. A. *Plasmonics: Fundamental and Applications.* Springer, New York, 2007.

[39] Barnes, W. L., Dereux, A., Ebbesen, T. W. *Nature* **2003**, 424, 824-830.

[40] Shalaby, M.; Peccianti, M.; Ozturk, Y.; Morandotti, R. *Nat. Commun.* **2013**, 4, 1558.

[41] Tamagnone, M.; Fallahi, A.; Mosig, J. R.; Perruisseau-Carrier, J. *Nat. Photonics* **2014**, 8, 556−563.

[42] Yu, Z.; Fan, S. *Nat. Photonics* **2009**, 3, 91−94.

[43] Bi, L.; et al. *Nat. Photonics* **2011**, 5, 758−762.

[44] Stadler, B. J. H.; Mizumoto, T. *IEEE Photonics J.* **2014**, 6, 600215.

[45] Kildishev, A. V.; Boltasseva, A.; Shalaev, V. M. *Science* **2013**, 340, 1232009.

[46] Yu, N.; et al. *Nano Lett.* **2012**, 12, 6328−6333.

[47] Monticone, F.; Estakhri, N. M.; Alù, A. *Phys. Rev. Lett.* **2013**, 110, 203903.

[48] Holloway, C. L.; et al. *IEEE Antennas Propag. Mag.* **2012**, 54, 10−35.

[49] Aieta, F.; et al. *Nano Lett.* **2012**, 12, 1702−1706.

[50] Pendry, J. B.; Schurig, D.; Smith, D. R. *Science* **2006**, 312, 1780−1782.

[51] Li, Y.; Zhang, Q.; Nurmikko, A.V.; Sun, S. *Nano Lett.* **2005**, 5, 1689.

[52] Papaioannou, E. Th.; et al. *Phys. Rev. B* **2010**, 81, 054424.

[53] Grunin, A. A.; Zhdanov, A. G.; Ezhov, A. A.; Ganshina, E. A.; Fedyanin, A. A. *Appl. Phys. Lett.* **2010**, 97, 261908.

[54] Wang, F.; Chakrabarty, A.; Minkowski, F.; Sun, K.; Wei, Q.-H. *Appl. Phys. Lett.* **2012**, 101, 023101.

[55] Rubio-Roy, M.; Vlasin, O.; Pascu, O.; Caicedo, V.; Schmidt, M.; Goñi, A. R.; Tognalli, N. G.; Fainstein, A.; Roig, A.; Herranz, G. *Langmuir* **2012**, 28, 9010.

[56] Pineider, F. et al. *Nano Lett.* **2013**, 13, 4785−4789.

[57] Sepúlveda, B.; González-Díaz, J. B.; García-Martín, A.; Lechuga, L. M.; Armelles, G. *Phys. Rev. Lett.* **2010**, 104, 147401.

[58] Tuboltsev, V.; Savin, A.; Pirojenko, A.; Räisänen, J. *ACS Nano* **2013**, 7, 6691−6699.

[59] Fox, M. *Optical Properties of Solids*. Oxford University Press, 2003.

[60] Ashcroft, N. W.; Mermin, N. D. *Solid State Physics*. Brooks Cole, 1976.

[61] Johnson, P. B.; Christy, R. W. *Phys. Rev. B* **1972**, 6, 4370-4379.

[62] Pinchuk, A.; Kreibig, U.; Hilger, A. *Surface Science* **2004**, 557, 269-280.

[63] Kang, H.; Milton, G. W. *Arch. Rational Mech. Anal.* **2008**, 188, 93-116.

[64] Borhen, C. F.; Huffman, D. R. Absorption and Scattering of *Light by Small Particles*. Wiley, 1998.

[65] Giannini, V.; Fernandenz-Dominguez, A. I.; Heck, S. C.; Maier, S. A. *Chem. Rev.* **2011**, 111, 3888-3912.

[66] Langhammer, C.; Yuan, Z.; Kasemo, B. *Nano Lett.* **2006**, 6, 833−838.

[67] Meier, M.; Wonaun, A. *Opt. Lett.* **1983**, 8, 581-583.

[68] Wonaun, A.; Gordon, J. P. *Phys. Rev. Lett.* **1982**, 48, 957-960.

[69] Jackson, J. D. *Classical Electrodynamic*. John Wiley & Sons, 1975.

[70] Zayats, A. V.; Richards, D. *Nano-Optics and Near-Field Optical Microscopy*. Artech House, Boston, USA, 2009.

[71] Liedberg, B.; Nylander, C.; Lunström, I. *Sensors and Actuators* **1983**, 4, 299-304.

[72] Homola, J.; Yee, S. S.; Gauglitz, G. *Sens. Actuators B* **1999**, 54, 3-15.

[73] Ozbay, E. *Science* **2006**, 311, 189-193.

[74] Jones, A. C. et al. *Nano Lett.* **2009**, 9, 2553-2558.

[75] Johnson, P. B.; Christy, R. W. *Phys. Rev. B* **1974**, 9, 5056-5070.

[76] Wang, F.; Shen, Y. R. *Phys. Rev. Lett.* **2006** ,97, 206806.

[77] Wood, R. *Proc. R. Soc. London, Ser. A* **1902**, 18, 269-275.

[78] Wood, R. *Phys. Rev.* **1935**, 48, 928-936.

[79] Rayleigh, L. *Proc. R. Soc. London, Ser. A* **1909**, 79, 399-416.

[80] Strong, J. *Phys. Rev.* **1936**, 49, 291–296.

[81] Fano, U. *J. Opt. Soc. Am.* 1941, 31, 213–222.

[82] Luk'yanchuk, B.; Zheludev, N. I.; Maier, S. A.; Halas, N. J.; Nordlander, P.; Giessen, H.; Chong, C. T. *Nat. Mater.* **2010**, 9, 707−715.

[83] http://teacher.nsrl.rochester.edu/PHY235/LectureNotes/Chapter12/Chapter12.pdf

[84] Joe, Y. S.; Satanin, A. M.; Kim, C. S. *Phys. Scr.* **2006**, 74, 259-266.

[85] Miroshnichenko, A. E.; Flach, S.; Kivshar, Y. S. *Rev. Mod. Phys.* **2010**, 82, 2257-2298.

[86] Breit, G.; Wigner, E. *Phys. Rev.* **1936**, 49, 519-531.

[87] Freiser, M. J. *IEEE Trans. Magn.* **1968**, 4, 152-161.

[88] Antonov, V.; Harmon B.; Yaresko, A. *Electronic Structure and Magneto-Optical Properties of Solids.* Kluwer Academic Publishers, 2004.

[89] Landau, L. D.; Lifshitz, E. M. *Electrodynamics of Continuous Media*. Pergamon Press, 1984.

[90] Fowles, G. R. *Introduction to Modern Optics*. Dover Publications, Inc., 1989.

[91] Osgood III, R. M. *Hysteresis Loops in Anisotropic Thin Films*. PhD Thesis, Stanford University, 1996.

[92] Argyres, P. N. *Phys. Rev.* **1955**, 97, 334-345.

[93] Atkinson, R.; Lissberger, P. H. *Appl. Opt.* **1992** 31, 6076-6081.

[94] Garnett, J. C. M. *Phil. Trans. R. Soc. B.* **1904**, 203, 385-420.

[95] Landauer, R. *J. Appl. Phys.* **1952**, 23, 779-784.

[96] Stroud, D. *Phys. Rev. B* **1975**, 12, 3368-3373.

[97] Višňovský, Š.; Pařízek, V.; Nývlt, M.; Kielar, P.; Prosser, V; Krishnan, R. J. Magn. Magn. Mater. **1993**, 127, 135-139.

[98] Krinchik, G. S.; Artem'ev, V. A. *Sov. Phys. JETP.* **1968**, 26, 1080-1085.

[99] Schubert, M.; Tiwald, T. E.; Woollam, J. A. *Appl. Opt.* **1999**, 38, 177-187.

[100] Zak, J.; Mook, E. R.; Liu, C.; Bader, S. D. *J. Magn. Magn. Mater.* **1990**, 89, 107-123.

[101] Višňovský, Š.; Lopusnik, R.; Bauer, M.; Bok, J.; Fassbender, J.; Hillebrands, B. *Opt. Express* **2001**, 9, 121-135.

[102] Maccaferri, N.; Kataja, M.; Bonanni, V.; Bonetti, S.; Pirzadeh, Z.; Dmitriev, A.; van Dijken, S.; Åkerman, J.; Vavassori, P. Phys. Status Solidi A, 2014, 211, 1067-1075.

[103] Kravets, V. G. et al. *Nat. Mater.* **2013**, 12, 304–309.

[104] Anker, J. N.; Hall, W. P.; Lyandres, O.; Shah, N. C.; Zhao, J.; Van Duyne, R. P. *Nat. Mater.* **2008**, 7, 442-453.

[105] Stewart, M. E.; Anderton, C. R.; Thompson, L. B.; Maria, J.; Gray, S. K.; Rogers, J. A.; Nuzzo, R. G. *Chem. Rev.* **2008**, 108, 494-521.

[106] Cui, Y.; Wei, Q. Q.; Park, H. K.; Lieber, C. M. *Science* **2001**, 293, 1289–1292.

[107] Anker, J. N. et al. *Nat. Mater.* **2008**, 7, 442–453.

[108] Larsson, E. M.; Syrenova, S.; Langhammer, C. *Nanophotonics* **2012**, 1, 249–266.

[109] Mayer, K. M.; Hafner, J. H. *Chem. Rev.* **2011** 111, 3828–3857.

[110]Chung, T.; Lee, S. Y.; Song, E. Y.; Chun, H.; Lee, B. *Sensors* **2011**, 11, 10907–10929.

[111]Shen, Y. et al. *Nat. Commun.* **2013**, 4, 2381.

[112]Aćimović, S. S. et al. *Nano Lett.* **2014**, 14, 2636–2641.

[113]Kabashin, A. V. et al. *Nat. Mater.* **2009**, 8, 867–871.

[114]Zijlstra, P.; Paulo, P. M. R.; Orrit, M. *Nat. Nanotech.* **2012**, 7, 379-382.

[115]Aćimović, S. S.; Kreuzer, M. P.; González, M. U.; Quidant, R. *ACS Nano* **2009**, 3, 1231-1237.

[116] Li, J.; Ye, J.; Chen, C.; Hermans, L.; Verellen, N.; Ryken, J.; Jans, H.; Van Roy, W.; Moshchalkov, V. V.; Lagae, L.; Van Dorpe, P. *Adv. Opt. Mater* **2015**, 3, 176-181.

[117]Svedendahl, M.; Chen, S.; Dmitriev, A.; Käll, M. *Nano Lett.* **2009**, 9, 4428–4433.

[118]Otte, M. A. et al. *ACS Nano* **2010**, 4, 349–357.

[119]Offermans, P. et al *ACS Nano* **2011**, 5, 5151–5157.

[120]Lodewijks, K. et al. *Plasmonics* **2013**, 8, 1379–1385.

[121]Verellen, N. et al. *Nano Lett.* **2011**, 11, 391–397.

[122]Lodewijks, K.; Van Roy, W.; Borghs, G.; Lagae, L.; Van Dorpe, P *Nano Lett.* **2012**, 12, 1655–1659.

[123]Svedendahl, M.; Verre, R.; Kall, M. *Light Sci. Appl.* **2014**, 3, e220.

[124]Toudert, J.; Wang, X.; Tallet, C.; Barois, P.; Aradian, A.; Ponsinet, V. *ACS Photonics* **2015**, 2, 1443-1450.

[125]Wersäll, M.; Verre, R.; Svedendahl, M.; Johansson, P.; Käll, M.; Shegai, T. *J. Phys. Chem. C* **2014**, 118, 21075-21080.

[126]Piliarik, M.; Šípová, H.; Kvasnička, P.; Galler, N.; Krenn, J. R.; Homola, J. *Opt. Express* **2012**, 20, 672-680.

[127]Moirangthem, R. S.; Chang, Y.-C.; Hsu, S.-H.; Wei, P.-K. *Biosensors and Bioelectronics* **2010**, 25, 2633-2638.

[128]Arwin, H.; Poksinski, M.; Johansen, K. *Appl. Opt.* **2004**, 43, 3028-3036.

[129]Kravets, V. G.; Schedin, F.; Kabashin, A. V.; Grigorenko, A. N. *Opt. Lett.* **2010**, 35, 956-958.

[130]Liu, S.-D.; Qi, X.; Zhai, W.-C.; Chen, Z.-H.; Wang, W.-J.; Han, J.-B. *Nanoscale* **2015**, 7, 20171-20179.

[131]Jeong, H.-H.; Mark, A. G.; Alarcón-Correa, M.; Kim, I.; Oswald, P.; Lee, T.-C.; Fischer, P. *Nat. Commun.* **2016**, 7, 11331.

[132]Verre, R.; Fleischer, K.; Sofin, R. G. S.; McAlinden, N.; McGilp, J. F.; Shvets, I. V. *Phys. Rev. B* **2011**, 83, 125432.

[133]Schubert, M. *Phys. Rev. B* **1996**, 53, 4265-4274.

[134]Zou, S.; Janel N.; Schatz, C. G. *J. Chem. Phys.* **2004**, 120, 10871-10875.

[135]Boris, K.; Andrei, M.; Vladimir, Z.; Nikolai, K. *Nanotechnology* **2006**, 17, 1437-1445.

[136]Dmitriev, A. et al. *Nano Lett.* **2008**, 8, 3893–3898..

[137]Knez, M.; Nielsch, K.; Niinistö, L. *Adv. Mater.* **2007**, 19, 3425–3438.

[138]George, S. M. *Chem. Rev.* **2010**, 110, 111–131.

[139]Du, Y.; George, S. M. *J. Phys. Chem. C* **2007**, 111, 8509–8517.

[140]Dahlin, A. B.; Tegenfeldt, J. O.; Höök, F. *Anal. Chem.* **2006**, 78, 4416–4423.

[141]Chen, S.; Svedendahl, M.; Käll, M.; Gunnarsson, L.; Dmitriev, A. *Nanotechnology* **2009**, 20, 434015.

[142]Hochuli, E.; Bannwarth, W.; Döbeli, H.; Gentz, R.; Stüber, D. *Nat. Biotechnol.* **1988**, 6, 1321–1325.

[143]Adamczyk, Z.; Siwek, B.; Zembala, M.; Belouschek, P. *Advances in Colloid and Interface Science* **1994**, 48, 151-280.

[144]Rosano, C.; Arosio, P.; Bolognesi, M. *Biomolecular Engineering* **1999**, 16, 5-12.

[145]Huang, N.-P.; Vörös, J.; De Paul, S. M.; Textor, M.; Spencer, N. D. *Langmuir* **2002**, 18, 220-230.

[146]Caballero, B.; García-Martín, A.; Cuevas, J. C. *ACS Photonics* **2016**, 3, 203–208.

[147]Naik, G. V.; Shalaev, V. M.; Boltasseva, A. *Adv. Mater.* **2013**, 25, 264−3294.

[148]Knight, M. W.; King, N. S.; Liu, L.; Everitt, H. O.; Nordlander, P.; Halas, N. J. *ACS Nano* **2014**, 8, 834−840.

[149]McClain, M. J.; Schlather, A. E.; Ringe, E.; King, N. S.; Liu, L.; Manjavacas, A.; Knight, M. W.; Kumar, I.; Whitmire, K. H.; Everitt, H. O.; Nordlander, P.; Halas, N. J. *Nano Lett.* **2015**, 15, 2751−2755.

[150]Safarov, V. I.; Kosobukin, V. A.; Hermann, C.; Lampel, G.; Peretti, J.; Marlière, C. *Phys. Rev. Lett.* **1994**, 73, 3584−3587.

[151]Ferré, J.; Pénissard, G.; Marlière, C.; Renard, D.; Beauvillain, P.; Renard, J. P. *Appl. Phys. Lett.* **1990**, 56, 1588−1590.

[152]Yang, K.; Clavero, C.; Skuza, J. R.; Varela, M.; Lukaszew, R. A. *J. Appl. Phys.* **2010**, 107, 103924.

[153]Armelles, G.; González-Díaz, J. B.; García-Martín, A.; García-Martín, J. M.; Cebollada, A.; González, M. U.; Acimovic, S.; Cesario, J.; Quidant, R.; Badenes, G. *Opt. Express* **2008**, 16, 16104.

[154]Armelles, G.; Cebollada, A.; García-Martín, A.; González, M. U.; García, F.; Meneses-Rodríguez, D.; de Sousa, N.; Froufe-Pérez, L. S. *Opt. Express* **2013**, 21, 27356−27370.

[155] Carron, K. T.; Fluhr, W.; Meier, M.; Wokaun, A.; Lehmann, H. W. *J. Opt. Soc. Am. B* **1986**, 3, 430.

[156] Markel, V. A. *J. Mod. Opt.* **1993**, 40, 2281−2291.

[157] Garcia de Abajo, F. J.; Gomez-Medina, R.; Saenz, J. J. *Phys. Rev. E* **2005**, 72, 016608.

[158] Auguié, B.; Barnes, W. L. *Phys. Rev. Lett.* **2008**, 101, 143902.

[159] Chu, Y.; Schonbrun, E.; Yang, T.; Crozier, K. B. *Appl. Phys. Lett.* **2008**, 93, 181108.

[160] Vecchi, G.; Giannini, V.; Gomez-Rivas, J. *Phys. Rev. Lett.* **2009**, 102, 146807.

[161] Halas, N. J.; Lal, S.; Chang, W. S.; Link, S.; Nordlander, P. *Chem. Rev.* **2011**, 111, 3913−3961.

[162] Humphrey, A. D.; Barnes, W. L. *Phys. Rev. B.* **2014**, 90, 075404.

[163] Garcia de Abajo, F. J. *Rev. Mod. Phys.* **2007**, 79, 1267.

[164] Kataja, M.; Hakala, T. K.; Julku, A.; Huttunen, M. J.; van Dijken, S.; Törmä, P. *Nat. Commun.* **2015**, 6, 7072.

[165] Auguié, B.; Barnes, W. L. *Opt. Lett.* **2009**, 34, 401−403.

[166] Ritchie, R. H.; Arakawa, E. T.; Cowan, J. J.; Hamm, R. N. *Phys. Rev. Lett.* **1968**, 21, 1530−1533.

[167] Watts, R. A.; Preist, T. W.; Sambles, J. R. Sharp Surface-Plasmon

Resonances on Deep Diffraction Gratings. Phys. Rev. Lett. 1997, 79,

3978−3981.

[168] Kats, A. V.; Nesterov, M. L.; Nikitin, A. Yu. *Phys. Rev. B* **2007**, 76, 045413.

[169] Romanato, F.; Lee, K. H.; Ruffato, G.; Wong, C. C. *Appl. Phys. Lett.* **2010**, 96, 111103.

[170] Sapozhnikov, M. V.; Gusev, S. A.; Troitskii, B. B.; Khokhlova, L. V. *Opt. Lett.* **2011**, 36, 4197−4199.

[171] Kang, H. K.; Lee, K. H.; Wu, Y.; Wong, C. C. *Plasmonics* **2011**, 6, 373−380.

[172] Billaudeau, C.; Collin, S.; Sauvan, C.; Bardou, N.; Pardo, F.; Pelouard, J.-L. *Opt. Lett.* **2008**, 33, 165−167.

[173] Ebbesen, T. W.; Lezec, H. J.; Ghaemi, H. F.; Thio, T.; Wolff, P. A. *Nature* **1998**, 391, 667−669.

[174] García-Vidal, F. J.; Martín-Moreno, L.; Ebbesen, T. W.; Kuipers, L. *Rev. Mod. Phys.* **2010**, 82, 729−787.

[175] Altug, H.; Englund, D.; Vuckovic, J. *Nat. Phys.* **2006**, 2, 484−488.

[176] Bozhevolnyi, S. I.; Volkov, V. S.; Devaux, E.; Laluet, J.-Y.; Ebbesen, T. W. *Nature* **2006**, 440, 508−511.

[177] Lal, S.; Link, S.; Halas, N. J. *Nat. Photon.* **2007**, 1, 641−648.

[178] Fang, H.; Caballero, B.; Akinoglu, E. M.; Papaioannou, E. Th.; García-Martín, A.; Cuevas, J. C.; Giersig, M.; Fumagalli, P. *Appl. Phys. Lett.* **2015**, 106, 153104.

[179] Armelles, G.; Caballero, B.; Cebollada, A.; Garcia-Martin, A.; Meneses-Rodríguez, D. *Nano Lett.* **2015**, 15, 2045−2049.

[180] Chetvertukhin, A. V.; Grunin, A. A.; Baryshev, A. V.; Dolgova, T. V.; Uchida, H.; Inoue, M.; Fedyanin, A. A. *J. Magn. Magn. Mater.* **2012**, 324, 3516−3518.

[181] Kostylev, N.; Maksymov, I. S.; Adeyeye, A. O.; Samarin, S.; Kostylev, M.; Williams, J. F. *Appl. Phys. Lett.* **2013**, 102, 121907.

[182] Newman, D. M.; Wears, M. L.; Matelon, R. J.; Hooper, I. R. *J. Phys.: Condens. Matter* **2008**, 20, 345230.

[183] Torrado, J. F.; Papaioannou, E.Th.; Ctistis, G.; Patoka, P.; Giersig, M.; Armelles, G.; García-Martín, A. *Phys. Status Solidi RRL* **2010**, 4, 271−273.

[184] Melander, E.; Östman, E.; Keller, J.; Schmidt, J.; Papaioannou, E. Th.; Kapalis, V.; Arnalds, U. B.; Caballero, B.; García-Martín, A.; Cuevas, J. C.; Hjörvarsson, B. *Appl. Phys. Lett.* **2012**, 101, 063107.

[185] Xia, W. B.; et al. *Opt. Express* **2014**, 22, 1359−1365.

[186] Adeyeye, A. O.; Singh, N. *J. Phys. D: Appl. Phys.* **2008**, 41, 153001.

[187] Caballero, B.; García-Martín, A.; Cuevas, J. C. *Phys. Rev. B* **2012**, 85, 245103.

[188] Neuber, G.; et al. *Appl. Phys. Lett.* **2003**, 83, 4509−4511.

[189] Koerkamp, K. J. K.; Enoch, S.; Segerink, F. B.; van Hulst, N. F.; Kuipers, L. *Phys. Rev. Lett.* **2004**, 92, 183901.

[190] Maksymov, I. S. *Nanomaterials* **2015**, 5, 577.

[191] Vavassori, P. *Appl. Phys. Lett.* **2000**, 77, 1605-1607.

[192] Fredriksson, H.; Alaverdyan, Y.; Dmitriev, A.; Langhammer, C.; Sutherland, D. S.; Zäch, M.; Kasemo, B. *Adv. Mat.* **2007**, 19, 4297-4302.

[193] Meier, M.; Wokaun, A., Liao, P. F. *J. Opt. Soc. Am. B* **1985**, 2, 931-949.

[194] Hui, P. M.; Stroud, D. *Appl. Phys. Lett.* **1987**, 50, 950-952.

[195] Xia, T. K.; Hui, P. M.; Stroud, D. *J. Appl. Phys.* **1990**, 67, 2736-2741.

[196] Yang, Z. J.; Scheinfein, M. R. *J. Appl. Phys.* **1993**, 74, 6810-6823.

[197] Bragg, W. L.; Pippard, A. B. *Acta Cryst.* **1953**, 6, 865-867.

[198] Moroz, A. *J. Opt. Soc. Am. B* **2009**, 26, 517-527.

[199] Kuwata, H.; Tamaru, H.; Esumi, K.; Miyano, K. *Appl. Phys. Lett.* **2003**,. 83, 4625-4627.

[200] Kelly, K. L.; Coronado, E.; Zhao, L. L.; Schatz, G. C. *J. Phys. Chem. B* **2003**, 107, 668-677.

[201] Farafonov, V. G.; Il'in, V. B.; Prokop'eva, M. S. *Optics and Spectroscopy* **2002**, 92, 567-576.

[202] Abe, M. *Phys. Rev. B* **1996**, 53, 7065-7075.

[203] Abe, M.; Suwa, T. *Phys. Rev. B* **2004**, 70(23), 235103.

[204] Draine, B.T.; Flatau, P.J. *J. Opt. Soc. Am. A* **1994**, 11, 1491-1499.

[205] Born, M.; Wolf, E., *Principles of Optics (4th.ed.)*, Pergamon Press 1970.

[206] Aspnes, D. E.; Studna, A. A. *Phys. Rev. Lett.* **1985,** 54, 1956-1959.

[207] Boris, K.; Andrei, M.; Vladimir, Z.; Nikolai, K. *Nanotechnology* **2006,** 17, 1437.

[208] Tompkins, H. G.; Irene, E. A. *Handbook of Ellipsometry*, Springer, 2005.